UNIVERSIDAD NACIONAL AUTÓNOMA DE MÉXICO

MAESTRÍA EN CIENCIAS (FÍSICA)
INSTITUTO DE CIENCIAS NUCLEARES
FÍSICA DE ALTAS ENERGÍAS, FÍSICA NUCLEAR, GRAVITACIÓN Y FÍSICA MATEMÁTICA

COLLISION ENERGY DEPENDENCE OF THE SOURCE PARAMETERS FOR PRIMARY AND SECONDARY PIONS AT NICA ENERGIES

TESIS
QUE PARA OPTAR POR EL GRADO DE:
MAESTRO EN CIENCIAS FÍSICAS (FÍSICA)

PRESENTA:
SANTIAGO BERNAL LANGARICA

Tutor Principal:
DR. JOSÉ ALEJANDRO AYALA MERCADO
Instituto de Ciencias Nucleares, UNAM

Miembros del Comité Tutor:
DRA. MARÍA ELENA TEJEDA YEOMANS
Facultad de Ciencias–CUICBAS, Universidad de Colima

DRA. IVONNE ALICIA MALDONADO CERVANTES
Joint Institute for Nuclear Research, Rusia

Ciudad Universitaria, Ciudad de México, abril, 2024

PROTESTA UNIVERSITARIA DE INTEGRIDAD Y HONESTIDAD ACADÉMICA Y PROFESIONAL
(Graduación con trabajo escrito)

De conformidad con lo dispuesto en los artículos 87, fracción V, del Estatuto General, 68, primer párrafo, del Reglamento General de Estudios Universitarios y 26, fracción I, y 35 del Reglamento General de Exámenes, me comprometo en todo tiempo a honrar a la Institución y a cumplir con los principios establecidos en el Código de Ética de la Universidad Nacional Autónoma de México, especialmente con los de integridad y honestidad académica.

De acuerdo con lo anterior, manifiesto que el trabajo escrito titulado:

Collision energy dependence of the source parameters for primary and secondary pions at NICA energies

que presenté para obtener el grado de -----Maestria----- es original, de mi autoría y lo realicé con el rigor metodológico exigido por mi programa de posgrado, citando las fuentes de ideas, textos, imágenes, gráficos u otro tipo de obras empleadas para su desarrollo.

En consecuencia, acepto que la falta de cumplimiento de las disposiciones reglamentarias y normativas de la Universidad, en particular las ya referidas en el Código de Ética, llevará a la nulidad de los actos de carácter académico administrativo del proceso de graduación.

Atentamente

Santiago Bernal Langarica
No. de Cuenta 312142971

(Nombre, firma y Número de cuenta de la persona alumna)

Resumen

En el estudio de las colisiones de iones pesados relativistas, la caracterización de la estructura espacio temporal y el tamaño de la región de interacción entre los núcleos que colisionan ha sido una herramienta básica para el estudio de las propiedades de los sistemas fuertemente interactuantes que se producen en este tipo de colisiones. El uso de las correlaciones cuánticas para determinar las características de dichas regiones es conocido como femtoscopía.

En este trabajo se estudiaron los parámetros que describen la función de correlación de dos piones, en el contexto de colisiones de iones pesados relativistas, y su evolución como función de la energía de la colisión en el intervalo energético de NICA. Para esto, se simularon cinco millones de colisiones de Bi+Bi, por energía estudiada, usando el generador Monte Carlo denominado *Ultra-relativistic Quantum Molecular Dynamics*. Esta cantidad de colisiones fue seleccionada para tener suficiente estadísitca para el análisis que se hizo. Los efectos de las correlaciones cuánticas se incluyeron con el formalismo *correlation afterburner* CRAB. Los resultados de la función de correlación se ajustaron utilizando distribuciones Gaussianas, Lorentzianas y de Lévy, donde esta última dio como resultado los mejores ajustes. La muestra completa se separó en piones que tienen un origen primario y piones que provienen del decaimiento de resonancias cuya vida media es grande. Se mostró que el tamaño de la fuente de estas últimas es mucho mayor que el de las primeras, resultado que es consistente con el modelo de *núcleo-halo* de la producción de piones. Los efectos de un detector no ideal se simularon al incluir un parámetro de *smearing* (embarramiento) en el momento para representar el momento mínimo del par de piones y entonces, por la relación de incertidumbre de Heisenberg, un tamaño máximo de la fuente que se puede resolver.

Recurriendo una vez más al modelo de *núcleo-halo*, se mostró que el valor del parámetro de intersección de la función de correlación es afectado por la presencia de una fracción significativa de piones del núcleo que provienen del decaimiento de resonancias cuya vida

media es larga, pero que se mueven lentamente. El estudio de la evolución de estas dos componentes del núcleo, con la energía de la colisión, puede mejorar la intuición para buscar señales de fenómenos críticos en estudios de femtoscopía.

Los resultados de este trabajo se reportaron en forma de artículo en la Ref. [1].

Abstract

In the study of relativistic heavy-ion collisions, the determination of the space-time structure and size of the interaction region between the colliding nuclei has been a primordial tool to study the properties of the strongly interacting systems that are produced in this kind of collisions. The use of quantum correlations to determine the size and space-time structure of these regions is sometimes referred to as femtoscopy.

In this work, the evolution with the collision energy of the parameters that describe the two-pion correlation function, in the context of relativistic heavy-ion collisions within the NICA energy range, were studied. To this end, five million collisions of Bi+Bi, per studied energy, were simulated using the Monte Carlo generator called Ultra-relativistic Quantum Molecular Dynamics. This amount of collisions was selected to have enough statistics to perform the analysis. The effects of the quantum correlations were included by using the correlation afterburner formalism CRAB. The resulting correlation functions were fitted using Gaussian, Lorentzian and Lévy distributions, with the latter providing the best fit. The whole sample was separated into pions coming from primary origin and pions coming from the decay of long-lived resonances and it was shown that the source size of the latter is significantly larger than for the former, which is consistent with the *core-halo* picture of pion production. The effects of a non-ideal detector were simulated by introducing a momentum smearing parameter representing the minimum pair momentum and thus, by means of the Heisenberg uncertainty relation, a maximum source size that can be resolved. By resorting again to the *core-halo* picture, it was shown that the values of the correlation function intercept parameter are affected by the presence of a significant fraction of *core* pions coming from the decay of long-lived but slow-moving resonances. The study of the evolution of these two core components with the collision energy can provide useful insights to look for signs of criticality in femtoscopy studies.

Reference [1] is the article where the results of this work were reported.

Contents

Agradecimientos

A lo largo de mis estudios de maestría, y en particular durante la elaboración de esta tesis, he recibido un enorme apoyo por parte de una grandísima cantidad de personas, tanto a nivel personal como académico. A todos, ¡gracias!

Dentro de los agradecimientos académicos, quisiera mencionar a mi asesor, el Dr. Alejandro Ayala, por muchísimas cosas, en particular por todas las enseñanzas, enriquecedoras discusiones y sesiones de trabajo, ¡incluso a extraños tiempos y distantes rincones de este planeta! y por proponerme e invitarme a participar en este y otros interesantísimos cálculos.

A mi tutora, la Dra. Ivonne Maldonado, por las enseñanzas, las enriquecedoras discusiones, las sesiones de programación, por recibirme y ayudarme a sobrevivir en Dubná.

A mi tutora, la Dra. Malena Tejeda, por las enseñanzas, las enriquecedoras discusiones, las referencias que me recomendó.

A la Dra. Isabel Domínguez, por las discusiones y por darme acceso al cluster de la UAS, en donde parte de los resultados de esta tesis fueron calculados.

Al Mtro. Luciano Díaz, por la ayuda con el cluster del ICN.

A los estudiantes del Dr. Alejandro Ayala, por los comentarios que me hicieron cuando les platicaba los avances de este proyecto.

A los miembros del jurado, por los comentarios que me hicieron para mejorar el contenido de esta tesis.

Al Instituto de Ciencias Nucleares, por las facilidades recibidas durante mis estudios, por el apoyo económico para ir a la CERN Latin-American School of High-Energy Physics (CLASHEP) en Chile y presentar los avances de este trabajo, así como por el uso del cluster para hacer los cálculos de esta tesis.

Al JINR, por recibirme y por el uso de su infraestructura de cómputo que utilicé para obtener algunos de los resultados de este trabajo.

Al Consejo Nacional de Humanidades, Ciencias y Tecnologías (CONAHCYT) de México, por la beca que recibí como parte del Sistema Nacional de Posgrados (SNP) y por el apoyo económico para participar en la XX Escuela Mexicana de Partículas y Campos en Mérida.

A la División de Partículas y Campos de la Sociedad Mexicana de Física, por el apoyo económico para ir a la CLASHEP y asistir a la XX Escuela Mexicana de Partículas y Campos en Mérida.

Dentro de los agradecimientos personales, quiero mencionar a mi mamá, Rosalia y a mi papá, Abel, por todo. En particular por ayudarme a revisar este texto.

A mi familia: mi hermana, Valentina, mis tíos y primos. A mis amigos: todos.

Finalmente, a todos los grandes maestros que tuve en este periodo.

"A knowledge of distances and dimensions is the basic necessity for a good concept of the universe"

Anton Pannekoek

CHAPTER 1

Introduction

One of the fundamental quests that the human kind has ever posed to themselves is the understanding of the fundamental pieces that form matter, and in particular, the one that forms us. At the beginning of the 20th century, humanity learned that the so-thought indivisible elements that compose us, the atoms, are divisible and have a structure composed of a nucleus, made of protons (and later, after its discovery, neutrons), as well as a cloud of electrons.

The problem that arose with that model was that the particles that compose the nuclei should not maintain together since there is an electrostatic repulsive force that repels the charged particles of the same electric sign (the protons). Hence, it was deducted that another force, much stronger than the repulsive electromagnetic force, should exist. Almost half a century later, humanity realized that protons and neutrons are not fundamental particles, but that are composed of quarks and gluons. Our modern understanding of how quarks and gluons interact between themselves is a relativistic quantum field theory called Quantum Chromodynamics (QCD), which is an SU(3) Yang–Mills theory.

As in most quantum field theories, exact calculations in QCD are difficult to perform. Even more, due to the significant value at low energies ($\simeq 200$ MeV) of the QCD coupling constant, perturbative calculations are not always valid, and therefore, the predictions of QCD are still unknown under certain regimes. According to the current standard model of particle physics, QCD is a vector theory[1], which includes the three generations of quarks,

[1] In this context, a vector theory refers to the fact that the left- and right-handed components of the quark fields couple in the same manner to the gluon field. The electroweak theory is an example of a theory where this does not happen: the left-handed components of the fermion fields couple differently than the

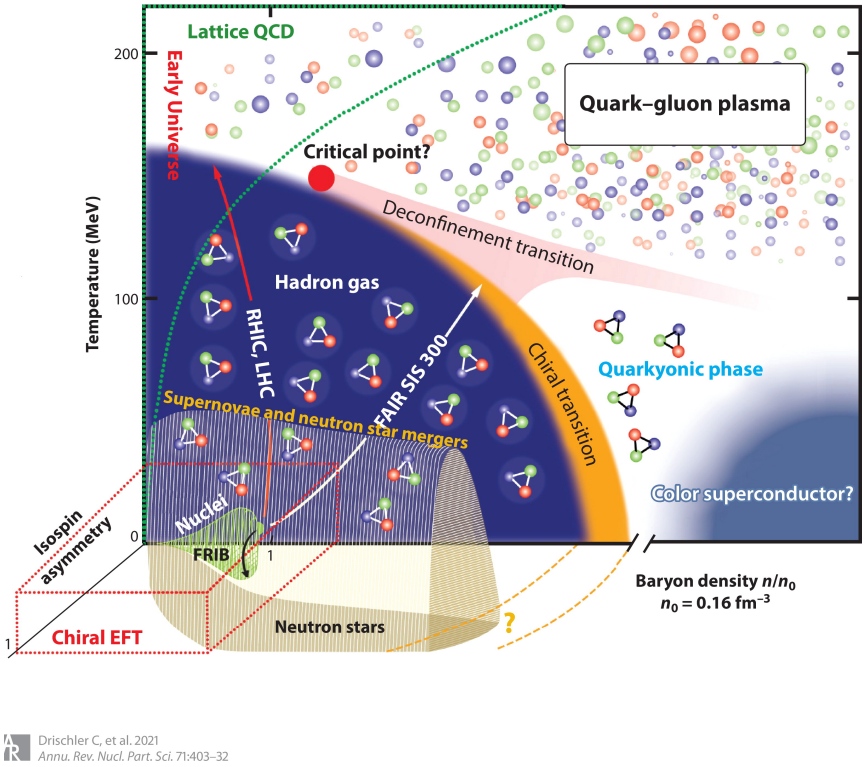

Figure 1.1: The conjectured QCD phase diagram in the temperature vs. baryon density (baryonic chemical potential) plane, and the isospin asymmetry (isospin chemical potential). Credits: C. Drischler, J. W. Holt and C. Wellenhofer, taken from Ref. [2].

each one composed of two flavours. Consequently, the QCD beta function, which describes the rate of change of the coupling constant, is negative. This means that the coupling constant decreases at higher energies, from which the asymptotic freedom property of QCD is deducted. Due to this asymptotic freedom, it is possible to deconfine the quarks and gluons from the hadrons in higher energy configurations, such as the quark - gluon plasma (QGP).

In particular, the exploration of the QCD phase diagram, i.e., of the different states of matter that exist at different temperatures, baryon chemical potential, magnetic fields, isospin chemical potential, and other variables, has drawn significant attention of the High–Energy Physics community over the last decades. Figure 1.1 shows the conjectured QCD phase diagram in the temperature vs. baryon density (baryonic chemical potential) plane, and the isospin asymmetry (isospin chemical potential). The regions of low temperature and high baryon chemical potential are especially fascinating because of the real-life system's

right-hand components to the gauge fields.

that exists these conditions. These include the innermost parts of compact stars and the interaction region at the initial moments of low energy relativistic heavy–ion collisions. One of the most intriguing aspects of the QCD phase diagram is related to the nature of the phase transition between the different states, since it has been realized that at zero baryo-chemical potential, the transition between the hadronic and the QGP phases is a smooth crossover; while at zero temperature, it is a first-order phase transition [3]. This behaviour implies that the order of the phase transition changes for different values of temperature and baryo-chemical potential, thus signalling the existence of a critical endpoint (CEP) where the first-order phase transition ends and the second-order phase transition begins.

However, due to the difficulties to obtain exact results in the temperature and baryo-chemical potential regime, where the CEP might be located, there have been only estimations of its location with Lattice QCD techniques, as well as effective models; nevertheless, its location over the phase diagram is widely spread. On the same line, there are regions where it has been shown that the CEP cannot be $145 \leq T_C \leq 155$ MeV and $\mu_{B,C}/T \leq 2$ MeV [2] [4].

Along the coexistence curve between the different phases, physical quantities such as the energy and baryonic densities, chiral condensate, among others, or their derivatives might have a discontinuous behaviour. But near the critical point, these discontinuities vanish since the two phases become identical. The system's behaviour near the critical point induces a variety of characteristic phenomena, called critical phenomena, which are due to the thermal fluctuations of the system and are the generators of long-range correlations. In the limit where the correlation length becomes infinite, the long-range thermodynamic fluctuations can be described by a conformal field theory, defined as the infrared fixed point of a renormalization group evolution of the system [3].

Nonetheless, the above mentioned phenomenology corresponds to static systems of infinite volume, but if the system has a finite size, the maximum correlation length must be limited by the system size, which in the case of relativistic heavy-ion collisions is, at most, 10 fm. Even more, since the system is not around the critical point for a long time, the correlation length does not achieve its equilibrium value but is related to the characteristic time scale in which the system is around the critical point, i.e., since the typical evolution times of the system are around 7-10 fm, the correlation length will be around 2-3 fm [3, 5].

To summarize what has been said until this point, the strongly interacting systems that are created in the collisions of relativistic heavy-ions, are short-lived and have collective properties that permeate the evolution of the system and can be used to test the theory of strong interactions, QCD. There are several interesting measurements that can be used to test, whether a QGP is formed during heavy-ion collisions. One proposed method is to check if the production of the J/Ψ meson is suppressed in these collisions compared to proton+proton collisions. Additionally, a technique called femtoscopy [6], which is based on

[2] Throughout this work, natural units, where $c = \hbar = k_B = 1$, will be used, unless it is noted otherwise.

the Hanbury-Brown and Twiss effect [7, 8], has been developed to determine the size and structure of the interaction region between the colliding ions in terms of space and time.

By the end of the 20th century, several experimental facilities were founded with the aim of colliding nuclei at very high-energies to study the formation and the properties of the QGP: Super Ion Synchrotron (SIS) at the GSI Helmholtz Center for Heavy Ion Research, in Germany; Relativistic Heavy Ion Collider (RHIC) and Alternating Gradient Synchrotron (AGS), both at Brookhaven National Laboratory (BNL), in the United States; Super Proton Synchrotron (SPS) and Large Hadron Collider (LHC), both at the European Center for Nuclear Research (CERN) in France and Switzerland, as well as future facilities like the Facility for Antiproton and Ion Research (FAIR) at the GSI Helmholtz Center for Heavy Ion Research, in Germany; and the Nucleotron-based Ion Collider fAcility (NICA) complex at the Joint Institute for Nuclear Research (JINR) in Russia. This last facility will have, as part of its heavy-ion collision experiments, the Multi-Purpose Detector (MPD), whose main scientific purpose is "to search for novel phenomena in the baryon-rich region of the QCD phase diagram by means of colliding heavy nuclei (mostly bismuth, lead and gold) in the range of 4 GeV $\leq \sqrt{s_{NN}} \leq$ 11 GeV" [9]. As it has been said, the MPD experiment is currently under construction and is expected to have its first experimental run in 2025.

The MPD detector is shown in Figure 1.2 with its various subsystems, including a 3-D tracking system of detectors, whose central detector is the Time Projection Chamber (TPC); and a particle identification system composed of the Electromagnetic (ECal) and Forward Hadronic (FHCal) calorimeters, Time of Flight (ToF) and Fast Forward detectors [9].

The purpose of this work is to study, with the use of femtoscopic techniques and within the *core-halo* picture, how the parameters that characterize the size of the whole interaction region, the sizes of the *core* and the *halo* evolve as a function of the collision energy, within the energy range of the MPD detector at the NICA complex. To this end, simulations of Bi+Bi collisions were made at $\sqrt{s_{NN}} = 4.0$, 5.8, 7.7, and 9.2 GeV with the Monte Carlo event generator UrQMD, and the correlations were added with the CRAB formalism (see Chapters 2, 3, and 4 for details). The results of this work were reported in the form of an article in Ref. [1].

This work is organized as follows: in Chapter 2, the formalism of femtoscopy and its use to compute the two-pion correlation function is explained in a theoretical sense, as well as from the Monte Carlo simulations point of view. In Chapter 3, the Monte Carlo simulations are explained, and the main characteristics of the output of the performed simulations are presented. In Chapter 4, the results of the parameters that characterize the interaction region are reported together with their evolution as a function of the collision energy, considering the case of ideal resolution and finite resolution, which seeks to resemble an actual experimental case. To avoid repetition in this chapter, only the complete analysis is presented for one of the simulated collision energies. Nevertheless, the complete analysis for the whole set of explored energies is presented for the interested reader in Appendix A for the case of ideal resolution and in Appendix B for the case of finite resolution. Finally, Chapter 5 presents a summary and the conclusions of this work.

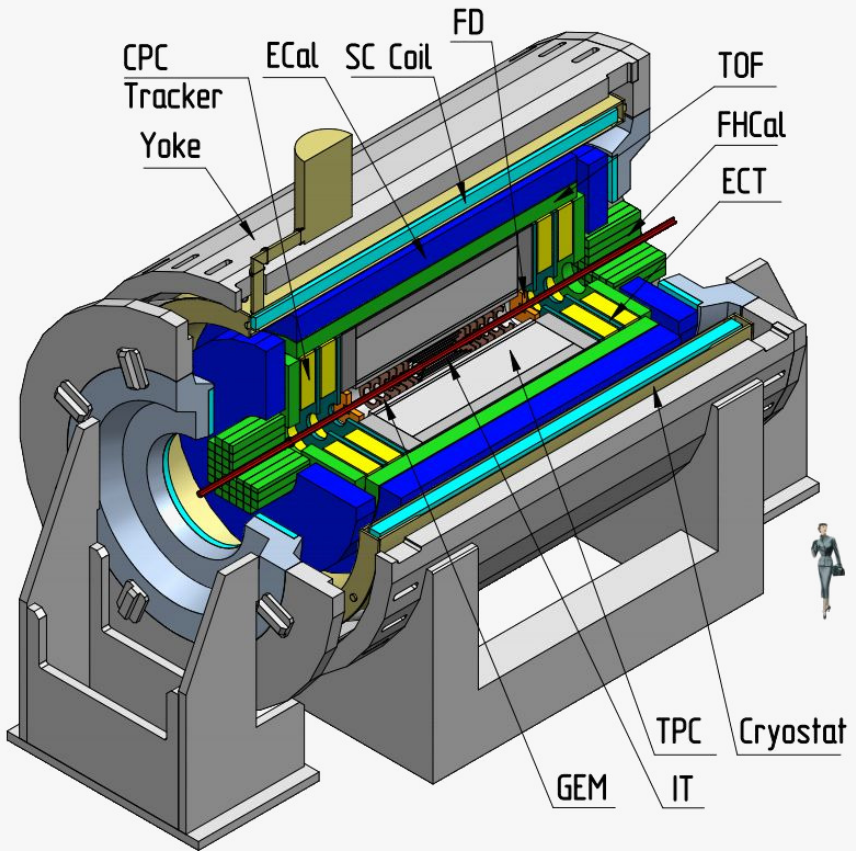

Figure 1.2: Schematic view of the MPD experiment in the first stage of operation with its inner components. The detector consists of three major parts: the central detector and two forward detectors. The time-projection chamber, time of flight system, electromagnetic calorimeter, and fast-forward–detectors are shown. Credits: MPD collaboration, taken from Ref. [9]

CHAPTER 2

The two-pion correlation function

In several domains of Physics, the object of study is not directly accessible due to its size, lifetime, or distance to the observers. Hence, we can focus on the emissions of this object, called source, and infer its properties from the particles that form these emissions. In other words, we can characterize the space-time structure of the source by measuring its emitted particles. The technique that uses the interference of two identical particles emitted from chaotic sources to determine the angular size of stars by measuring the arrival-time correlation of photons, was developed by Hanbury-Brown and Twiss [7, 8]. A few years later, G. Goldhaber, S. Goldhaber, W.-Y. Lee and A. Pais [10] realized that a similar technique could also be applied to study the interaction region formed in proton-antiproton collisions and to determine its size with identical pions. Notice, however, that there are fundamental differences between the two techniques: in the latter, the source is short-lived, evolves in space-time, and the measurements consist of momentum correlations of outgoing particles, while in the other case, the sources are static and long-lived and require experimental filters and assumptions to consider the simultaneous emission of two photons [11]. The term *femtoscopy*, coined by Lednicky [6], refers to studies and measurements that provide spatio-temporal information.

2.1 The Formalism of identical particle femtoscopy

We will start the discussion of the formalism and ideas behind the identical two-particle correlation function, following Ref. [12]. The single-particle momentum distribution is

defined as

$$\mathcal{P}_1(\mathbf{p}) \equiv \frac{\mathrm{d}^3 N}{\mathrm{d}p^3}, \tag{2.1}$$

where N is the total number of particles, also called the total multiplicity. This single particle momentum distribution measures the probability of emission of a particle with momentum $\mathbf{p}$. In a similar manner, the two-particle momentum distribution, viz. the probability that a particle of momentum $\mathbf{p}_2$ is emitted simultaneously with a particle of momentum $\mathbf{p}_1$ is

$$\mathcal{P}_2(\mathbf{p}_1, \mathbf{p}_2) \equiv \frac{\mathrm{d}^6 N}{\mathrm{d}p_1^3\, \mathrm{d}p_2^3}. \tag{2.2}$$

When the particle emission processes are independent of each other, the two-particle momentum distribution can be factorized as the product of single-particle momentum distributions

$$\mathcal{P}_2(\mathbf{p}_1, \mathbf{p}_2) = \left(\frac{\mathrm{d}^3 N}{\mathrm{d}p_1^3}\right)\left(\frac{\mathrm{d}^3 N}{\mathrm{d}p_2^3}\right). \tag{2.3}$$

When the above factorization is not valid, it is due to the fact that the emission probability of one particle affects the other, in other words, the emission processes are not independent but correlated. There are several reasons for the particles to be correlated: energy-momentum conservation (e.g., pair annihilation), a product of decay, and the quantum nature of the particles. This last reason is caused by the enhancement of the probability of emission of a pair of bosons if their momenta are similar. In contrast, the probability of emission of a pair of fermions is reduced if their momenta are similar. Recalling that the wave function of a many-body system of identical particles is symmetric (bosons) or anti-symmetric (fermions) under the exchange of a single particle.

We can express the single- and two-particle momentum distributions in a more concrete form. To this end, following Ref. [13], let us assume a dilute system of indistinguishable and non-interacting bosons, the occupation number of a state with a set of quantum numbers ω, is given by

$$N_\omega = \frac{1}{\exp(E_\omega - \mu)/T - 1}, \tag{2.4}$$

where E_ω is the energy of the state, μ is the chemical potential associated with the particle number density, and T is the system temperature. Since the chemical potential does not correspond to a strictly speaking conserved quantity, it cannot be included in the Hamiltonian and thus in the Lagrangian in the same way that a conserved quantity would be included: $\hat{H} \to \hat{H} - \mu\hat{Q}$, with $\hat{Q}$ the conserved charged. In this sense, this chemical potential corresponds to an effective description of the (in average) approximately conserved number of particles [13]. Let us assume that, in configuration space, the wave-function satisfies the normalization condition

$$\int d^3 r\, \psi_\omega^*(\mathbf{r}, t) \overleftrightarrow{\frac{\partial}{\partial t}} \psi_\omega(\mathbf{r}, t) = 1, \tag{2.5}$$

and its Fourier transform is

$$\psi_\omega(\mathbf{p}) = \int d^3r\, e^{-\,i\mathbf{p}\cdot\mathbf{r}}\psi_\omega(\mathbf{r}). \tag{2.6}$$

Given that the wave-function of the particles in momentum space, ψ_ω, is properly normalized according to Eq. (2.5), then it is possible to write the single-particle momentum distribution as

$$\mathcal{P}_1(\mathbf{p}) \equiv \frac{\mathrm{d}^3N}{\mathrm{d}p^3} = \frac{1}{(2\pi)^3}\sum_\omega 2E_\omega N_\omega \psi^*_\omega(\mathbf{p})\psi_\omega(\mathbf{p}). \tag{2.7}$$

The total number of particles can be shown to be obtained from

$$N = \sum_\omega \frac{1}{\exp(E_\omega - \mu)/T - 1}. \tag{2.8}$$

For a totally chaotic particle source, which happens when the emission can be characterized as thermal and hence without any classical (coherent) component, the two-particle momentum distribution is given by

$$\mathcal{P}_2(\mathbf{p}_1,\mathbf{p}_2) \equiv \frac{\mathrm{d}^6N}{\mathrm{d}p_1^3\,\mathrm{d}p_2^3} = \mathcal{P}_1(\mathbf{p}_1)\mathcal{P}_1(\mathbf{p}_2) + \left|\frac{1}{(2\pi)^3}\sum_\omega 2E_\omega N_\omega \psi^*_\omega(\mathbf{p}_1)\psi_\omega(\mathbf{p}_2)\right|^2, \tag{2.9}$$

from where the two-particle correlation function C_2 is expressed in terms of the single- and two-particle momentum distributions as

$$C_2(\mathbf{p}_1,\mathbf{p}_2) \equiv \frac{\mathcal{P}_2(\mathbf{p}_1,\mathbf{p}_2)}{\mathcal{P}_1(\mathbf{p}_1)\mathcal{P}_1(\mathbf{p}_2)} = 1 + \frac{\left|\sum_\omega E_\omega N_\omega \psi^*_\omega(\mathbf{p}_1)\psi_\omega(\mathbf{p}_2)\right|^2}{\sum_\omega E_\omega N_\omega \left|\psi(\mathbf{p}_1)\right|^2 \sum_\omega E_\omega N_\omega \left|\psi(\mathbf{p}_2)\right|^2}. \tag{2.10}$$

When the particle source is not totally chaotic, i.e., when there is a degree of coherence in the emission of particles, which happens when the fraction of particles in the ground state is not negligible, its contribution to the correlation function must be separated as

$$\begin{aligned} C_2(\mathbf{p}_1,\mathbf{p}_2) = 1 &+ \frac{\left|\sum_{\omega\neq\omega_0} E_\omega N_\omega \psi^*_\omega(\mathbf{p}_1)\psi_\omega(\mathbf{p}_2)\right|^2}{\sum_\omega E_\omega N_\omega \left|\psi(\mathbf{p}_1)\right|^2 \sum_\omega E_\omega N_\omega \left|\psi(\mathbf{p}_2)\right|^2} \\ &+ \frac{\left|E_{\omega_0} N_{\omega_0} \psi^*_{\omega_0}(\mathbf{p}_1)\psi_{\omega_0}(\mathbf{p}_2)\right|^2}{\sum_\omega E_\omega N_\omega \left|\psi(\mathbf{p}_1)\right|^2 \sum_\omega E_\omega N_\omega \left|\psi(\mathbf{p}_2)\right|^2}, \end{aligned} \tag{2.11}$$

where ω_0 represents the set of quantum numbers corresponding to the ground state. Notice that when particles coming from the ground state are treated separately from the ones coming from excited states, the correlation function fails to reach its maximum possible value $C_2(q=0)_{\max} = 2$, as the ground state occupation number increases. This happens

since for $\mathbf{q} = \mathbf{p}_1 - \mathbf{p}_2 = 0$, the numerator and the denominator of the second and third terms on the right-hand side of Eq. (2.11) are no longer equal, as they were in Eq. (2.10) for the case of a totally chaotic source.

Usually, the correlation function is reported as a function of the magnitude of the momentum difference $q = |\mathbf{p}_1 - \mathbf{p}_2|$, and for fixed values of the average momentum $K = \frac{1}{2}(p_1 + p_2)$, since the Jacobian of the transformation onto these variables is one and the on-shell constraint

$$K \cdot q = \frac{1}{2}\left(p_1^2 - p_2^2\right) = \frac{1}{2}\left(m_1^2 - m_2^2\right) = 0, \tag{2.12}$$

implies that $q_0 = \frac{\mathbf{q}\cdot\mathbf{K}}{K_0}$, and hence, only three of the four components of q are independent and the dependence of the correlation function on q can be translated into a dependence on $\mathbf{q}$. Moreover, if the two particles of the pair have a similar energy, then K is approximately on-shell and the correlation function becomes only a function of $\mathbf{q}$ and $\mathbf{K}$. Thus, the two-particle correlation function C_2 depends on the six kinematical variables corresponding to the two particles momenta as well as parametrically on μ, T, and other factors that affect the system, such as its finite volume, magnetic field, and expansion velocity, among others [13, 14]. The properties of the correlation function can be more easily studied by setting particular configurations of these kinematical variables. Notice that the most important dependence of the correlation function is on the relative momentum since it is more dependent on $\mathbf{q}$ than on the average momentum [15].

The two-particle correlation function can also be related to the particle emitting source function in phase space, $S(x, p)$, which is the quantum-mechanical analogue of the classical probability of emitting a particle at the phase-space point (x, p). It is represented by the covariant Wigner transformation of the source density matrix [16]. If dynamical correlations are neglected, the single- and two-particle momentum distributions can be written as

$$\mathcal{P}_1(p) = \int d^4x\, S(x,p)\, |\Psi_p(x)|^2\,, \tag{2.13}$$

$$\mathcal{P}_2(p_1,p_2) = \int d^4x_1 d^4x_2\, S(x_1,p_1)S(x_2,p_2)\, |\Psi_{p_1,p_2}(x_1,x_2)|^2\,, \tag{2.14}$$

where Ψ_p and Ψ_{p_1,p_2} are the single- and two-particle symmetrized, properly normalized wave functions. Hence, the two-particle correlation function can be written as

$$C_2(p_1,p_2) = \frac{\int d^4x_1 d^4x_2\, S(x_1,p_1)S(x_2,p_2)\, |\Psi_{p_1,p_2}(x_1,x_2)|^2}{\int d^4x_1\, S(x_1,p_1)\, |\Psi_{p_1}(x_1)|^2 \int d^4x_2\, S(x_2,p_2)\, |\Psi_{p_2}(x_2)|^2}. \tag{2.15}$$

Since the squared single-particle wave function must be properly normalized to unity, it can be omitted from the previous expression. Usually, the squared two-particle wave function serves as a weight and the particle emitting source function contains all space-time information about the source [11]. Following Ref. [11], we can write the single- and

two-particle momentum distributions in terms of T-matrix elements. Beginning with the single-particle,

$$\mathcal{P}_1(p) = \int d^4x\, S(x,p) = \sum_{F'} \left| \int d^4x\, T_{F'}(x) e^{-ip\cdot x} \right|^2, \tag{2.16}$$

$$S(x,p) = \sum_{F'} \int d^4\delta x\, T^*_{F'}(x+\delta x/2) T_{F'}(x-\delta x/2) e^{ip\cdot\delta x}, \tag{2.17}$$

where F' is the state of all other particles in the system. Recall that all the particle interactions with the residual system are incorporated into the T- matrix formalism. Notice that, for example, final-state Coulomb interactions can be incorporated in Eq. (2.16) by substituting the phase in $\mathcal{P}_1$ with an outgoing Coulomb wave function or by including them in the T matrix. Hence, there exists the possibility to incorporate mean-field interactions in the T matrix or to incorporate them into the evolution matrix.

Equations (2.16) and (2.17) have four underlying assumptions that must be discussed before proceeding [11]:

Assumption 1: *Higher order symmetrization can be neglected.* Equation (2.16) implies that all the particles with asymptotic momentum p must have had their last interaction with the source at some point x. If there are $N > 1$ particles, then it must be considered $T(x_1, \cdots, x_N)$ and taken into account that the evolution matrix is no longer a simple phase, but includes $N!$ interference terms. The single-particle momentum distribution can be obtained by integrating over the remaining $N-1$ momenta.

Assumption 2: *The emission process is initially uncorrelated.* Equation (2.16) requires that the emission is independent. In other words, the two-particle matrix elements factorize: $T_{F''}(x_1,x_2) = T_{F'_1}(x_1) T_{F'_2}(x_2)$. If multi-particle symmetrization can be neglected, the two-particle evolution operator factorizes into a center-of-mass and a relative operator: $U(x_1,x_2;p_1,p_2) = e^{iK\cdot(x_1+x_2)}\Big(u_{q'}(x'_1-x'_2) + u_{q'}(x'_2-x'_1)\Big)/\sqrt{2}$, where the prime denotes quantities in the center-of-mass frame, where $\mathbf{K}=0$. Then, the two-particle momentum distribution can be expressed in terms of the single-particle momentum distributions as

$$\begin{aligned}\mathcal{P}_2(p_1,p_2) = \int d^4x_1 d^4x_2 d^4\tilde{q}\, S_1\Big(x_1, (E'_1/M_{\rm inv})K + \tilde{q}\Big) S_2\Big(x_2, (E'_2/M_{\rm inv})K + \tilde{q}\Big) \\ \times d^4\delta r'\, e^{i\tilde{q}\cdot\delta r'} u^*_{q'}(x'_1 - x'_2 + \delta r'/2) u_{q'}(x'_1 - x'_2 - \delta r'/2),\end{aligned} \tag{2.18}$$

where $M_{\rm inv}$ is the pair invariant mass.

Assumption 3: *Smoothness approximation.* In general, Eq. (2.18) is very difficult to determine, as it requires to evaluate the particle emitting source function off-shell. If it is assumed that the particles do not interact, aside from their identical particles

interference, then $u_q(x_1 - x_2) = \left(e^{iq\cdot(x_1-x_2)} + e^{iq\cdot(x_2-x_1)}\right)/\sqrt{2}$ and the integrals over $\tilde{q}$ and $\delta r'$ can be analytically done. Hence,

$$\mathcal{P}_2(p_1,p_2) = \int d^4x_1 d^4x_2 \left\{ S(x_1,p_1)S(x_2,p_2) + S(x_1,K)S(x_2,K)\cos\Big((p_1-p_2)\cdot(x_1-x_2)\Big)\right\}. \tag{2.19}$$

The source functions for the interference term are evaluated off-shell for non-zero relative and average momentum. The smoothness approximation replaces $S(x_1,K)S(x_2,K)$ with either $S(x_1,E(\mathbf{K}),\mathbf{K})S(x_2,E(\mathbf{K}),\mathbf{K})$ or with $S(x_1,p_1)S(x_2,p_2)$.

Assumption 4: *Equal time approximation.* The smoothness approximation is used to neglect the $\tilde{q}$ dependence in the product of source functions of Eq. (2.18). In the presence of final-state interactions, this assumption is more stringent because the relevant range of $\tilde{q}$ extends beyond q. Hence, one obtains a δ-function constraint for $\delta r'$, and the integrand of Eq. (2.18) is proportional to the squared evolution matrix $|u_{q'}(x'_1 - x'_2)|^2$. This evolution matrix has non-zero time components, which must be neglected in order to identify it with the relative wave function.

Based on the previous four assumptions (particularly on Assumption 3), one can find that the two-particle correlation function can be written as

$$C_2(\mathbf{q},\mathbf{K}) = 1 + \int d^3r' \mathcal{S}_{\mathbf{K}}(\mathbf{r}')\left[|\Psi_{K,q}(\mathbf{q}',\mathbf{r}')|^2 - 1\right], \tag{2.20}$$

$$\mathcal{S}_{\mathbf{K}}(\mathbf{r}') \equiv \frac{\int d^4x_1 d^4x_2\; S_1(x_1,\bar{p}_1)S_2(x_2,\bar{p}_2)\delta(\mathbf{r}' - \mathbf{x}'_1 - \mathbf{x}'_2)}{\int d^4x_1 d^4x_2\; S_1(x_1,\bar{p}_1)S_2(x_2,\bar{p}_2)}, \tag{2.21}$$

where $\bar{\mathbf{p}}_a = 2m_a\mathbf{K}/(m_1+m_2)$ and $\bar{p}_a^0 = E(\bar{\mathbf{p}}_a)$. The previous equation allows us to consider the squared wave function as the kernel from which one transforms from the coordinate space basis to the relative momentum basis. Additionally, the two-particle correlation function provides information about the distribution of relative positions of particles, $\mathcal{S}_{\mathbf{K}}$, with identical velocities and average momentum K, as they move in their asymptotic state. Thus, the analysis of the correlation function cannot be used to determine the size of the entire source, but it can be used to determine the dimensions of the "region of homogeneity", i.e., the size and shape of the phase space cloud of outgoing particles whose velocities have a specific magnitude and direction [11]. If the collective expansion of the produced matter is strong, as it occurs in central collisions, then the region of homogeneity is significantly smaller than the entire source volume [11, 14].

These four assumptions are consistent with a semi-classical formalism, since the quantum-mechanical particle emission probability, defined by the T-matrix elements, is approximated by classical particle emitting source functions.

Since in heavy-ion collisions the particles that are more abundantly produced are pions, we will focus the discussion on the two-pion correlation function. However, most of what will be stated below is still valid for identical bosons femtoscopy.

On the other hand, taking into account these assumptions, neglecting final-state interactions and higher order effects, the squared wave functions are [17]

$$|\Psi_p(x)|^2 = 1 \tag{2.22}$$

$$|\Psi_{p_1,p_2}(x_1,x_2)|^2 = 1 + \cos\Big((p_1-p_2)(x_1-x_2)\Big). \tag{2.23}$$

Notice that, from Eq. (2.20), the curvature of C_2 at vanishing relative momentum can be related to the mean square separation of the three-dimensional shape of $\mathcal{S}_{\mathbf{K}}(\mathbf{r})$ [11]

$$-\left.\frac{\mathrm{d}^2 C_2(\mathbf{q},\mathbf{K})}{\mathrm{d}q_i'\mathrm{d}q_j'}\right|_{q=0} = \langle r_i r_j\rangle = \int d^3r\, \mathcal{S}_{\mathbf{K}}(\mathbf{r}) r_i r_j. \tag{2.24}$$

This illustrates the relation between specific space-time information and specific features of the correlation function [11].

Notice that if we identify the Fourier-transformed source function,

$$\tilde{S}(q_x,p) = \int d^4x\, e^{iq_x\cdot x} S(x,p) \tag{2.25}$$

then one can write the two-pion correlation function as [17]

$$C_2(p_1,p_2) = 1 + \mathrm{Re}\left[\frac{\tilde{S}(q,p_1)\tilde{S}^*(q,p_2)}{\tilde{S}(0,p_1)\tilde{S}^*(0,p_2)}\right], \tag{2.26}$$

where $q = p_1 - p_2$. Now, recall that the pion production in a relativistic heavy-ion collision is described by the equations of motion of the pion field, $\phi(x)$,

$$\left(\Box + m^2\right)\hat{\phi}(x) = \hat{J}(x), \tag{2.27}$$

where $\Box$ is the D'Alembert operator and $\hat{J}$ is the current operator. The latter operator can be approximated by a classical commuting space-time function $J(x)$, which means that at freeze-out, when the pions stop interacting, the emitting source is assumed not to be affected by the emission of a single pion [18]. Following Ref. [18], for a classical source, the pion in the final state is a coherent state $|J\rangle$, which is an eigenstate of the annihilation operator

$$\hat{a}_{\mathbf{p}}\,|J\rangle = i\tilde{J}(\mathbf{p})\,|J\rangle\,, \tag{2.28}$$

where $\tilde{J}$ is the on-shell Fourier transformed classical source. By assuming that the classical current is a superposition of independent elementary source functions J_0, then

$$\tilde{J}(\mathbf{p}) = \sum_{i=1}^{N} e^{i\varphi_i} e^{i\mathbf{p}\cdot\mathbf{x}_i}\tilde{J}_0(p-p_i), \tag{2.29}$$

with φ_i a set of random phases, which characterizes chaotic particle emission. In this case, the average for an operator $\hat{\mathcal{O}}$, specifying the particle spectra is

$$\left\langle \hat{\mathcal{O}} \right\rangle = \sum_{N=0}^{\infty} P_N \prod_{i=1}^{N} \int d^4x_i d^4p_i \, \rho(x_i, p_i) \int_0^{2\pi} \frac{d\varphi_i}{2\pi} \left\langle J \right| \hat{\mathcal{O}} \left| J \right\rangle , \tag{2.30}$$

where P_N is the properly normalized probability distribution for N sources and $\rho(x_i, p_i)$ is the normalized probability that describes the distribution of the elementary sources J_0 in the phase-space. Using this, as well as the commutation relations between the creation and the annihilation operators, independent particle emission and the absence of final-state interactions, we can factorize the two-pion momentum distribution, $\mathcal{P}_2$, in terms of single-pion momentum distributions, $\mathcal{P}_1$, as

$$\mathcal{P}_2(\mathbf{p}_1, \mathbf{p}_2) = \frac{\langle N(N-1) \rangle_P}{\langle N \rangle_P^2} \left(\mathcal{P}_1(\mathbf{p}_1) \mathcal{P}_1(\mathbf{p}_2) + \left| \bar{S}_J(\mathbf{p}_1, \mathbf{p}_2) \right|^2 \right) , \tag{2.31}$$

where

$$\bar{S}_J(\mathbf{p}_1, \mathbf{p}_2) \equiv \sqrt{E_1 E_2} \left\langle \hat{a}^\dagger_{\mathbf{p}_1} \hat{a}_{\mathbf{p}_2} \right\rangle = \sqrt{E_1 E_2} \left\langle \tilde{J}^*(\mathbf{p}_1) \tilde{J}(\mathbf{p}_2) \right\rangle , \tag{2.32}$$

$\langle N(N-1) \rangle_P = \sum_{N=0}^{\infty} P_N N(N-1)$, $\langle N \rangle_P = \sum_{N=0}^{\infty} P_N N$ and N, denotes the number of sources. The source function $S(x,p)$ can be identified with the Fourier transform of the covariant quantity $\bar{S}_J(\mathbf{p}_1, \mathbf{p}_2)$. The latter is given by the Wigner transform of the density matrix associated with the classical currents

$$S_J(x, K) = \int \frac{d^4y}{2(2\pi)^3} e^{-iK\cdot y} \left\langle J^* \left(x + \frac{y}{2} \right) J \left(x - \frac{y}{2} \right) \right\rangle . \tag{2.33}$$

Hence,

$$S_J(x, K) = \langle N \rangle_P \int d^4z d^4q \, \rho(z, q) S_0(x - z, K - q), \tag{2.34}$$

with S_0 the Wigner functions of the elementary source functions, given by

$$S_0(x, K) = \int \frac{d^4y}{2(2\pi)^3} e^{-iK\cdot y} J_0^* \left(x + \frac{y}{2} \right) J_0 \left(x - \frac{y}{2} \right) . \tag{2.35}$$

By direct substitution of Eqs. (2.31) and (2.32) and assuming that the relative momenta between the particles is much smaller than the average pair momenta, then the two-pion correlation function can be written as [15, 18]

$$C_2(\mathbf{q}, \mathbf{K}) = 1 + \frac{\left| \int d^4x \, S(x, K) \, e^{iq\cdot x} \right|^2}{\int d^4x \, S(x, p_1) \int d^4y \, S(y, p_2)}, \tag{2.36}$$

and identifying the Fourier transform of the source functions, Eq. (2.25),

$$C_2(q_{\text{inv}}, K_{\text{inv}}) = 1 + \frac{\left| \tilde{S}(q_{\text{inv}}, K_{\text{inv}}) \right|^2}{\left| \tilde{S}(0, K_{\text{inv}}) \right|^2}, \tag{2.37}$$

which can be written as a function of the Lorentz invariant relative momentum $q_{\rm inv} \equiv \sqrt{q^\mu q_\mu} = \sqrt{q_0^2 - |\mathbf{q}|^2}$ and for a fixed Lorentz invariant average momentum $K_{\rm inv} \equiv \sqrt{K^\mu K_\mu} = \sqrt{k_0^2 - |\mathbf{k}|^2}$ [17, 19].

From Eq. (2.37), it can be seen that the two-pion correlation function can reach a maximum value of two at zero relative momentum, where the correlation function intercept, $C_2(q_{\rm inv} \to 0)$, is usually denoted by $C_2(q_{\rm inv} \to 0) = 1+\lambda$, with λ also known as the intercept, chaoticity or incoherence parameter, where the last two names have their origin from the relation between the coherence of the emission and the λ parameter (see Refs. [13, 20–22] for further details on the coherence properties of the emission).

2.2 The *core-halo* picture

As it has already been mentioned, different effects such as final state interactions, magnetic fields [13], expanding source boundaries [14], partial coherence [13, 20–23], particle misidentification and a finite experimental resolution [23] can prevent the intercept parameter from reaching the value of one. This can be understood in terms of the *core-halo* picture [23, 24], whereby particles that come from the decay of long-lived resonances create a component of the source with a size that may not be resolved when the corresponding width of the pair momentum difference becomes smaller than the detector resolution. In this work, we will not focus on the other effects, such as coherence, that can reduce the value of the intercept parameter. We will now proceed to present the *core-halo* picture following Ref. [16]: accounting for this possibility, the phase space pion emitting source can be modelled as a superposition of two components: a central core surrounded by an extended halo, such as is depicted in Fig. 2.1.

Recall that the experiments designed to detect the pions emitted from the collisions of heavy-ions have a minimum resolution on the pair relative, $q_{\rm min}$, as well as on their average momenta, $K_{\rm min}$. Since the Bose-Einstein enhancement of the correlation comes from the region of small relative momenta, the effect of the finite resolution must be understood within the *core-halo* picture that is based on four assumptions [24]:

Assumption 1: The phase space emission source function does not have a determinate scale, due to its power-law–like structure.

Assumption 2: The pions are emitted either from a central part, called the *core* and whose source is denoted by $S_{\rm core}$, or from the surrounding *halo*, whose source is denoted by $S_{\rm halo}$. Hence, the complete emission source can be written as

$$S = S_{\rm core} + S_{\rm halo}, \tag{2.38}$$

where each component has a Fourier transform, and the *core* is composed of pions that are produced from fragmentation or recombination of partons [25], hydrodynamic

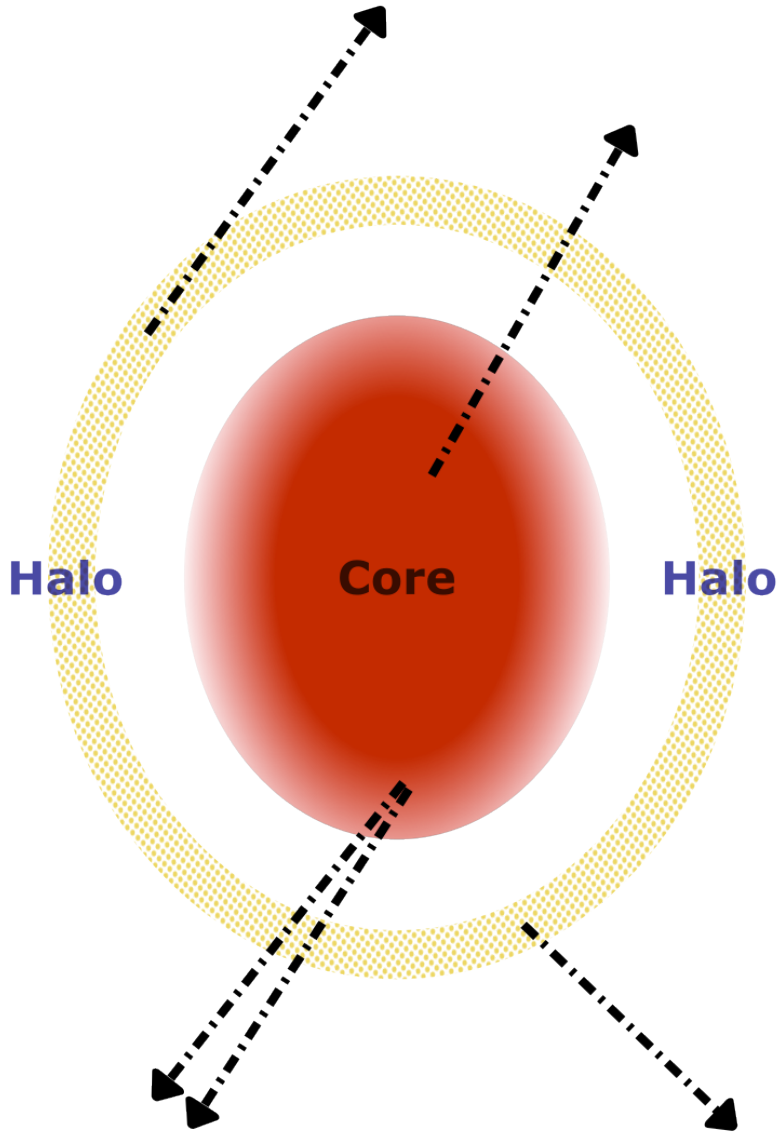

Figure 2.1: Outline of the *core-halo* picture, with the central, red gradient part representing the *core* and the spotted yellow ring representing the *halo*. The black arrows represent the pions being emitted by the *core* and the *halo*.

evolution or production from excited strings and subsequent re-scattering of the particles [26]. These processes are known as primary or direct processes.

Assumption 3: The emission source that describes the *halo* changes on a length-scale R_{halo} that is larger than $R_{\text{min}} = 1/q_{\text{min}}$, the maximum length scale that can be resolved. The length scale of the *core*, R_{core}, is smaller than the maximum resolvable scale. Thus,

$$R_{\text{core}} < R_{\text{max}} < R_{\text{halo}}. \tag{2.39}$$

Assumption 4: The fraction of pions emitted from the *core*, with respect to the total, varies slowly on the relative momentum scale.

Notice that the single-pions momentum distribution emitted from the *core* and the *halo* can be expressed, in terms of the Fourier transformed source function, as

$$\mathcal{P}_{1,\text{core}}(K_{\text{inv}}) = \int d^4x\, S_{\text{core}}(x, K_{\text{inv}}) = \tilde{S}_{\text{core}}(0, K_{\text{inv}}) \equiv N_{\text{core}}, \tag{2.40}$$

$$\mathcal{P}_{1,\text{halo}}(K_{\text{inv}}) = \int d^4x\, S_{\text{halo}}(x, K_{\text{inv}}) = \tilde{S}_{\text{halo}}(0, K_{\text{inv}}) \equiv N_{\text{halo}}, \tag{2.41}$$

and hence, $\mathcal{P}_1(K_{\text{inv}}) = \tilde{S}(0, K_{\text{inv}}) = N_{\text{core}} + N_{\text{halo}} = N$. The measured correlation function is determined for $q > q_{\text{min}}$, and any structure within the $q < q_{\text{min}}$ region will not be resolved. Since, by Assumption 3, the pions coming from the *halo* come from a length-scale larger than R_{max}, then they will create a narrow peak in the region of $q < q_{\text{min}}$, therefore $\tilde{S}_{\text{halo}}(q_{\text{inv}}, K_{\text{inv}}) \approx 0$ for $q_{\text{inv}} < q_{\text{min}}$, i.e., the Fourier transform of the emission source of the *halo* vanishes at the minimum resolution of the experiment. At zero relative momentum, this source gives the single-particle momentum distribution from the *halo*, which is not affected by the two-particle resolution [24].

Thus, for experimentally resolvable values of the relative momentum, it can be assumed that $\tilde{S}(q_{\text{inv}}, K_{\text{inv}}) \simeq \tilde{S}_{\text{core}}(q_{\text{inv}}, K_{\text{inv}})$. Therefore, the two-pion correlation function can be expressed as

$$C_2(q_{\text{inv}}, K_{\text{inv}}) = 1 + \left(\frac{N_{\text{core}}}{N_{\text{core}} + N_{\text{halo}}}\right)^2 \frac{\left|\tilde{S}_{\text{core}}(q_{\text{inv}}, K_{\text{inv}})\right|^2}{\left|\tilde{S}_{\text{core}}(0, K_{\text{inv}})\right|^2}. \tag{2.42}$$

As a consequence, in the *core-halo* picture, we can identify, for a given pair invariant momentum [16, 24, 27]

$$\lambda = \left(\frac{N_{\text{core}}}{N_{\text{core}} + N_{\text{halo}}}\right)^2, \tag{2.43}$$

which, in general, is a function of the pair average momentum. Notice that, as a consequence of the *core-halo* picture, the height of the two-pion correlation function at vanishing relative momentum is no longer two but $1 + \lambda$, where λ is related to the fraction of pions emitted

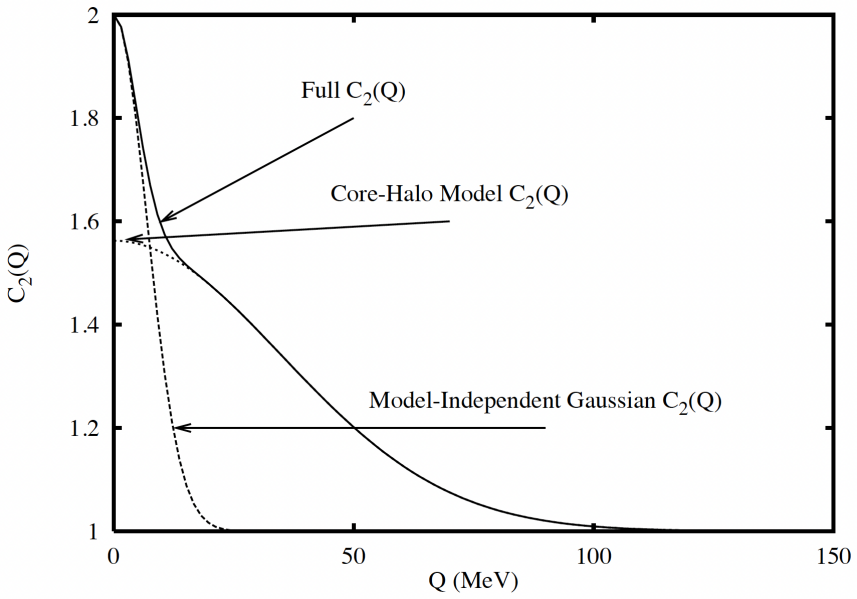

Figure 2.2: Predicted effect of the finite resolution on the two-pion correlation within the *core-halo* picture. Credits: T. Csörgő, taken from Ref.[16]

by the *core*. Hence, by measuring λ, one could infer the fraction of pions from the *core*. The effects predicted by the *core-halo* picture on the two-pion correlation picture are shown in Fig. 2.2.

2.3 Correlation functions from Monte Carlo simulations and the CRAB formalism

Nowadays, there exists a plethora of models of heavy-ion collisions, many of which have been implemented as numerical or Monte Carlo simulations. They provide an important tool for the study of these systems and, in particular, to perform femtoscopy studies on these models. The previous definitions of the two-pion correlation function are barely used when dealing with experimental or Monte Carlo produced data due to the difficulty of working with them. Instead of Eq. (2.10), it is usual to compute the two-pion correlation function from measurements or simulations as [15]

$$C_2(q,K) = \frac{\mathcal{N}_B}{\mathcal{N}_A}\frac{A(q,K)}{B(q,K)}, \tag{2.44}$$

where $A(q,K)$ is the pair relative momentum distribution of pions, which contains the femtoscopic correlations, also called the signal distribution, and $B(q,K)$ is the same as A,

but it does not contain Bose-Einstein correlations, also called the background distribution. $\mathcal{N}_A$ and $\mathcal{N}_B$ are normalization factors for A and B; most commonly, the number of pairs used to construct the distributions or $\int_{q_1}^{q_2} D(q,K)dq$, where $D(q,K)$ is either A or B and $[q_1,q_2]$ is an interval of large-q where Bose-Einstein effects no longer affect the correlation [15, 17]. An additional multiplicative factor can be included to take into account non-femtoscopic correlations (see, for example, Ref. [11]). It is usual to look for particular characteristics of the events and specific values of K to construct C_2 as a function of q, so the main dependence comes from the relative momentum.

Several techniques have been developed to construct the signal and background distributions [11], but one of the most popular is the event mixing technique, where the signal distribution is computed from the relative momentum distribution of pions coming from the same event, whereas the background distribution is computed from the relative momentum distribution of pions coming from different events that share the same characteristics as those that were used for A. This technique minimizes non-quantum-statistical correlations [15], but does not remove them entirely [28], although it must be stated that for elementary particle collisions or in low multiplicity events, the event mixing technique can violate the total energy-momentum conservation, and hence the obtained correlation can reflect non-femtoscopic as well as femtoscopic correlations [11].

However, when dealing with numerical simulations and not with experimental data, not all the available simulators include the effects of Bose-Einstein statistics, since Monte Carlo simulations are formulated via probabilities of interactions and do not take into account the quantum mechanical symmetrization effects, and hence, the simulated collisions lack Bose-Einstein correlations. Nevertheless, this could be done, in principle, by properly propagating symmetrized N-particle amplitudes from some initial condition [18]. To include this correlations, two main methods have been developed: one method is motivated by Eq. (2.20), which involves constructing a discretized version of Eq. (2.36). In the so-called "classical interpretation" of the output of the Monte Carlo simulation, the output phase-space points are identified as the pion emitting source function and the two-pion correlation function takes the form [18]

$$C_2(\mathbf{q},\mathbf{K}) = 1 + \frac{\displaystyle\sum_{m=1}^{N_{\text{ev}}} \left[\left| \sum_{i=1}^{N_m} \delta^{(\epsilon)}_{\check{\mathbf{p}}_i,\mathbf{K}}\, e^{i(q^0 \check{t}_i - \mathbf{q}\cdot\check{\mathbf{r}}_i)} \right|^2 - \sum_{i=1}^{N_m} \left(\delta^{(\epsilon)}_{\check{\mathbf{p}}_i,\mathbf{K}}\right)^2 \right]}{\displaystyle\sum_{m=1}^{N_{\text{ev}}} \left[\left(\sum_{i=1}^{N_m} \delta^{(\epsilon)}_{\check{\mathbf{p}}_i,\mathbf{p}_1} \right) \left(\sum_{j=1}^{N_m} \delta^{(\epsilon)}_{\check{\mathbf{p}}_j,\mathbf{p}_2} \right) - \sum_{i=1}^{N_m} \delta^{(\epsilon)}_{\check{\mathbf{p}}_i,\mathbf{p}_1} \delta^{(\epsilon)}_{\check{\mathbf{p}}_i,\mathbf{p}_2} \right]}, \tag{2.45}$$

where N_{ev} is the number of simulated events, N_m is the multiplicity of each event, $(\check{\mathbf{r}}_i, \check{t}_i, \check{\mathbf{p}}_i)$ are the phase-space points output of the simulation and the rectangular "bin functions",

$\delta^{(\epsilon)}_{\check{\mathbf{p}}_i,\mathbf{p}}$ are defined by

$$\delta^{(\epsilon)}_{\check{\mathbf{p}}_i,\mathbf{p}} = \begin{cases} 1/\epsilon^3 & \text{if} \quad p_j - \frac{\epsilon}{2} \leq \check{p}_{i,j} \leq p_j + \frac{\epsilon}{2} \qquad (j = x, y, z), \\ 0 & \text{else .} \end{cases} \tag{2.46}$$

In general, the value of the correlation at a particular $(\mathbf{q}, \mathbf{K})$ configuration will depend on the bin width ϵ, but accurate results require large statistics and small ϵ. There exists a variant of this method, called the "quantum interpretation", in which the output of the simulation is identified with the center of Gaussian wave packets. In both interpretations of this method, the inclusion of final-state interactions increases the complexity of the algorithm from $\mathcal{O}(N_m)$ to $\mathcal{O}(N_m^2)$ [18].

The second method, randomly samples the position of pairs of particles, regardless of their momenta. The numerator of the correlation function is then computed by generating pairs and weighting them by the square of the relative wave function, while the denominator is obtained in a similar manner, but without weighting the pairs. This method has the advantage that kinematic or experimental effects can easily be taken into account, while the first method makes a quicker calculation [11]. An example of this second method is the Correlation After Burner formalism (CRAB), developed by S. Pratt *et al.* [29, 30][1]. This formalism performs the computation of the correlation function as follows [29]:

1. Perform a dynamical simulation that yields the final momenta and space-time points of final interaction (freeze-out position) for particles of a given type.

2. Repeat the calculation many times for several impact parameters. Store the points in a different file for each impact parameter.

3. Choose pairs of particles from the same impact parameter weighted by the two-particle multiplicity and any possible impact parameter cuts that are needed.

4. Test whether the two particles will be detected by the experiment. If not, pick a new pair.

5. Boost these points to the center of mass of the pair reference frame. Calculate the pair relative wave function and square it (see Eq. (2.23)) in terms of the pair separation and their relative momentum in this reference frame, which is the invariant momentum.

6. For the numerator, bin the event according to the relative momentum, this can be done in any desired reference frame. To this bin, add the squared relative wave function as a weight.

[1] The code of CRAB, is available at the website
https://web.pa.msu.edu/people/pratts/freecodes/crab/home.html [30]

7. For the denominator, choose two separate pairs from those in part 6. As a weight, use the product of the weights of the two pairs. This would correspond to the experimental procedure of using only two-particle events to calculate the denominator.

8. Divide the bins by one another to obtain the correlation function.

This procedure includes the correlations due to averaging the impact parameter, but will not include the effects of event-to-event large-scale fluctuations. To include this effects, it is necessary to treat each event as a separate impact parameter, and hence there would be a need for much more statistics. Final-state interactions can be added at the moment of weighting the numerator by modifying the relative wave function, to include the desired effect.

The CRAB formalism became a popular tool in the field by many years, but it was later discovered that, for small systems at TeV energies, the predictions made by CRAB were not very precise, and hence, more modern versions were developed, such as "Correlation Analysis Tools using Schrödinger equation" (CATS) [31] and "Correlation Algorithm Library" (CorAL, based on CRAB) [32–34]. Some of the developed formalisms may also include final state interactions, like CRAB and the one found in Refs. [35, 36].

2.4 Parametrizations and fits of the two-pion correlation function

Once the procedure previously described for constructing the two-pion correlation function is complete, it is possible to make certain assumptions about the shape of the pion emitting source and find if the obtained correlation function is consistent with those assumptions. To begin with, and for clarity purposes, following Refs. [27, 37], let's start by considering the simplest case of a one-dimensional static pion emitting source function in phase space that can be factorized into a space-time distribution $f(x)$ and a momentum space distribution $g(p)$, i.e.,

$$S(x,p) = f(x)\, g(p), \tag{2.47}$$

where x and p are one dimensional coordinate and momentum variables, respectively. The normalization of such distributions is chosen such that

$$\int dx\, f(x) = 1 \qquad \text{and} \qquad \int dp\, g(p) = \langle n \rangle, \tag{2.48}$$

where $\langle n \rangle$ is the pion mean multiplicity. Then, the single-pion momentum distribution can be obtained as (Eq. (2.13))

$$\mathcal{P}_1(p) = \int dx\, S(x,p) = g(p). \tag{2.49}$$

Assuming a chaotic pion emission and a plane wave approximation, the two-pion, symmetrized wave function can be expressed as (Eq. (2.23))

$$\Psi_{p_1,p_2}(x_1,x_2) = \frac{1}{\sqrt{2}}\left[\exp(ip_1x_1 + ip_2x_2) + \exp(ip_1x_2 + ip_2x_1)\right]. \tag{2.50}$$

The two-pion momentum distribution is then (Eq. (2.14))

$$\mathcal{P}_2(p_1,p_2) = \int dx_1dx_2\; S(x_1,p_1)S(x_2,p_2)\left|\Psi_{p_1,p_2}(x_1,x_2)\right|^2. \tag{2.51}$$

Thus, the two-pion correlation function is

$$\begin{aligned} C_2(p_1,p_2) &= \frac{\mathcal{P}_2(p_1,p_2)}{\mathcal{P}_1(p_1)\mathcal{P}_1(p_2)} = \frac{\int dx_1dx_2\; f(x_1)g(p_1)f(x_2)g(p_2)\left|\Psi_{p_1,p_2}(x_1,x_2)\right|^2}{\int dx_1\; f(x_1)g(p_1)\int dx_2 f(x_2)g(p_2)} \\ &= \int dx_1dx_2\; f(x_1)f(x_2)\left|\Psi_{p_1,p_2}(x_1,x_2)\right|^2. \end{aligned} \tag{2.52}$$

Noting that $\left|\Psi_{p_1,p_2}(x_1,x_2)\right|^2 = 1 + \frac{1}{2}\left[\exp(iq(x_1-x_2)) + \exp(-iq(x_1-x_2))\right]$, then

$$\begin{aligned} C_2(p_1,p_2) &= \int dx_1dx_2\; f(x_1)f(x_2)\left[1 + \frac{1}{2}\left(\exp(iq(x_1-x_2)) + \exp(-iq(x_1-x_2))\right)\right] \\ &= 1 + \frac{1}{2}\left[\int dx_1\; f(x_1)e^{iqx_1}\int dx_2\; f(x_2)e^{-iqx_2}\right. \\ &\quad \left. + \int dx_1\; f(x_1)e^{-iqx_1}\int dx_2\; f(x_2)e^{iqx_2}\right] \\ &= 1 + \tilde{f}(q)\tilde{f}^*(q) = 1 + \left|\tilde{f}(q)\right|^2, \end{aligned} \tag{2.53}$$

where $\tilde{f}(q) = \int dx\, \exp(iqx)f(x)$. Hence, the two-pion correlation function measures the squared norm of the Fourier transformed source coordinate-space distribution function of the pion emitting source, where the Fourier transformed source density is often called the characteristic function. Notice that the two-pion correlation function is insensitive to the phase of the characteristic function, and as a consequence it only measures the relative coordinates distributions of the source, but it cannot measure the location of the center of the source distribution [27].

If the characteristic function is an analytic function at $q = 0$ and can be expanded into a convergent Taylor series

$$\tilde{f}(q) \approx 1 + iq\langle x\rangle - q^2\langle x^2\rangle/2 + \ldots, \tag{2.54}$$

where

$$\langle x^n\rangle = \int dx\; x^n f(x), \tag{2.55}$$

then, the two-pion correlation function can be expressed as

$$C_2(q,K) = 1 + \left|\tilde{f}(q)\right|^2 \approx 2 - q^2(\langle x^2\rangle - \langle x\rangle^2) + \ldots \approx 1 + \exp\Big(-q^2R^2\Big), \tag{2.56}$$

where a Gaussian source radius parameter R is defined as the width of the source emission function $R = \sqrt{\langle x^2 \rangle - \langle x \rangle^2}$. To a first approximation, this ansatz can give a good description of the data. Therefore, it is possible to perform a fit to a Gaussian of a measured two-pion correlation function and obtain the source radius, which will be further discussed. However, we could wonder about the physical conditions under which this ansatz remains valid. To have a better understanding of it, the pion emission may be figured out as a superposition of many independent processes that shift by δx the coordinate x, and that the final production point, is a sum of many similarly distributed random shifts, $x = \sum_i \delta x_i$. If the shifts are characterized by a finite variance, then, by means of the Central Limit Theorem[2], for such random variables, the probability distribution for x tends to a Gaussian. Since the Fourier transform of a Gaussian is also a Gaussian, so it is expected that the shape of the two-pion correlation function is also a Gaussian [27].

Nonetheless, there are many random processes for additive random variables where a limiting distribution exists, but it is not a Gaussian. For example, in the vicinity of a critical point, where the phase transition changes from a first order to a second order, fluctuations appear on all possible wavelengths and scales. These fluctuations are signalled by a decreased attenuation length at all possible wavelengths. As the characteristic size disappears from the physical description of second-order phase transitions at the critical point, power-law distributions emerge and characterize the physical quantities and the exponents of these power laws [37]. Due to this power-law behaviour of the distributions, the variance of the elementary process diverges, and thus, there is a non-analytic behaviour for small values of the arguments, then the probability distribution will deviate from a Gaussian. This kind of distribution is called Lévy or stable distribution [27]. For a more complete discussion of Lévy distributions, see Ref. [27] and references therein. Following Ref. [27], let's write a generalized univariate stable distribution (the characteristic function) as

$$\tilde{f}(q) = \exp\left(-\gamma^{\alpha_{\text{Lévy}}}|q|^{\alpha_{\text{Lévy}}} + i\beta\gamma^{\alpha_{\text{Lévy}}}|q|^{\alpha_{\text{Lévy}}}\text{sign}(q)\tan\left(\frac{\alpha_{\text{Lévy}}\pi}{2}\right) + iq\delta\right), \tag{2.57}$$

where $\alpha_{\text{Lévy}} \neq 1$. Hence, this characteristic function depends on four parameters: the Lévy index of stability, $0 < \alpha_{\text{Lévy}} \leq 2$; the skewness parameter, $-1 \leq \beta \leq 1$; the scale parameter, $0 < \gamma$ and the location parameter, $-\infty < \delta < \infty$. Let's consider a special case of this general distribution, where $\beta = 0$, $\gamma = R/2^{1/\alpha_{\text{Lévy}}}$ and $\delta = x_0$, then

$$\tilde{f}(q) = \exp(iqx_0 + |qR|^{\alpha_{\text{Lévy}}}) \approx 1 + iqx_0 - \frac{1}{2}|qR|^{\alpha_{\text{Lévy}}}. \tag{2.58}$$

Notice that this expression is only analytical if $\alpha_{\text{Lévy}} = 2$, which corresponds to the Gaussian limit. Hence, the two-pion correlation function is

$$C_2(q; \alpha_{\text{Lévy}}) = 1 + \exp(-|qR|^{\alpha_{\text{Lévy}}}). \tag{2.59}$$

[2]In a few words, the Central Limit Theorem states that, under certain conditions, the distribution of the sum of a large number of random variables converges to a limit distribution. If the elementary distributions have finite mean and variance, then the limit distribution of their sum is a Gaussian.

The physical meaning of the index of stability is that the Lévy distribution decreases for large values of the coordinate x as a power-law, $f(x) \propto x^{-1-\alpha_{\text{Lévy}}}$ for $x \gg R$. These distributions are long-tailed and are related to the self-similarity of the generating mechanism. Particular cases of this expression correspond to $\alpha_{\text{Lévy}} = 2$, which is the already discussed Gaussian case, and $\alpha_{\text{Lévy}} = 1$, which is referred as the Cauchy form [27]. The three dimensional generalization of the previous discussion can be found in Ref. [27], but it is beyond the scope of this work.

As it has been said, in the vicinity of the critical point, where a second-order phase transition becomes a first-order phase transition, there is an emergence of critical behaviour, in which certain properties of the system diverge or go to zero. To keep track of these rapid variations in the system properties, critical exponents are introduced to describe their behaviour around the critical point. In particular, for the case of QCD matter described in Chapter 1, there exist six critical exponents [37, 38]:

- The critical exponent α [3], that measures the power-law behaviour of the heat capacity C near the critical point, is defined as

$$C(t) \simeq |t|^{-\alpha}, \tag{2.60}$$

  where t is the reduced temperature $t = (T - T_C)/T_C$

- The critical exponent β, which signals the temperature dependence near, but below, the critical point of the order parameter, $|\phi|$, (the quark condensate) is defined as

$$|\phi(t)| \simeq |t|^{\beta} \tag{2.61}$$

- The susceptibility exponent γ, defined as

$$\int d^3r\, G(r,t) \propto |t|^{-\gamma}, \tag{2.62}$$

  where r is a measure of the relative coordinates and $G(r,t) = \langle\phi(r,t)\phi(0,t)\rangle - \langle\phi(0,t)\rangle^2$ is the order parameter correlation function

- The exponent δ is related to the expectation value of the order parameter in the presence of a small external field that is related to the masses of the light quarks $H \propto m_q = m_u = m_d$, it is defined as

$$\langle\phi(t = 0, H \to 0)\rangle \propto |H|^{1/\delta} \tag{2.63}$$

- The exponent ν of the correlation length ζ, defined as

$$\zeta \propto |t|^{-\nu} \tag{2.64}$$

[3] Not to be confused with the Lévy index of stability, $\alpha_{\text{Lévy}}$.

- The exponent η of the Fourier transformed correlation function of the order parameter in the critical point, defined as

$$\tilde{G}(k \to 0) \propto |k|^{-2+\eta} \tag{2.65}$$

Only two of these six critical exponents are independent, while the remaining four are related by

$$\begin{aligned} \alpha &= 2 - d\,\nu, \\ \beta &= \frac{\nu}{2}\,(d - 2 + \eta)\,, \\ \gamma &= (2 - \eta)\,\nu, \\ \delta &= \frac{d + 2 - \eta}{d - 2 + \eta}, \end{aligned} \tag{2.66}$$

where d is the number of dimensions ($d = 3$ for heavy ions).

In a model of QCD where there are two species of massless quarks, based on the symmetries of the order parameter, Rajagopal and Wilczek [38] argued that to describe a second-order chiral phase transition, the order parameter should have an $O(4)$ symmetry group of rotations in internal space. Hence, the universality class of two flavour massless QCD should be the same of the 3d Ising model.

Since the universality class of QCD is predicted to be that of the 3d Ising model, it is possible to compute the values of the six critical exponents. Nevertheless, due to the violent conditions of heavy-ion collisions, the universality class is not the one of the 3d Ising model but rather that of the random field 3d Ising model [37]. The values of the critical exponents are [37, 39]

$$\begin{aligned} \eta &= 0.5 \pm 0.05, \\ \nu &= 1.1 \pm 0.2, \\ \alpha &= -1.3 \pm 0.6, \\ \beta &= 0.6 \pm 0.1, \\ \gamma &= 2.2 \pm 0.4, \\ \delta &= 4.7 \pm 0.3. \end{aligned} \tag{2.67}$$

On the other hand, recall that in the QGP, the vacuum expectation value of the quark condensate vanishes, while in the hadron gas phase it is non-zero. The correlation function of this order parameter is defined as [37]

$$\rho(r) = \langle \phi(r)\phi(0) \rangle - \langle \phi \rangle^2, \tag{2.68}$$

and measures the spatial correlations between pions. In the vicinity of the critical point, this correlation must decay as a power-law [37]

$$\rho(r) \propto r^{-(d-2+\eta)}. \tag{2.69}$$

For Lévy stable sources, the correlation between initial and actual positions must also decay as a power-law [37]

$$\rho(r) \propto r^{-(1+\alpha_{\text{Lévy}})}, \tag{2.70}$$

hence, for the case of QCD matter in $d = 3$, the correlation exponent is equal to the Lévy index of stability, i.e.,

$$\eta = \alpha_{\text{Lévy}}. \tag{2.71}$$

Therefore, the measurement of the two-pion correlation function not only gives us information about the size and shape of the pion emitting source, but it can also be used to signal the presence of critical phenomena in heavy-ion collisions [37, 40, 41].

CHAPTER 3

Monte Carlo simulations with UrQMD

This chapter presents a description of the Monte Carlo simulations used to perform the femtoscopy studies. Firstly, a concise description of the model utilized to generate phase-space distributions, from which the two-pion correlation function was computed, is presented.

3.1 The UrQMD approach to heavy-ion collisions

Numerical simulations of heavy-ion collisions provide an excellent tool for studying several aspects of these systems. As mentioned in the preceding chapter, a great variety of models has been developed, each providing us with a better description of some phenomena at a particular energetic regime. Several approaches exist to the modelling of relativistic collisions of heavy-ions, such as thermal models, hydrodynamic models and microscopic transport models [12]. Within this last category, one of the most widely used models at low (within the range of SIS, 2.7-10 GeV, and the range of RHIC, up to 100 GeV) and high energies (within the range of LHC, 2.76 - 5.02 TeV) is the Ultra-relativistic Quantum Molecular Dynamics (UrQMD) model [42–44], which describes the evolution of the hadronic degrees of freedom produced during the whole evolution of the collision. UrQMD is a multi-purpose tool that aims to describe the collision by propagating the particles along straight-line classical trajectories until there is an interaction at some point on a one-to-one basis. This simulation mode is sometimes referred to as cascade model [11]. In other words, UrQMD describes the collision by effectively solving, with Monte Carlo techniques, the

Boltzmann equation [12]

$$\frac{\mathrm{d}f_i(x,p)}{\mathrm{d}t} \equiv \frac{\partial p}{\partial t}\frac{\partial f_i(x,p)}{\partial p} + \frac{\partial x}{\partial t}\frac{\partial f_i(x,p)}{\partial x} + \frac{\partial f_i(x,p)}{\partial t} = S_t f_i(x,p), \tag{3.1}$$

where f_i is the phase space density of the particle species $i = N,\ \Delta,\ \Lambda$, etc., x and p are the position and momentum of the particle, respectively, and $S_t f_i$ is the collision term of this particle species, which is connected to any other particle species phase space density f_k [12].

In UrQMD, only binary collisions are considered, and for two particles to interact, the following condition must be satisfied: the area of the circumference whose diameter is the transverse distance of the closest approach between them, d_{trans}, must be smaller than the total cross-section for interaction between the two, σ_{tot}, [12]

$$d_{\mathrm{trans}} < \sqrt{\frac{\sigma_{\mathrm{tot}}}{\pi}}, \tag{3.2}$$

with the interactions described as probabilities, weighted by their branching ratios. In the low energy regime (< 5 GeV), particle production is dominated by resonance decays, while at higher energies, elastic scatterings, soft resonance production, string fragmentation, and string excitation (Lund model) becomes more relevant [12, 45].

The UrQMD model considers around 50 baryon and 45 meson species, together with their respective antiparticle, and all the possible reactions between them: nucleon–nucleon, meson–meson, meson–baryon and baryon–baryon [12].

UrQMD works as a `Fortran77` and `GNU-make` code, which is compiled with an input file that indicates the collision parameters (number of nucleons involved, center of mass energy, impact parameter, and final evolution time), the particular model that will be used and the expected output format. There are six possible output formats, each one containing different information, such as the particle identity, its freeze-out phase-space coordinates and the phase-space coordinates at some specific time or / and at the end of the simulation, as well as the process that produced it and the parent particle. To see the list of all the different particles that are included in UrQMD, just as the different process that can produce particles, see Ref. [44].

3.2 Simulation of Bi+Bi collisions

To perform the femtoscopy studies, five million central collisions of the bismuth isotopes $^{209}_{83}$Bi were simulated using UrQMD in its cascade mode at four different center-of-mass collision energies: $\sqrt{s_{NN}} = 4.0,\ 5.8,\ 7.7$ and 9.2 GeV, with the impact parameter chosen to be a random number between 0 and 1 fm, this impact parameter was chosen to avoid any effect related to the angular momentum generated in non-central collisions. The simulations were stopped after an evolution time of 200 fm. These energies were chosen to be within

the NICA energy range. Including the first experimental run of the NICA collider: Bi+Bi at $\sqrt{s_{NN}} = 9.2$ GeV.

The CRAB formalism requires the input files which contain the phase space points to be in the `OSCAR1997A` format [30], which includes a file-header consisting of [44]

1. Output format: `OSC1997A`
2. File contents: `final_id_p_x`
3. General information, which contains the model and its version, projectile and target nuclei, reference frame, incident beam energy, and number of test particles per nucleon, for example:

```
UrQMD  3.4       (209,    83)+(209,    83)  eqsp  0.4324E+02          1
```

The main file body consists of a one-line event header, which contains [44]:

1. Event counter.
2. Number of particles in the event.
3. Impact parameter in fm.
4. Rotation of the plane, which is fixed to zero in UrQMD.

And the subsequent particle vectors, in which time units are $[t] = 1$ fm, position units are $[r] = 1$ fm, energy (and hence momenta) units are $[E] = 1$ GeV and mass units are $[m] = 1$ GeV [44]:

1. Particle counter.
2. PDG particle identification number[1].
3. Particle's momentum component along the x direction.
4. Particle's momentum component along the y direction.
5. Particle's momentum component along the z direction.
6. Particle's energy.
7. Particle's mass.
8. Particle's freeze-out position component along the x direction.

[1] See the Particle Data Group website https://pdg.lbl.gov/2023/listings/contents_listings.html for more information on the particle ID.

```
OSC1997A
final_id_p_x
   UrQMD  3.4       (209,    83)+(209,    83)  egsp  0.4324E+02        1
         1        1928     0.654     0.000
         1        2212  0.768516E-01  -.889905E-01  0.523122E+01  0.531595E+01  0.938000E+00  0.260631E+01  -.535103E+01  0.247522E+02  0.271180E+02
         2        2212  -.119187E+00  -.900905E-01  0.441408E+01  0.451091E+01  0.917574E+00  0.000000E+00  0.000000E+00  0.000000E+00  0.000000E+00
         3        2212  -.544653E+00  0.124143E+01  -.164424E+01  0.232834E+01  0.938000E+00  -.892984E+01  0.150474E+02  -.254880E+02  0.362900E+02
         4        2112  -.245898E+00  -.379727E+00  -.109825E-01  0.104145E+01  0.938000E+00  -.504972E+01  -.951113E+00  -.891433E+00  0.135821E+02
         5        2112  0.631594E-01  0.215271E+00  -.246538E+01  0.264732E+01  0.938000E+00  -.137009E+01  0.520523E+01  -.439930E+02  0.521220E+02
         6        2212  -.274031E+00  0.476537E-01  0.831804E+00  0.128418E+01  0.938000E+00  -.109123E+02  -.137439E-01  0.146258E+02  0.290088E+02
         7        2112  -.396144E+00  0.160850E+01  0.309997E+01  0.363783E+01  0.938000E+00  -.191413E+01  0.783603E+01  0.109139E+02  0.156085E+02
         8        2112  0.541221E+00  -.561191E+00  -.104050E+01  0.160323E+01  0.938000E+00  0.941632E+01  -.785605E+01  -.474319E+01  0.191723E+02
         9        2212  0.169214E+00  -.278197E+00  0.340674E+01  0.354849E+01  0.938000E+00  0.363836E+01  0.149934E+00  0.322924E+02  0.349788E+02
        10        3222  -.202897E+00  0.429722E+00  0.282927E+01  0.310668E+01  0.119200E+01  -.116202E+01  -.966259E+00  0.294376E+02  0.343509E+02
        11        2212  0.197950E-01  0.254417E+00  0.540149E+01  0.548826E+01  0.938000E+00  0.247221E+01  0.613453E+01  0.425827E+02  0.442448E+02
        12        2112  -.212746E+00  0.218267E+00  0.381765E+00  0.105759E+01  0.938000E+00  -.677962E+00  0.287356E+00  -.154411E+01  0.125691E+02
        13        2212  -.634747E+00  0.341518E+00  0.180600E+01  0.215894E+01  0.938000E+00  -.526612E+01  0.142470E+01  0.129780E+02  0.185729E+02
        14        2212  -.247465E+00  -.375701E+00  -.319052E+01  0.335584E+01  0.938000E+00  -.482294E+01  -.111108E+02  -.493852E+02  0.539247E+02
        15        2112  -.961211E+00  0.143564E+00  0.147802E+01  0.200223E+01  0.938000E+00  -.200760E+01  0.718489E+01  0.114807E+02  0.184360E+02
```

Figure 3.1: Example of the OSCAR1997A format.

9. Particle's freeze-out position component along the y direction.

10. Particle's freeze-out position component along the z direction.

11. Particle's freeze-out time.

An example of the `OSCAR1997A` format can be seen in Fig. 3.1. UrQMD supports this output file format on its output type `.f19`.

As it has been stated in the preceding chapters, since charged pions are the most abundantly detected particles in heavy-ion collisions, they are the most commonly used femtoscopy tool. Thus, we are going to focus on positively charged pions.

In the study of heavy-ion collisions, Monte Carlo simulations provide an equivalent tool to obtain experimentally measurable quantities. Since not all of the quantities of interest can be experimentally measured, they must be found from the handful of experimentally measurable quantities [46], such as the multiplicity, the total and the transverse momentum distribution, among others. Recall, from what was discussed in Chapter 2, that the two-pion correlation function can be obtained from the total and transverse momentum distributions of pairs of particles.

In Fig. 3.2, the positively charged pion multiplicity is shown for the four center-of-mass energies that were studied. As it is expected, the average multiplicity grows as the energy increases. Whereas in Fig. 3.3, their transverse momentum distributions are shown, which shows an exponential decay, as expected.

3.3 Separation of primary and secondary pions

Since we are interested in taking into account the *core-halo* picture, discussed in Chapter 2, we must separate the particles coming from the *core*, which from now on will be referred to as primary pions, and those coming from the *halo*, which will be referred to as secondary pions. Recall that, in simulations of relativistic heavy-ion collisions, the primary and secondary language is typically used for particles that come from primary processes and from the decay of long-lived resonances, respectively. To accomplish this, we must make

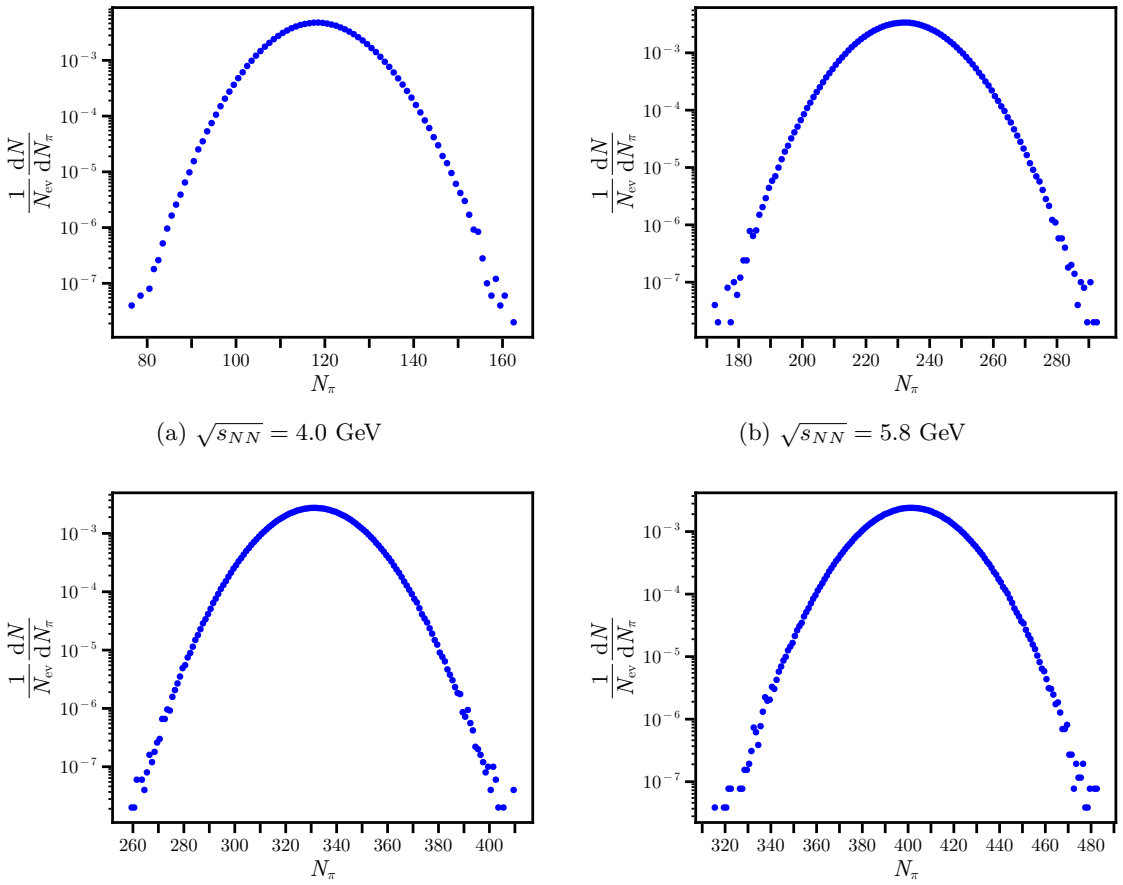

(a) $\sqrt{s_{NN}} = 4.0$ GeV

(b) $\sqrt{s_{NN}} = 5.8$ GeV

(c) $\sqrt{s_{NN}} = 7.7$ GeV

(d) $\sqrt{s_{NN}} = 9.2$ GeV

Figure 3.2: Positively charged pion multiplicity, normalized to the total number of events, at (a) $\sqrt{s_{NN}} = 4.0$ GeV, (b) $\sqrt{s_{NN}} = 5.8$ GeV, (c) $\sqrt{s_{NN}} = 7.7$ GeV and (d) $\sqrt{s_{NN}} = 9.2$ GeV, for events with impact parameters between $0 - 1$ fm.

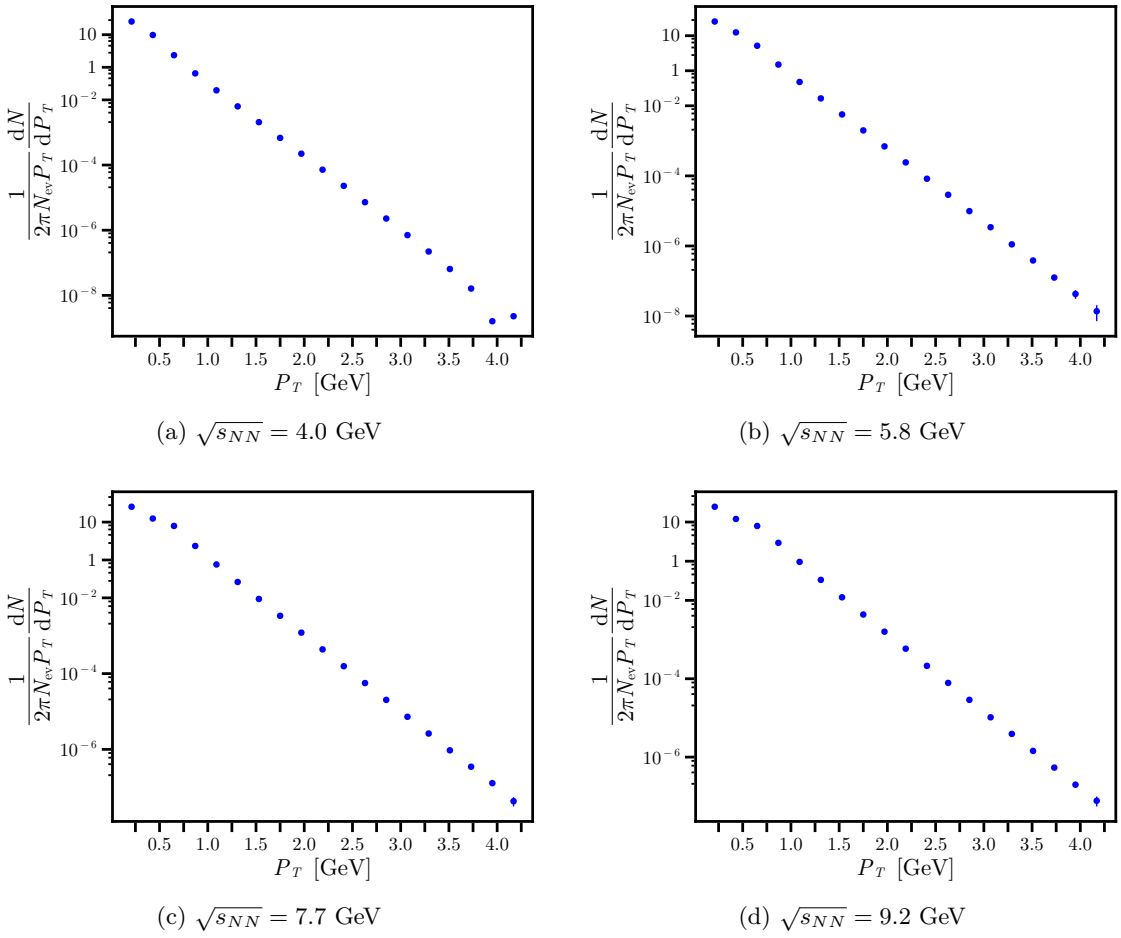

(a) $\sqrt{s_{NN}} = 4.0$ GeV

(b) $\sqrt{s_{NN}} = 5.8$ GeV

(c) $\sqrt{s_{NN}} = 7.7$ GeV

(d) $\sqrt{s_{NN}} = 9.2$ GeV

Figure 3.3: Transverse momentum distribution of positively charged pion, normalized to the total number of events and integrated over the rapidity interval, at (a) $\sqrt{s_{NN}} = 4.0$ GeV, (b) $\sqrt{s_{NN}} = 5.8$ GeV, (c) $\sqrt{s_{NN}} = 7.7$ GeV and (d) $\sqrt{s_{NN}} = 9.2$ GeV, for events with impact parameters between $0 - 1$ fm.

use of the parent process type information, which is provided in the UrQMD output file type `.f13`. This output file includes a detailed event header per event [44]:

1. Model, version, and output file type.
2. Projectile and target nuclei.
3. Transformation velocity between the center-of-mass reference frame, the laboratory and the projectile frame.
4. Impact parameter and total cross-section information.
5. Equation of state and collision energy in the laboratory, center-of-mass and projectile reference frames.
6. Event number, random seed, simulation total time and elapsed time between the start and end of the simulation.
7. Information about the simulation options (these lines start with the characters `op`).
8. Information about the optional parameters used in the simulation (these lines start with the characters `pa`).
9. A description of the particle vector will be listed below (this line starts with the characters `pvec`).

The event header is followed by a line that contains the number of particles and the simulation output time. The next line is the collision counter line, which contains:

1. Number of collisions.
2. Number of elastic collisions.
3. Number of inelastic collisions.
4. Number of Pauli-blocked collisions.
5. Number of decays.
6. Number of produced *hard* baryon resonances.
7. Number of produced *soft* baryon resonances.
8. Number of baryon resonances produced via the decay of another resonances.

After the collision counter line, the final particle's phase space information is contained within the aforementioned particle vector, which includes [44]:

1. Particle's time.
2. Particle's position component along the x direction.
3. Particle's position component along the y direction.
4. Particle's position component along the z direction.
5. Particle's energy.
6. Particle's momentum component along the x direction.
7. Particle's momentum component along the y direction.
8. Particle's momentum component along the z direction.
9. Particle's mass.
10. Particle urqmd type.
11. Two times the particle's isospin.
12. Particle's charge.
13. Parent collision number.
14. Number of collisions.
15. Parent process type.
16. Particle's freeze-out time.
17. Particle's freeze-out position component along the x direction.
18. Particle's freeze-out position component along the y direction.
19. Particle's freeze-out position component along the z direction.
20. Particle's freeze-out energy.
21. Particle's freeze-out momentum component along the x direction.
22. Particle's freeze-out momentum component along the y direction.
23. Particle's freeze-out momentum component along the z direction.

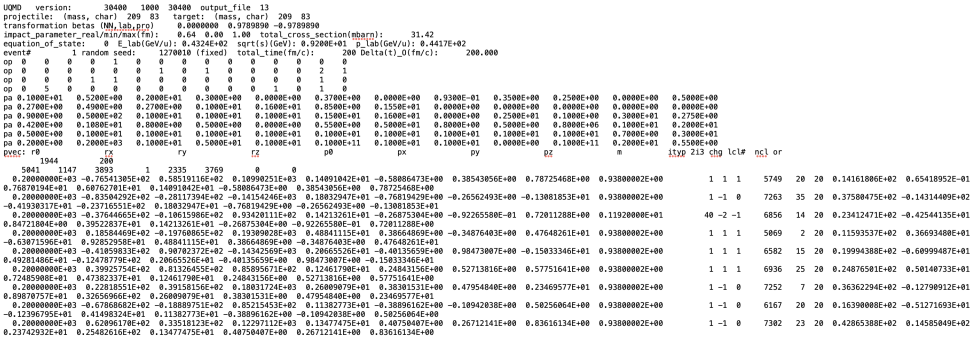

Figure 3.4: Example of the .f13 format.

The units in the particle momentum follow the same conventions as in the particle vector the `OSCAR1997A` format. An example of the `.f13` format can be seen in Fig. 3.4.

Therefore, by identifying the particles whose parent process is a decay, it is possible to separate the pions coming from the *halo* than those coming from the *core* and rewrite the information given in the `.f13` file to the `OSCAR1997A` format and pass it to CRAB in order to obtain the two-pion correlation function.

The secondary pions, whose origin is the decay of resonances, come mainly from the decay of the ρ, Δ, ω, and K^* resonances, whose mean lifetimes are $\tau_\rho = 1.64$ fm, $\tau_\Delta = 1.21$ fm, $\tau_\omega = 23.4$ fm and $\tau_{K^*} = 3.94$ fm, respectively. These "parent" resonances are consistent with the long-lived resonances discussed in Ref. [23].

In Figs. 3.5 and 3.6, the positively charged primary and secondary pion multiplicity are shown for the four center-of-mass energies that were studied, respectively. This multiplicities are normalized over the total number of events. Once again, as it is expected, the average multiplicity grows as the energy increases for both kinds. Figures 3.7 and 3.8 show the transverse momentum distributions of primary and secondary pions, respectively. Again, these distributions show an exponential decay, as expected.

Notice that the primary pion average multiplicity (between 10 and 50 primary pions per event) is significantly smaller than for the secondary pions (between 110 and 350 secondary pions per event). This means that most of the pions are produced by decays of resonances and not by primary processes. Figure 3.9 shows the distribution of the event-by-event fraction, f_{Primary}, of primary to all pions. The mean fraction of primary pions is

$$f_{\text{Primary}}(\sqrt{s_{NN}} = 4.0 \text{ GeV}) = 0.061987, \tag{3.3}$$
$$f_{\text{Primary}}(\sqrt{s_{NN}} = 5.8 \text{ GeV}) = 0.108306, \tag{3.4}$$
$$f_{\text{Primary}}(\sqrt{s_{NN}} = 7.7 \text{ GeV}) = 0.123475, \tag{3.5}$$
$$f_{\text{Primary}}(\sqrt{s_{NN}} = 9.2 \text{ GeV}) = 0.129207, \tag{3.6}$$

which means that between 6 and 13 % of the produced pions are of primary origin, and this event-by-event fraction increases with the collision energy.

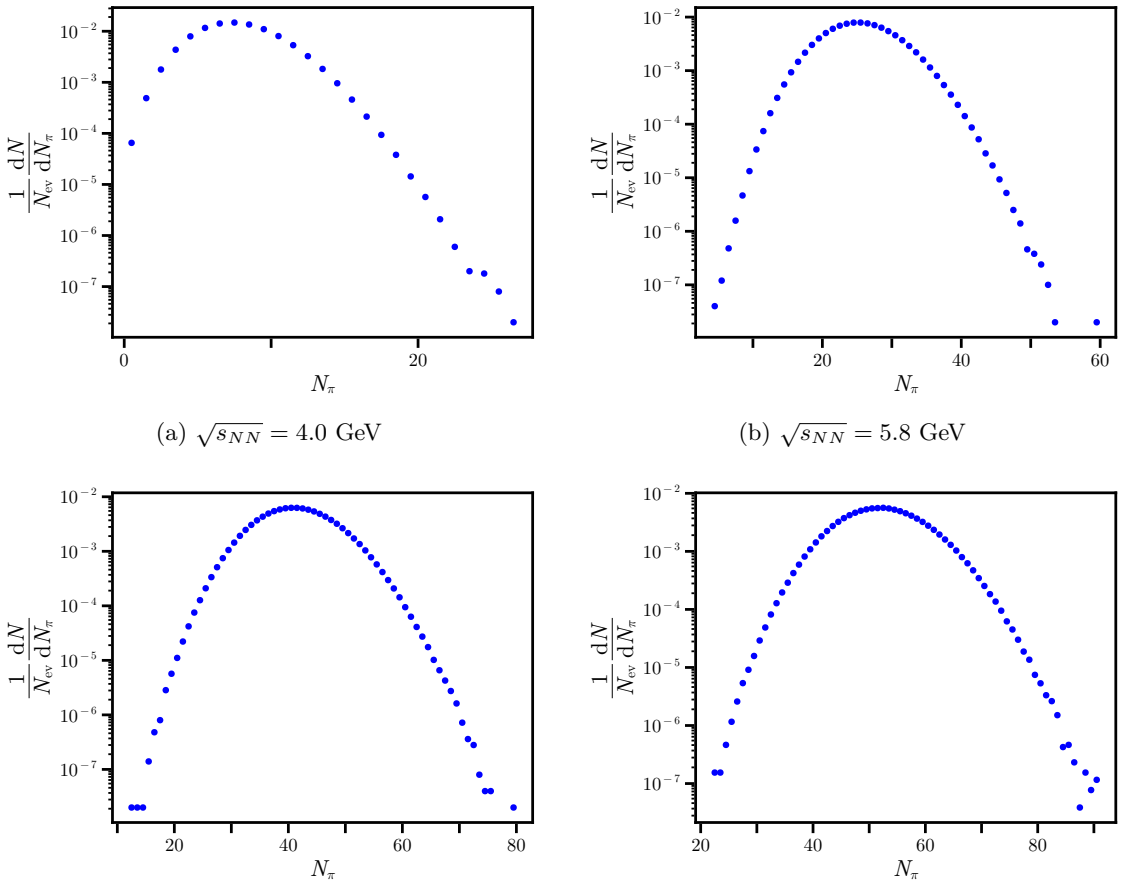

(a) $\sqrt{s_{NN}} = 4.0$ GeV

(b) $\sqrt{s_{NN}} = 5.8$ GeV

(c) $\sqrt{s_{NN}} = 7.7$ GeV

(d) $\sqrt{s_{NN}} = 9.2$ GeV

Figure 3.5: Multiplicity of positively charged primary pions, normalized to the total number of events, at (a) $\sqrt{s_{NN}} = 4.0$ GeV, (b) $\sqrt{s_{NN}} = 5.8$ GeV, (c) $\sqrt{s_{NN}} = 7.7$ GeV and (d) $\sqrt{s_{NN}} = 9.2$ GeV, for events with impact parameters between $0 - 1$ fm.

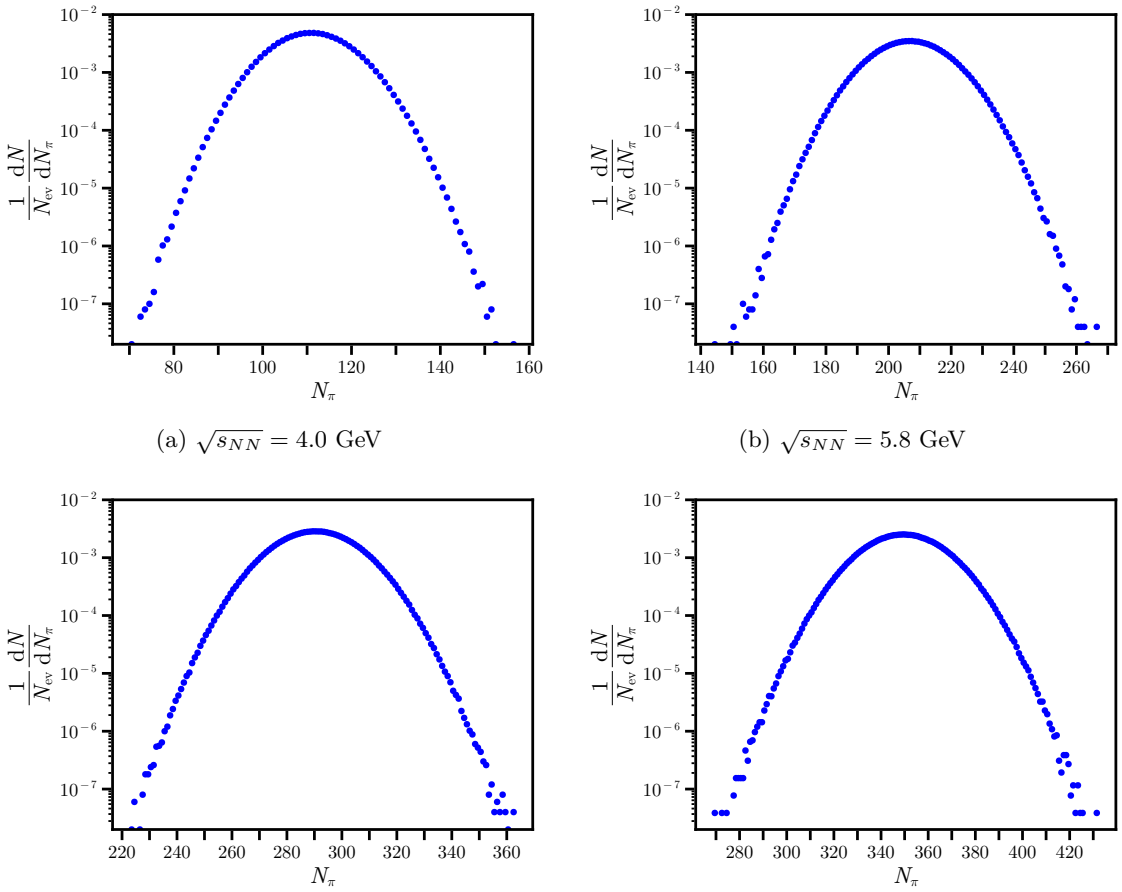

(a) $\sqrt{s_{NN}} = 4.0$ GeV

(b) $\sqrt{s_{NN}} = 5.8$ GeV

(c) $\sqrt{s_{NN}} = 7.7$ GeV

(d) $\sqrt{s_{NN}} = 9.2$ GeV

Figure 3.6: Multiplicity of positively charged secondary pions, normalized to the total number of events, at (a) $\sqrt{s_{NN}} = 4.0$ GeV, (b) $\sqrt{s_{NN}} = 5.8$ GeV, (c) $\sqrt{s_{NN}} = 7.7$ GeV and (d) $\sqrt{s_{NN}} = 9.2$ GeV, for events with impact parameters between $0 - 1$ fm.

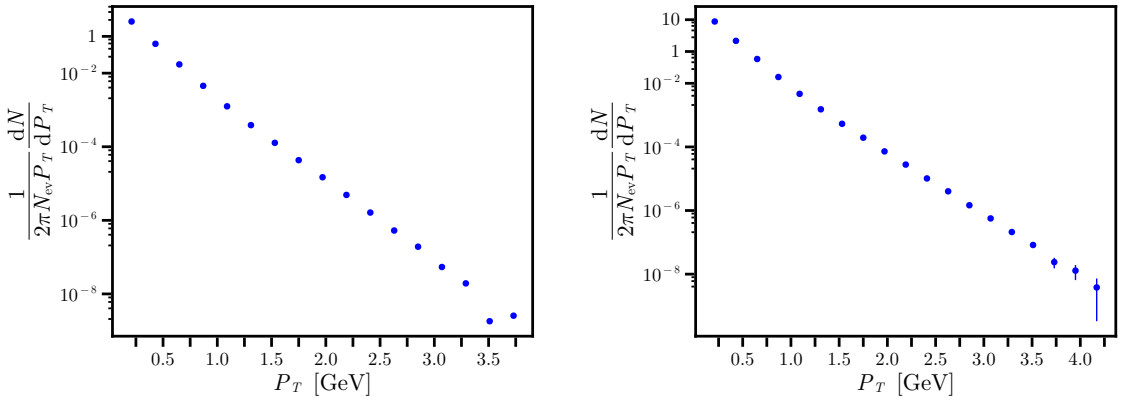

(a) $\sqrt{s_{NN}} = 4.0$ GeV

(b) $\sqrt{s_{NN}} = 5.8$ GeV

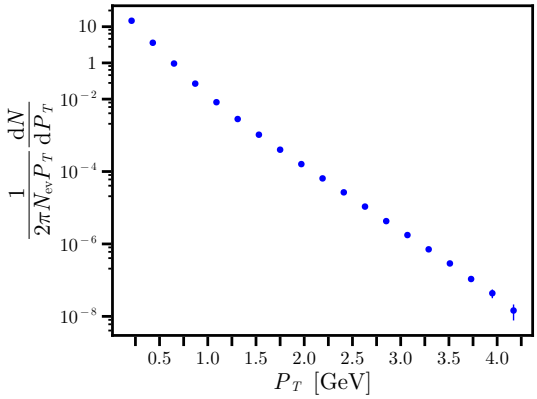

(c) $\sqrt{s_{NN}} = 7.7$ GeV

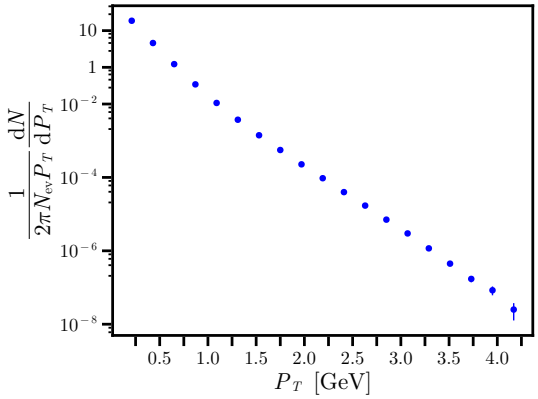

(d) $\sqrt{s_{NN}} = 9.2$ GeV

Figure 3.7: Transverse momentum distribution of positively charged primary pions, normalized to the total number of events and integrated over the rapidity interval, at (a) $\sqrt{s_{NN}} = 4.0$ GeV, (b) $\sqrt{s_{NN}} = 5.8$ GeV, (c) $\sqrt{s_{NN}} = 7.7$ GeV and (d) $\sqrt{s_{NN}} = 9.2$ GeV, for events with impact parameters between $0 - 1$ fm.

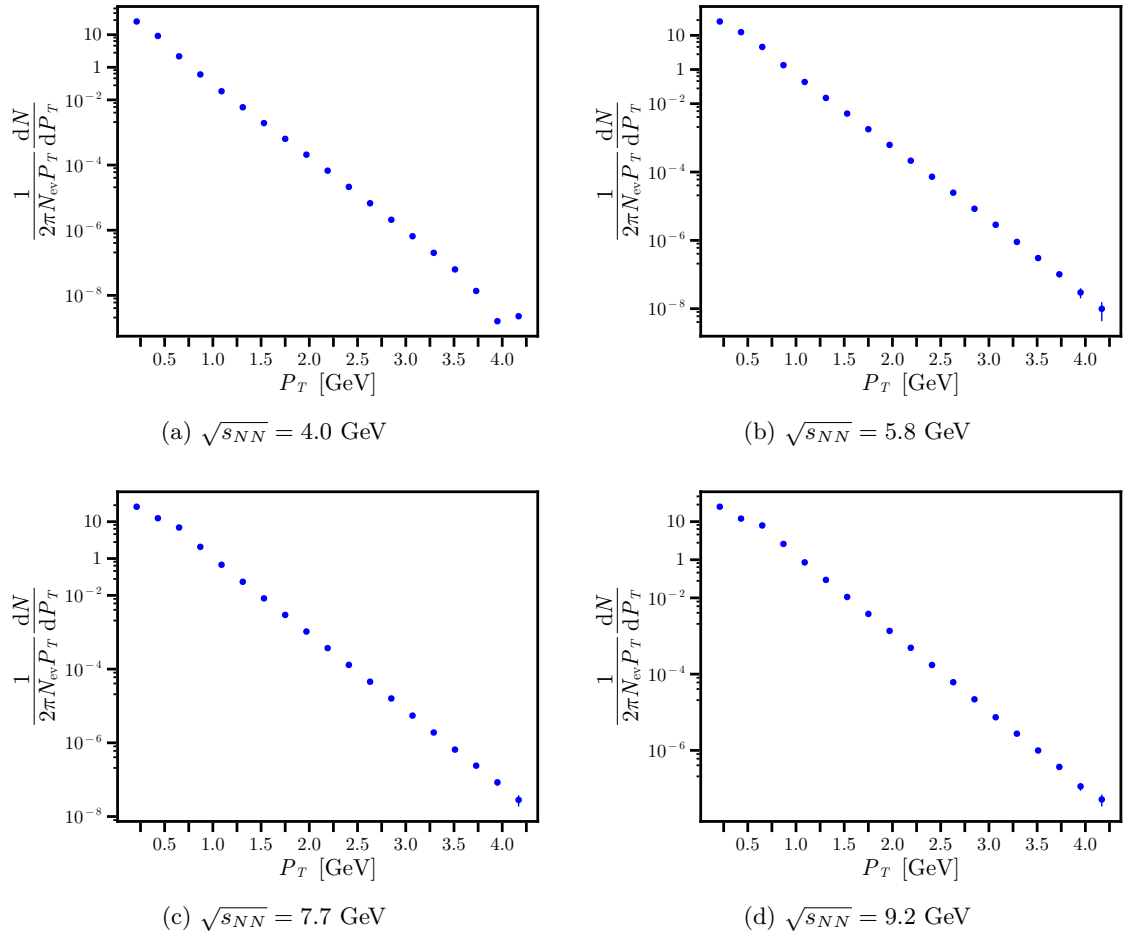

(a) $\sqrt{s_{NN}} = 4.0$ GeV (b) $\sqrt{s_{NN}} = 5.8$ GeV

(c) $\sqrt{s_{NN}} = 7.7$ GeV (d) $\sqrt{s_{NN}} = 9.2$ GeV

Figure 3.8: Transverse momentum distribution of positively charged secondary pions, normalized to the total number of events and integrated over the rapidity interval, at (a) $\sqrt{s_{NN}} = 4.0$ GeV, (b) $\sqrt{s_{NN}} = 5.8$ GeV, (c) $\sqrt{s_{NN}} = 7.7$ GeV and (d) $\sqrt{s_{NN}} = 9.2$ GeV, for events with impact parameters between $0 - 1$ fm.

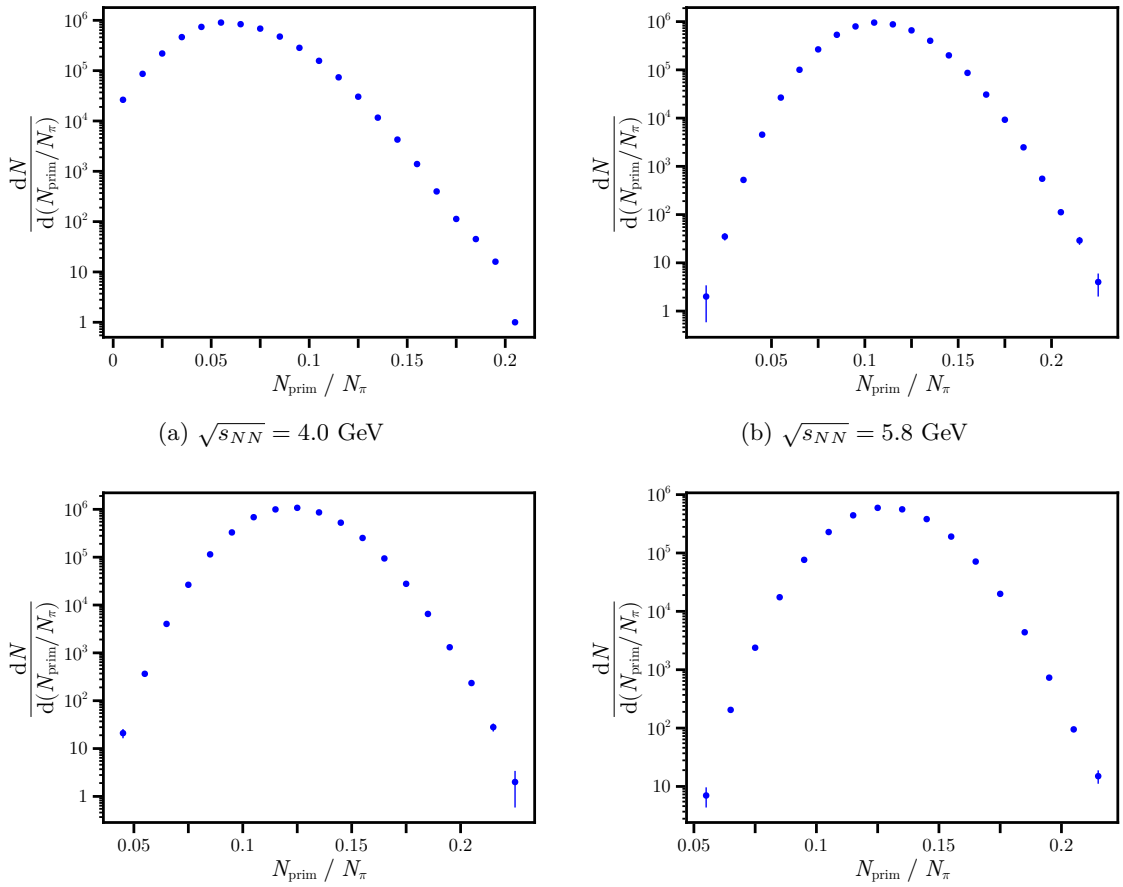

(a) $\sqrt{s_{NN}} = 4.0$ GeV

(b) $\sqrt{s_{NN}} = 5.8$ GeV

(c) $\sqrt{s_{NN}} = 7.7$ GeV

(d) $\sqrt{s_{NN}} = 9.2$ GeV

Figure 3.9: Distribution of the event-by-event fraction of primary to all positively charged pions at (a) $\sqrt{s_{NN}} = 4.0$ GeV, (b) $\sqrt{s_{NN}} = 5.8$ GeV, (c) $\sqrt{s_{NN}} = 7.7$ GeV and (d) $\sqrt{s_{NN}} = 9.2$ GeV, for events with impact parameters between $0 - 1$ fm.

CHAPTER 4

Results of the source size and parameters from two-pion correlation function

The main results of this work are presented in this chapter: using the Monte Carlo simulations of five million Bi+Bi collisions, the two-pion correlation function was computed using the CRAB formalism for the whole set of positively charged pions and for the separated sets of primary and secondary pions. By using the Gaussian, Lévy, and Lorentz forms of the two-pion correlation function, the source size, and parameters were obtained within the context of the *core-halo* picture.

4.1 Correlation function fits and parameters

Let us start by briefly summarizing the functional forms that the two-pion correlation function can take, as discussed in Chapter 2. As it has been mentioned, in general, it is assumed that the phase space source distribution, S, can be factorized into a space-time distribution and momentum distribution. The Fourier transform of the space-time part is assumed to be an analytic function around zero relative momentum and its second order Taylor expansion characterizes its behaviour, even for large values of $q_{\rm inv}$ [27]. Thus, the two-pion correlation function can be approximately written as

$$C_2(q_{\rm inv}) = 1 + \lambda \exp\Big(-q_{\rm inv}^2 R_{\rm inv}^2\Big), \tag{4.1}$$

where R_{inv} is the characteristic size of the source and $q_{\text{inv}} = \sqrt{q_0^2 - |\mathbf{q}|^2}$ is the invariant relative momentum. Eq. (4.1) will be referred to as the Gaussian form. The previously mentioned assumptions can be translated into the stochastic nature of the several (independent) pion emission processes. If one assumes that many independent processes shift the emission position and that the final production point is a sum of many, similarly distributed, random shifts whose variance is finite, then according to the Central Limit Theorem, the distribution tends to a Gaussian. However, suppose the processes are characterized by large fluctuations originating power-like tails and a non-analytic behaviour of the characteristic function. In that case, the limiting distribution is not a Gaussian but instead a Lévy distribution [27]. A special case of this distribution is the one named *symmetric stable* Lévy distribution, which is written as

$$C_2(q_{\text{inv}}) = 1 + \lambda \exp(-|q_{\text{inv}} R_{\text{inv}}|^{\alpha}), \tag{4.2}$$

where α is called the stability index and can be related to the correlation critical exponent of QCD [37, 47]. Equation (4.2) will be referred to as the Lévy form of the correlation function. As a last example of the different functions that can describe the two-pion correlation function, we consider the Lorentzian distribution

$$C_2(q_{\text{inv}}) = 1 + \lambda \frac{\Gamma^2}{q_{\text{inv}}^2 + \Gamma^2}, \tag{4.3}$$

where Γ is the width of the distribution and is related to the characteristic size of the source by $\Gamma = \frac{1}{2R_{\text{inv}}}$. Equation (4.3) will be referred to as the Lorentzian form of the correlation function. At this point, a clarification should be made: in the literature, the Cauchy form discussed in Chapter 2 is sometimes also called the Lorentzian form, since it can be deducted from a Lorentzian characteristic function. However, the form of the correlation function is different from the Lorentzian form of Eq. (4.3).

4.2 Two-pion correlation function with ideal resolution

In the context of the *core-halo* picture, the two-pion correlation function is distorted due to the effects of the finite resolution of the detectors and the multi-component source, hence, to explore the nature of these effects, we start by computing the two-pion correlation function for all the positively charged pions, obtained from the five million Bi+Bi collisions, and fitting the three previously discussed functional forms. We compute the correlation function for separating the primary and secondary pions of those five million Bi+Bi collisions, and fit them to the same forms to compare the results. The fits are done to the central value of the correlation function in each bin. The rationale is to simulate the case of a huge statistical sample. To avoid repetition, only one of the four collision energies studied will be fully presented in this chapter and the evolution of the source parameters as a function of the collision energy, obtained through the fits, will be shown. However, the complete data of the four collision energies will be presented in Appendix A, for the interested reader.

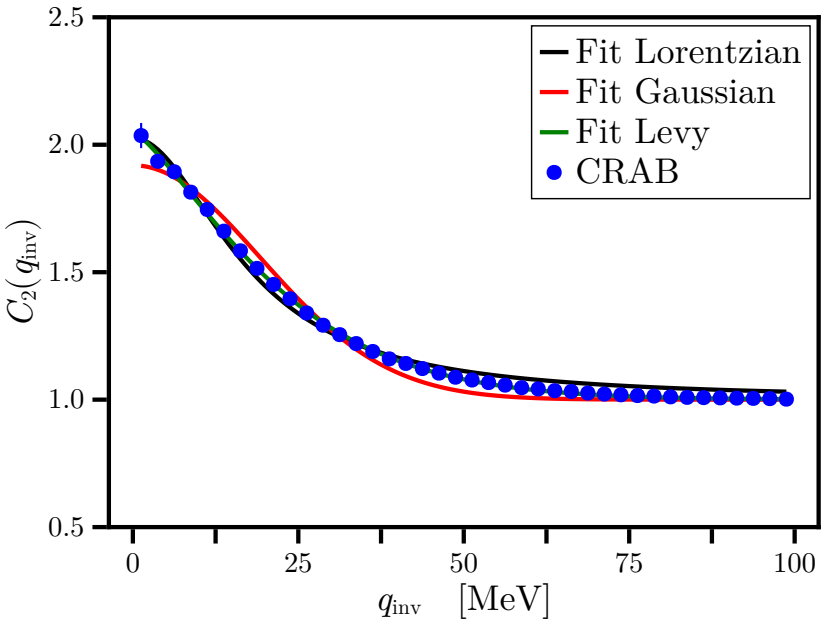

Figure 4.1: Two-pion correlation function for Bi+Bi collisions at $\sqrt{s_{NN}} = 5.8$ GeV, with impact parameter $b = 0 - 1$ fm. The blue dots represent the output of CRAB, while the solid lines of different colors represent the Lorentzian (black), Gaussian (red) and Lévy (green) fits.

Afterwards, the effect of the finite resolution will be taken into account and, the analysis above will be redone with this new dataset. Once again, to avoid repetition, only one of the four collision energies studied will be fully presented, and the evolution of the fit parameters will be shown. Nonetheless, the complete data of the four collision energies will be presented in Appendix B for the interested reader.

4.2.1 Two-pion correlation function for the complete set of pions

With the simulated Bi+Bi collisions, the CRAB formalism was applied to the phase space points. For the case of $\sqrt{s_{NN}} = 5.8$ GeV, the two-pion correlation function for the complete set of pions is shown in Fig. 4.1, together with its fits to the Lorentzian, Eq. (4.3), Gaussian, Eq. (4.1), and Lévy, Eq. (4.2), forms. The fit parameters are shown in Table 4.1. Notice that the fit that better describes the correlation function, by visual inspection and by the χ^2-value [1], is obtained with the Lévy form.

[1] In this case, the χ^2-value is defined as $\chi^2 = \sum_i \frac{(x_{\text{fit}} - x_{\text{data}})^2}{\sigma_{fit}}$, where x_{fit} is the value predicted by the fit, x_{data} is the value obtained from CRAB and σ_{fit} is the error associated with the fit.

	R_{inv} [fm]	λ	α	χ^2 / n.d.f.
Lorentzian	5.632 ± 0.142	1.027 ± 0.018	—	45.27
Gaussian	7.254 ± 0.166	0.919 ± 0.018	—	38.301
Lévy	8.121 ± 0.059	1.05 ± 0.006	1.312 ± 0.015	0.835

Table 4.1: Parameters resulting from fits of the two-pion correlation function to Lorentzian, Gaussian and Lévy forms for the complete pion set obtained at $\sqrt{s_{NN}} = 5.8$ GeV.

The same analysis can be done for the rest of the simulated collision energies (see Appendix A) and then obtain the fit that better describes the correlation function, which in all cases, it turns out to be the Lévy form. This is shown in Fig. 4.2.

Notice that for the whole sample of pions, there is a general tendency for R_{inv} to increase as the collision energy increases. The index α slightly decreases with the collision energy from the lowest to the largest energy considered but the overall decrease is non-monotonic.

As can be seen from Fig. 4.2, there appears to be a correlation between the fit parameters R_{inv}, λ and α. This was found in Ref. [17], and based on the findings of Ref. [48], a new scale parameter was introduced, without any theoretical motivation, that relates the other three by

$$\hat{R} \equiv \frac{R}{\lambda(1+\alpha)}. \tag{4.4}$$

Figure 4.3 shows the behaviour of $\hat{R}$ as a function of the collision energy for the complete set of pions. It can be seen that this parameter grows monotonically with the collision energy.

4.2.2 Two-pion correlation function for the separated samples

With the simulated Bi+Bi collisions and the separation of primary and secondary pions, discussed in Chapter 3, the CRAB formalism was applied to the phase space points of primary and secondary pions. For the case of $\sqrt{s_{NN}} = 5.8$ GeV, the two-pion correlation function for primary and secondary pions is shown in Fig. 4.4, together with its fits to the already discussed forms. Tables 4.2 and 4.3 show the resulting fit parameters for primary and secondary pions, respectively. Figure 4.4 also shows the comparison between the obtained correlation function for primary and secondary pions.

The results of the fits are consistent with the core-halo picture since the source of primary pions has a size of $R_{\text{inv, prim}} = 3.516$ fm, which is significantly smaller than that of secondary pions, $R_{\text{inv, second}} = 8.402$ fm. Notice that the following hierarchies of the source parameters hold: $R_{\text{inv, prim}} < R_{\text{inv, all}} < R_{\text{inv, second}}$, $\lambda_{\text{prim}} < \lambda_{\text{all}} < \lambda_{\text{second}}$ and $\alpha_{\text{second}} \lesssim \alpha_{\text{all}} < \alpha_{\text{prim}}$. Also, the correlation function for primary pions has the closest behaviour to a Gaussian.

Once again, using a visual inspection and the χ^2-value, the fit that better describes

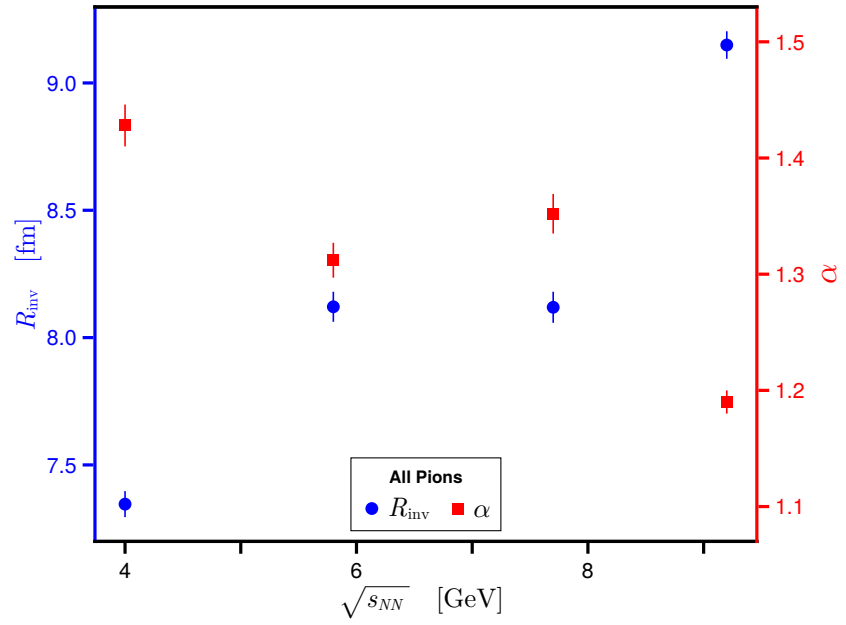

Figure 4.2: Source size $R_{\rm inv}$ (blue dots) and Lévy index of stability α (red squares) as a function of the collision energy, $\sqrt{s_{NN}}$, for the complete sets of pions obtained from Bi+Bi collisions with impact parameter $b = 0 - 1$ fm. $R_{\rm inv}$ and α are obtained from fits to a Lévy form.

	$R_{\rm inv}$ [fm]	λ	α	χ^2 / n.d.f.
Lorentzian	2.445 ± 0.079	1.03 ± 0.022	—	158.468
Gaussian	3.476 ± 0.017	0.965 ± 0.004	—	3.132
Lévy	3.516 ± 0.014	0.982 ± 0.004	1.863 ± 0.021	0.353

Table 4.2: Parameters resulting from fits of the two-pion correlation function to Lorentzian, Gaussian and Lévy forms for the primary pion set obtained at $\sqrt{s_{NN}} = 5.8$ GeV.

	$R_{\rm inv}$ [fm]	λ	α	χ^2 / n.d.f.
Lorentzian	5.828 ± 0.168	1.041 ± 0.021	—	54.205
Gaussian	7.455 ± 0.17	0.93 ± 0.018	—	30.012
Lévy	8.402 ± 0.065	1.066 ± 0.007	1.31 ± 0.016	0.321

Table 4.3: Parameters resulting from fits of the two-pion correlation function to Lorentzian, Gaussian and Lévy forms for the secondary pion set obtained at $\sqrt{s_{NN}} = 5.8$ GeV.

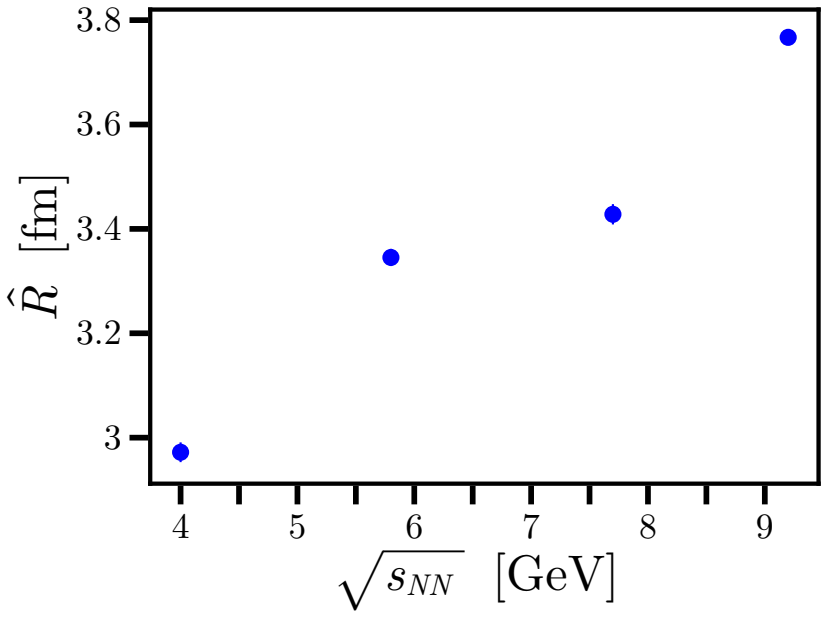

Figure 4.3: Scale parameter, $\hat{R}$, as a function of the collision energy, $\sqrt{s_{NN}}$, for the complete set of pions obtained from Bi+Bi collisions with impact parameter $b = 0 - 1$ fm. $\hat{R}$ is obtained from the fits to a Lévy form and Eq. (4.4).

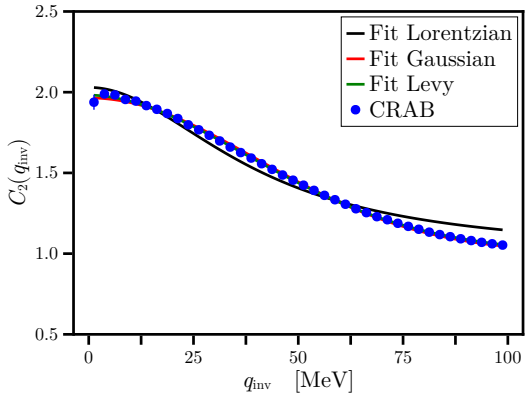

(a) Primary pions

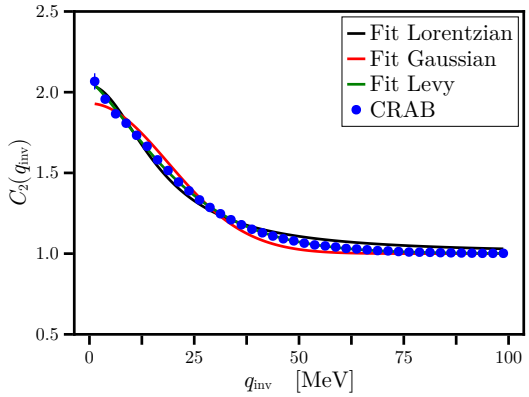

(b) Secondary pions

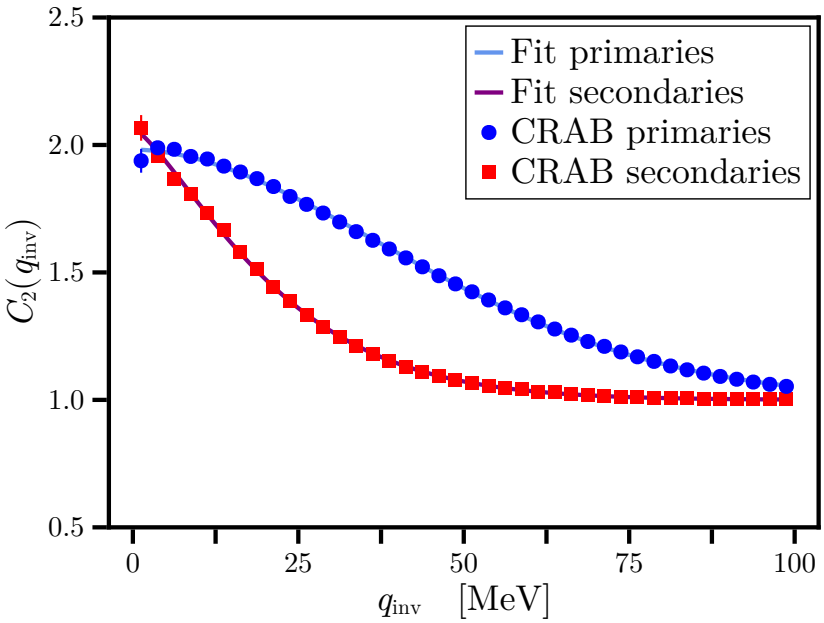

(c) Primary and secondary pions

Figure 4.4: Two-pion correlation function for Bi+Bi collisions at $\sqrt{s_{NN}} = 5.8$ GeV, with impact parameter $b = 0 - 1$ fm for (a) primary and (b) secondary pions. The blue dots represent the output of CRAB, while the solid lines of different colors represent the Lorentzian (black), Gaussian (red) and Lévy (green) fits. The comparison between the correlation function of primary and secondary pions, together with its fits to the Lévy form is shown in (c), where the CRAB output is represented by blue dots for the case of primary pions set and by red squares for the case of secondary pions, while the solid lines represent the fit to Lévy forms shown in (a) and (b).

the correlation function is obtained with the Lévy form. This holds true for the range of explored collision energies. Hence, the same analysis can be done for the rest of the simulated collision energies (see Appendix A).

Figure 4.5 shows the evolution of the source radii and the Lévy index of stability with the collision energy for the sets of primary and secondary pions, while Fig. 4.6 shows the comparison between the evolution of the source size and the Lévy index of stability for the complete, primary and secondary pions sets. Notice that for the separate samples of primary and secondary pions. However, R_{inv} grows with the collision energy from the lowest to the largest energy considered, this growth is non-monotonic. The index α slightly decreases with the collision energy from the lowest to the largest energy considered but, except for the case of the primary pion sample, the overall decrease is non-monotonic. For all the energies considered, we observe the source parameters hierarchies $R_{\text{inv, prim}} < R_{\text{inv, all}} < R_{\text{inv, second}}$ and $\alpha_{\text{second}} \lesssim \alpha_{\text{all}} < \alpha_{\text{prim}}$. Hence, the general behaviour for the source radii is to grow with the collision energy, while the Lévy index of stability does not have a clear general tendency, except for the case of primary pions, which tend to deviate for the Gaussian case, signalling the importance of Lévy distributions when describing this phenomenon at higher collision energies. Also, the behaviour and values of R_{inv} and α for secondary pions are very similar to those of the complete pions.

Figure 4.7 shows the scale parameter $\hat{R}$ evolution with the collision energy for the sets of primary and secondary pions. The comparison of the complete sample with the primary and secondary pions is also shown in Fig. 4.7. Notice that, once again, the scale parameter grows monotonically with the collision energy.

Ref. [17] also found that the inverse of the scale parameter, $\hat{R}^{-1}$, has a linear behaviour as a function of the pion transverse mass $m_T \equiv \sqrt{m^2 + K_T^2}$, with $K_T \equiv \frac{1}{2}\sqrt{K_x^2 + K_y^2}$. The explanation of this linearity is unknown, according to Ref. [17]. This linear behaviour is also shown as a function of the collision energy in Fig. 4.8.

4.3 Two-pion correlation function with finite resolution

To account for finite resolution effects, the NICA-MPD collaboration has reported to have a minimum momentum resolution around 1.0 and 1.5 % for single-particles with total momentum, $|\mathbf{p}|^2 = p_\parallel^2 + p_\perp^2$, around 0.2 GeV. For particles whose total momentum is between 0.6 and 0.8 GeV, the minimum momentum resolution is around 2 % [49], as shown in Fig. 4.9. Therefore, the average relative momentum resolution of MPD can be thought to be about 10 MeV. This effect can be included in this work by fixing the smearing parameter of CRAB to 10 MeV. The smearing function of CRAB adds to each components of the momentum of the particle a random value that is Gaussianlly distributed, whose mean is zero and its standard deviation is the value of the smearing parameter. The effect of this smearing function is to "spread" the values of the momentum for each pion by a value related to the minimum resolution of the detector.

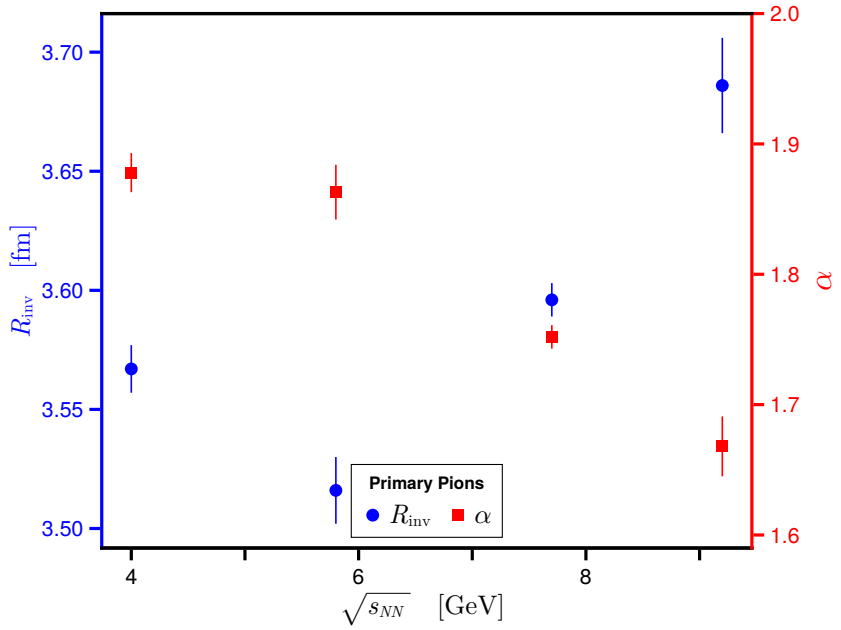

(a) Primary pions

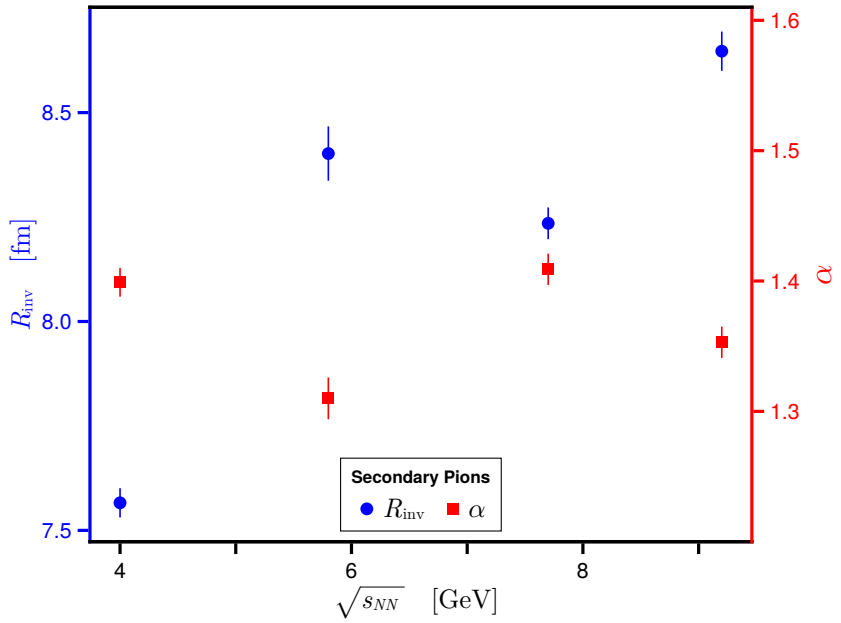

(b) Secondary pions

Figure 4.5: Source size $R_{\rm inv}$ and Lévy index of stability α as a function of the collision energy, $\sqrt{s_{NN}}$, for (a) the primary pions and (b) the secondary pions obtained from Bi+Bi collisions with impact parameter $b = 0 - 1$ fm. $R_{\rm inv}$ and α are obtained from fits to a Lévy form.

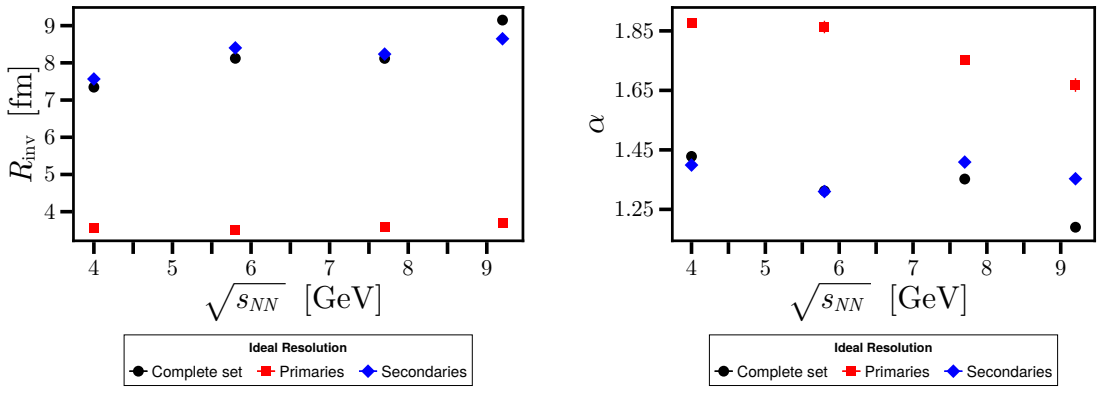

(a) $R_{\rm inv}$ (b) α

Figure 4.6: Comparison of the behaviour of (a) the source size and (b) the Lévy index of stability for the complete (black dots), primary (blue squares) and secondary (red diamonds) obtained from Bi+Bi collisions with impact parameter $b = 0-1$ fm. $R_{\rm inv}$ and α are obtained from fits to a Lévy form.

	$R_{\rm inv}$ [fm]	λ	α	χ^2 / n.d.f.
Lorentzian	4.449 ± 0.13	0.641 ± 0.013	—	28.227
Gaussian	5.856 ± 0.094	0.582 ± 0.008	—	13.295
Lévy	6.238 ± 0.046	0.632 ± 0.004	1.502 ± 0.022	0.912

Table 4.4: Parameters resulting from fits of the two-pion correlation function, obtained at $\sqrt{s_{NN}} = 5.8$ GeV, to Lorentzian, Gaussian, and Lévy forms for the complete pion set that takes into account the finite resolution effects of MPD, by setting the smearing parameter to 10 MeV.

In this section, the analysis of the previous section is repeated but includes the finite resolution effects and compared with the results obtained for the ideal resolution case. Once again, only the case of $\sqrt{s_{NN}} = 5.8$ GeV will be presented, but the full analysis of the four collision energies will be presented on Appendix B for the interested reader.

4.3.1 Finite resolution effects on the two-pion correlation function for the complete set of pions

The effects of the finite resolution on the two-pion correlation function can be seen in Fig. 4.10, with the fit parameters shown in Table 4.4. Once again, the fit to the Lévy form is the one that better describes the correlation function. The same is true for the rest of the explored collision energies.

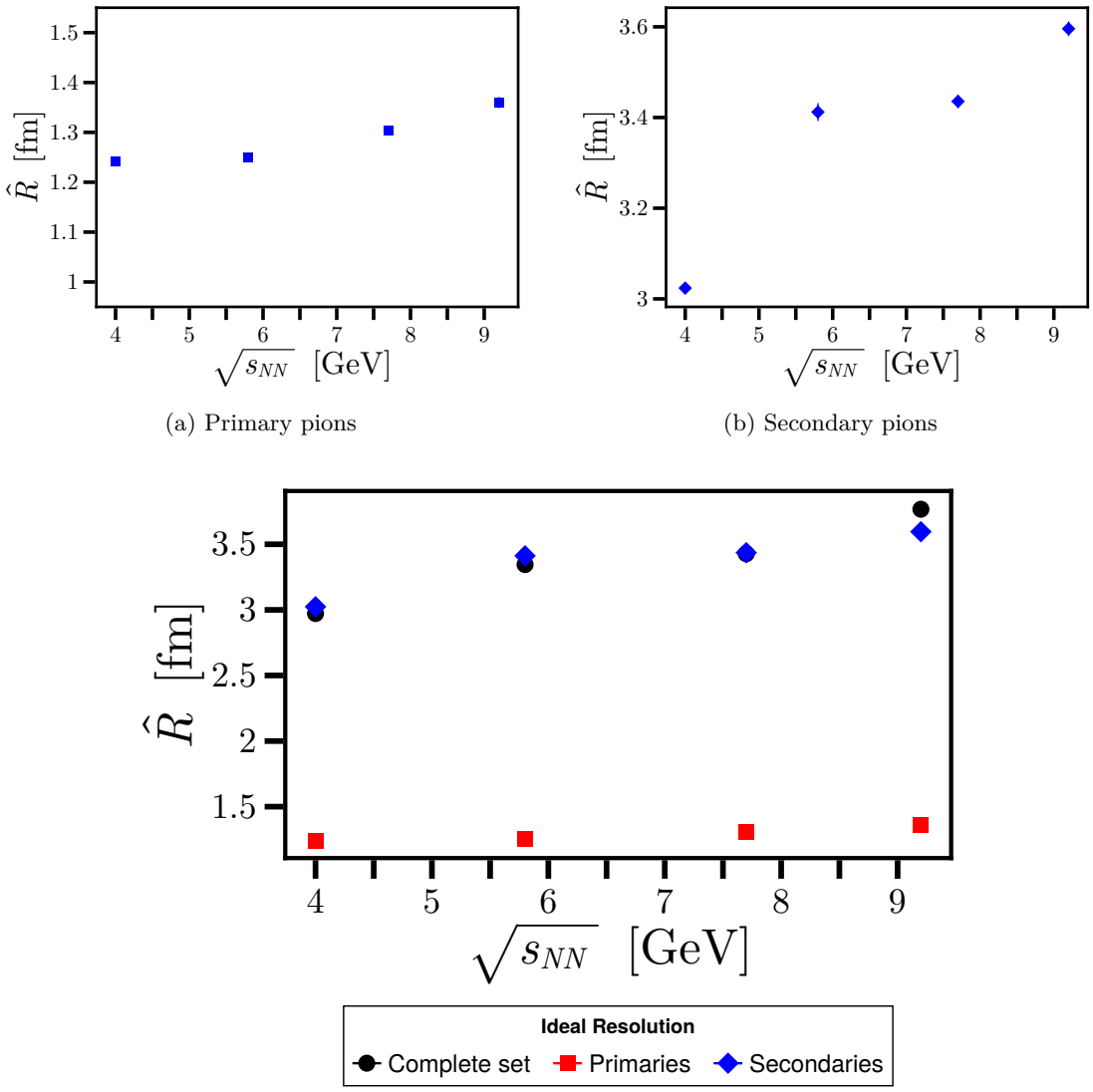

(a) Primary pions

(b) Secondary pions

(c) Comparison of the three samples

Figure 4.7: Scale parameter, $\hat{R}$, as a function of the collision energy, $\sqrt{s_{NN}}$, for (a) the primary pions and (b) the secondary pions obtained from Bi+Bi collisions with impact parameter $b = 0 - 1$ fm. $\hat{R}$ is obtained from the fits to a Lévy form and Eq. (4.4). The comparison between the complete, primary and secondary pions is shown in (c).

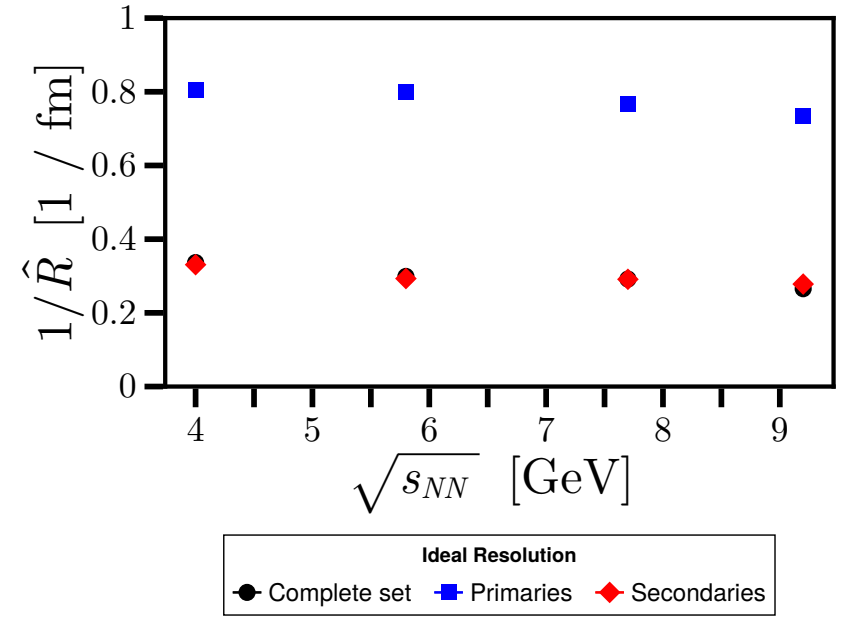

Figure 4.8: Inverse of the scale parameter, $\hat{R}^{-1}$ as a function of the collision energy, $\sqrt{s_{NN}}$, for the complete (black dots), primary (blue squares) and secondary (red diamonds) sets.

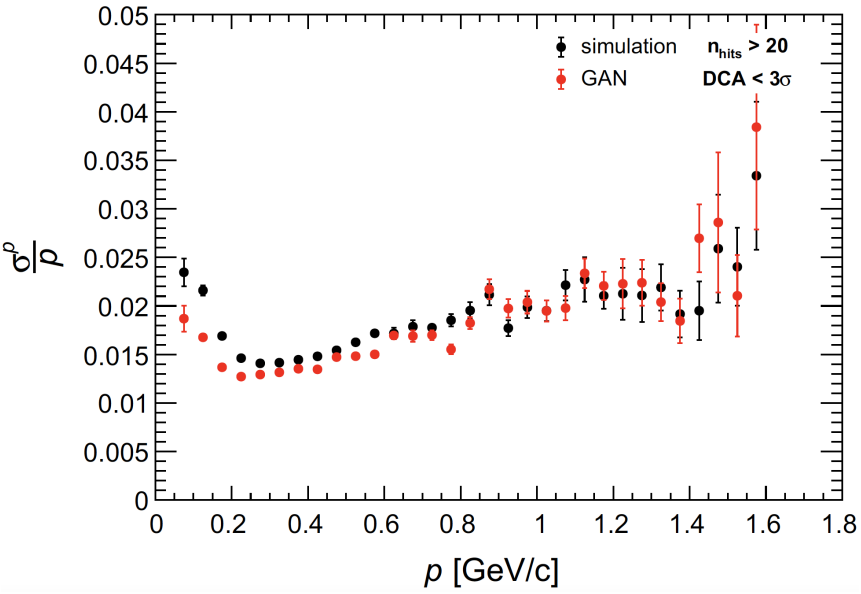

Figure 4.9: MPD total momentum resolution as a function of the total momentum. Credits: A. Maevskiy *et al.*, taken from Ref. [49].

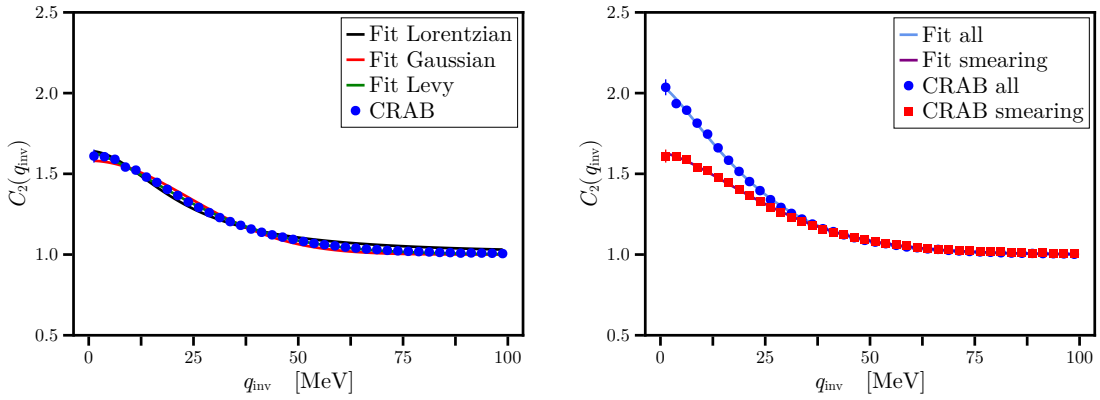

(a) Fits to finite resolution correlation function

(b) Comparison between ideal and finite resolution

Figure 4.10: Two-pion correlation function of Bi+Bi collisions at $\sqrt{s_{NN}} = 5.8$ GeV, with impact parameter $b = 0 - 1$ fm. In (a), the output of CRAB is shown but with the finite resolution effect of MPD, with a smearing of 10 MeV. The blue dots represent the output of CRAB, while the solid lines represent the fits to the Lorentz, Gaussian, and Lévy forms. In (b), a comparison between the ideal and finite resolution is made, where the blue dots represent the same output of CRAB of Figure 4.1, while the red dots include the finite resolution effect of MPD, with a smearing of 10 MeV. Solid lines represent the fit to a Lévy form.

	R_{inv} [fm]	λ	α	χ^2 / n.d.f.
w. smearing	6.238 ± 0.046	0.632 ± 0.004	1.502 ± 0.022	0.912
wo. smearing	8.121 ± 0.059	1.05 ± 0.006	1.312 ± 0.015	0.835

Table 4.5: Results of the fit to the two-pion correlation function with a Lévy form accounting for a finite resolution of the detector, setting a smearing of 10 MeV for the complete pion set obtained at $\sqrt{s_{NN}} = 5.8$ GeV.

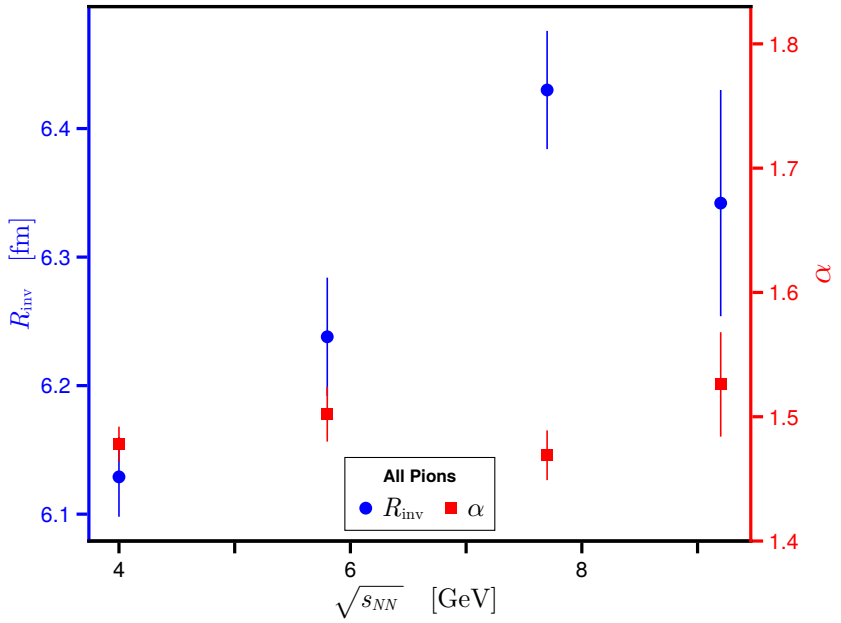

Figure 4.11: Source size $R_{\rm inv}$ and Lévy index of stability α as a function of the collision energy for the complete set of pions obtained from Bi+Bi collisions with impact parameter $b = 0 - 1$ fm and a smearing of 10 MeV. $R_{\rm inv}$ and α are obtained from the fit to a Lévy form.

The comparison of the fit parameters of the Lévy forms between the case of ideal and finite resolution is shown in Table 4.5. Notice that the finite resolution has the effect of significantly diminishing the source size (by about 23 %) and the value of the intercept (by about 39 %) while increasing the value of the Lévy stability index (by about 14 %). While for the different energies considered, the effect of the finite resolution is of different intensity, in average, its effect is to diminish, on average, the source size by 23 % and the value of the intercept by 39 %, while increasing, the value of the Lévy stability index by 14 %, in average.

The evolution of the source radii and the Lévy index with respect to the collision energy, accounting for the finite resolution effects of the detector, are shown in Fig. 4.11. Notice that $R_{\rm inv}$ shows an overall tendency to increase with the collision energy, whereas α is basically constant around the same value $\alpha \simeq 1.5$. This behaviour is in agreement with the preliminary results of the STAR collaboration [50], which indicate that α decreases very slowly as a function of the collision energy.

Figure 4.12 shows the behaviour of $\hat{R}$ as a function of the collision energy for the complete set of pions, accounting for the finite resolution effects of the detector. Notice that the scale parameter monotonically grows with the collision energy, just as in the case

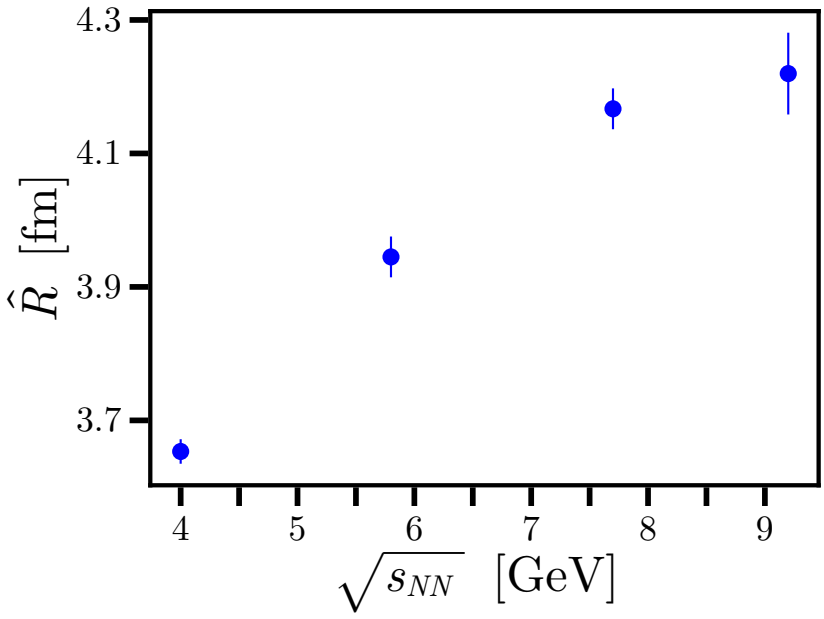

Figure 4.12: Scale parameter, $\hat{R}$, as a function of the collision energy, $\sqrt{s_{NN}}$, for the complete set of pions obtained from Bi+Bi collisions with impact parameter $b = 0 - 1$ fm and a smearing of 10 MeV. $\hat{R}$ is obtained from the fits to a Lévy form and Eq. (4.4).

	R_{inv} [fm]	λ	α	χ^2 / n.d.f.
Lorentzian	2.341 ± 8.843	0.93 ± 0.014	—	60.619
Gaussian	3.339 ± 0.027	0.869 ± 0.006	—	13.614
Lévy	3.426 ± 0.012	0.905 ± 0.003	1.709 ± 0.016	1.615

Table 4.6: Parameters resulting from fits of the two-pion correlation function, obtained at $\sqrt{s_{NN}} = 5.8$ GeV, to Lorentzian, Gaussian, and Lévy forms for the primary pions, accounting for a finite resolution of the detector, setting a smearing of 10 MeV.

	R_{inv} [fm]	λ	α	χ^2 / n.d.f.
Lorentzian	4.673 ± 0.147	0.65 ± 0.014	—	31.385
Gaussian	6.083 ± 0.108	0.587 ± 0.009	—	10.753
Lévy	6.591 ± 0.054	0.647 ± 0.005	1.447 ± 0.022	0.259

Table 4.7: Parameters resulting from fits of the two-pion correlation function, obtained at $\sqrt{s_{NN}} = 5.8$ GeV, to Lorentzian, Gaussian, and Lévy forms for the secondary pions, accounting for a finite resolution of the detector, setting a smearing of 10 MeV.

without finite resolution effects.

4.3.2 Finite resolution effects on the two-pion correlation function for the separated samples

The effect of the finite resolution on the separated samples, as well as the fits to the Lorentzian, Gaussian, and Lévy forms are shown in Fig. 4.4, while Tables 4.6 and 4.7 show the resulting fit parameters for primary and secondary pions, respectively. Figure 4.13 also shows the comparison between the effects of the finite resolution for primary and secondary pions.

As it has happened recurrently, the fit to the Lévy form is the one that better describes the correlation function for both primary and secondary pions, and the same happens for the whole range of explored collision energies, and hence, the same analysis can be done for the rest of the collision energies (see Appendix B).

The comparisons of the fit parameters of the Lévy forms between the case of ideal resolution and finite resolution for primary and secondary pions are shown in Tables 4.8 and 4.9, respectively.

Notice that, once again, the finite resolution has the effect of diminishing the source size (by about 2 % for primary pions and about 21 %, for secondary pions) and the value of the intercept (by about 8 % for primary pions and about 39 % for secondary pions), while the value of the Lévy index decreases for primary pions (by about 8 %) and increases for secondary pions (by about 10 %). This means that the effect of the finite resolution is of the same order for the set containing all the pions as for the set containing

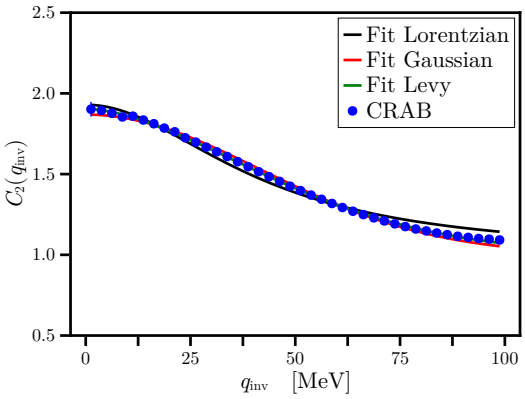

(a) Primary pions

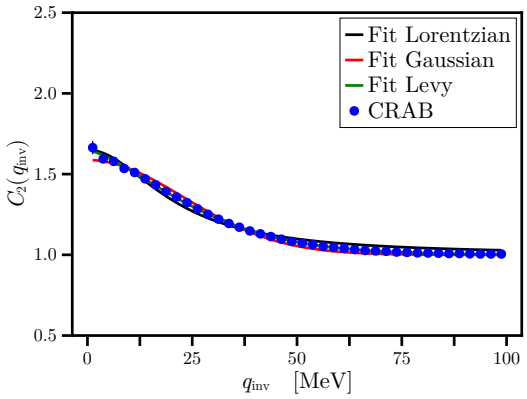

(b) Secondary pions

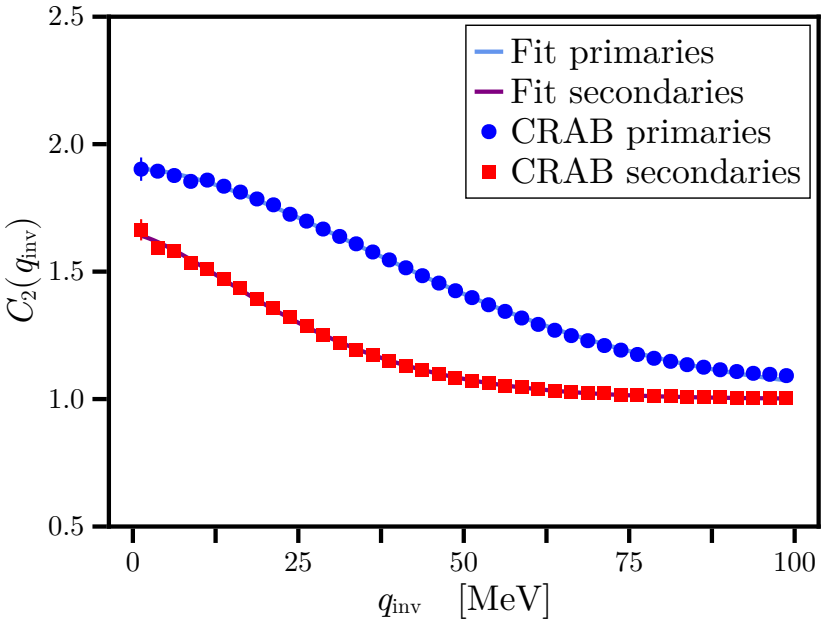

(c) Primary and secondary pions

Figure 4.13: Two-pion correlation function of (a) primary and (b) secondary pions, produced in Bi+Bi collisions at $\sqrt{s_{NN}} = 5.8$ GeV, with impact parameter $b = 0 - 1$ fm. The blue dots and the red squares represent the output of CRAB with a smearing of 10 MeV, while the solid lines represent the fits Lorentzian (black), Gaussian (red), and Lévy (green) fits. The two-pion correlation function of primary and secondary pion, together with its fits to the Lévy forms are compared in (c).

	R_{inv} [fm]	λ	α	χ^2 / n.d.f.
w. smearing	3.426 ± 0.012	0.905 ± 0.003	1.709 ± 0.016	1.615
wo. smearing	3.516 ± 0.014	0.982 ± 0.004	1.863 ± 0.021	0.353

Table 4.8: Results of the fit to the two-pion correlation function with a Lévy form accounting for a finite resolution of the detector, setting a smearing of 10 MeV for the primary pions obtained at $\sqrt{s_{NN}} = 5.8$ GeV.

	R_{inv} [fm]	λ	α	χ^2 / n.d.f.
w. smearing	6.591 ± 0.054	0.647 ± 0.005	1.447 ± 0.022	0.259
wo. smearing	8.402 ± 0.065	1.066 ± 0.007	1.31 ± 0.016	0.321

Table 4.9: Results of the fit to the two-pion correlation function with a Lévy form accounting for a finite resolution of the detector, setting a smearing of 10 MeV for the secondary pions obtained at $\sqrt{s_{NN}} = 5.8$ GeV.

only the secondary pions, while the effect of a finite resolution barely affects the set of primary pions. Additionally, the hierarchy of the fit parameters remains the same for the invariant radii, $R_{\text{inv, prim, FR}} < R_{\text{inv, all, FR}} < R_{\text{inv, second, FR}}$, but it changes for the intercept parameter becoming $\lambda_{\text{all, FR}} < \lambda_{\text{second, FR}} < \lambda_{\text{prim, FR}}$, and it remains the same for $\alpha_{\text{second, FR}} < \alpha_{\text{all, FR}} < \alpha_{\text{prim, FR}}$. For the different energies considered, these hierarchies hold for the invariant radii and for the Lévy index of stability, but the hierarchy of $\lambda_{\text{all, FR}}$ and $\lambda_{\text{second, FR}}$ changes for some energies.

Figure 4.14 shows the evolution of the source radii and the Lévy index with respect to the collision energy for the sets separating the pion sample into primary and secondary pions, accounting for the effects of the finite resolution of the detector, while Fig. 4.15 shows the comparison between the evolution of the source size and the Lévy index of stability for the complete, primary and secondary pion sets, with a smearing of 10 MeV. Notice that for the set of primary pions, R_{inv} is basically constant for the energy range considered whereas α shows a moderate decrease with energy. This means that a finite momentum resolution has a small effect on the pions of primary origin. The values for R_{inv} and α for the set of secondary pions are closer to the corresponding parameters when the whole pion sample is considered. This means that when no separation of the sample between primary and secondary pions is made, the full sample is dominated by the secondary pions. As it happened for the case of the whole sample of pions, shown in Fig. 4.11, for the set of secondary pions, R_{inv} shows an overall tendency to increase with the collision energy, whereas for both of these samples, α is basically constant around the same value $\alpha \simeq 1.5$. It also can be shown that, as the collision energy increases, the set of pions of primary origin are worse described by a Gaussian fit. In this sense, the Lévy fit becomes a better alternative for the correlation function as the collision energy increases.

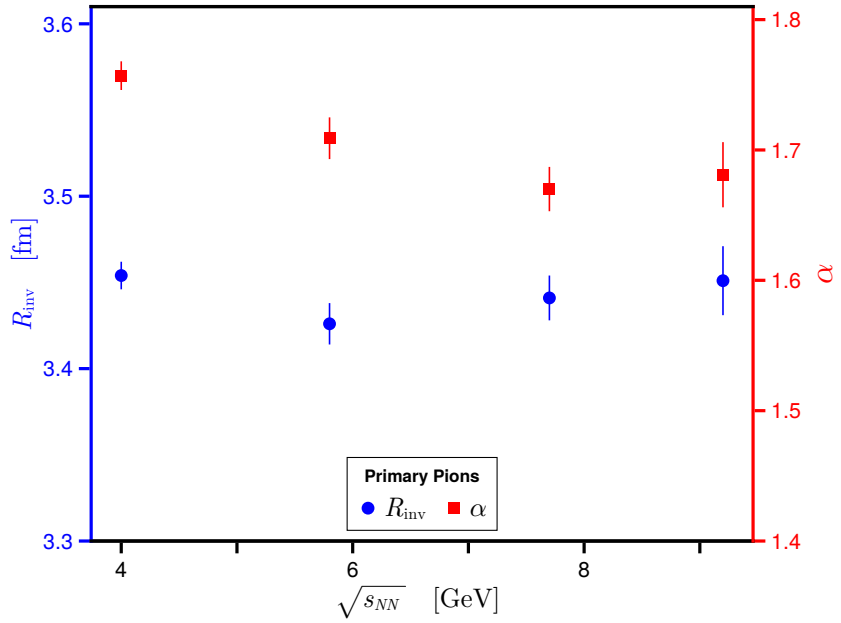

(a) Primary pions

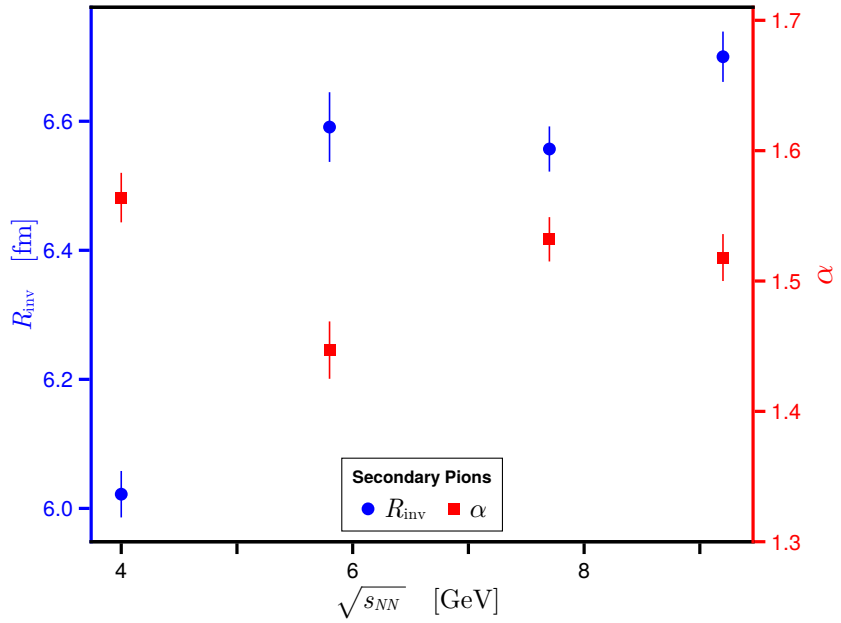

(b) Secondary pions

Figure 4.14: Source size R_{inv} and Lévy index of stability α as a function of the collision energy for (a) primary and (b) secondary pions obtained from Bi+Bi collisions with impact parameter $b = 0 - 1$ fm and a smearing of 10 MeV. R_{inv} and α are obtained from the fit to a Lévy form.

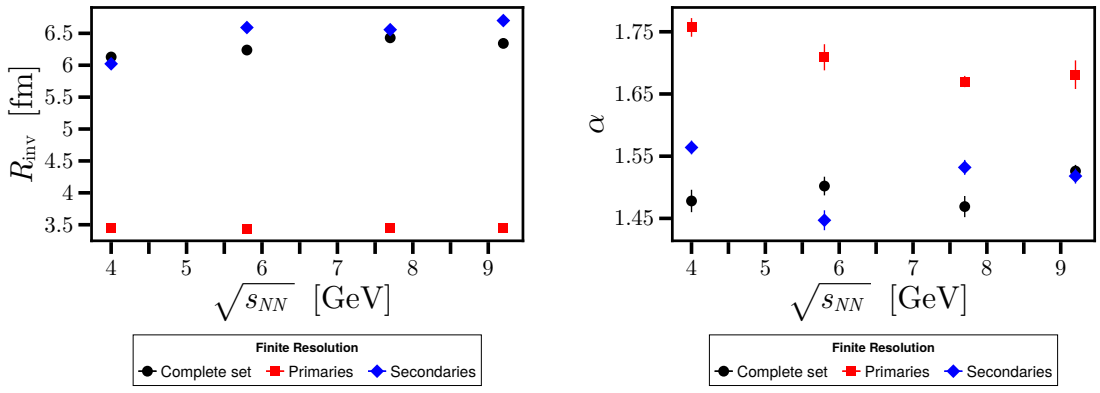

(a) $R_{\rm inv}$ (b) α

Figure 4.15: Comparison of the behaviour of (a) the source size and (b) the Lévy index of stability for the complete (black dots), primary (blue squares) and secondary (red diamonds) obtained from Bi+Bi collisions with impact parameter $b = 0 - 1$ fm and a smearing of 10 MeV. $R_{\rm inv}$ and α are obtained from fits to a Lévy form.

Figure 4.16 shows the scale parameter $\hat{R}$ evolution with the collision energy for the sets of primary and secondary pions. The comparison of the complete sample with the primary and secondary pions is also shown in Fig. 4.16. Notice that, once again, the scale parameter grows monotonically with the collision energy. Fig. 4.17 shows the inverse of the scale parameter, accounting for the finite resolution effects. Once again, the behaviour of the inverse of the scale parameter is linear with the collision energy.

Table 4.10 shows the evolution of the intercept parameter λ with respect to the collision energy for the complete set of pions, as well as for the primary and secondary pions. Notice that for all the cases, the value of λ decreases as the energy increases. Nonetheless, for the complete set and the secondary pions the decrease is around 10 %, whereas for the primary pions the decrease is only marginal and around 2 %.

$\sqrt{s_{NN}}$ [GeV]	$\lambda_{\rm all}$	$\lambda_{\rm prim}$	$\lambda_{\rm second}$
4.0	0.677 ± 0.003	0.907 ± 0.002	0.651 ± 0.004
5.8	0.632 ± 0.004	0.905 ± 0.003	0.647 ± 0.005
7.7	0.625 ± 0.004	0.9 ± 0.003	0.608 ± 0.003
9.2	0.595 ± 0.007	0.887 ± 0.005	0.602 ± 0.003

Table 4.10: Evolution of the intercept parameter λ with the collision energy for the complete, primary and secondary sets of pions, obtained from fits to a Lévy form accounting for a finite resolution of the detector with a smearing of 10 MeV.

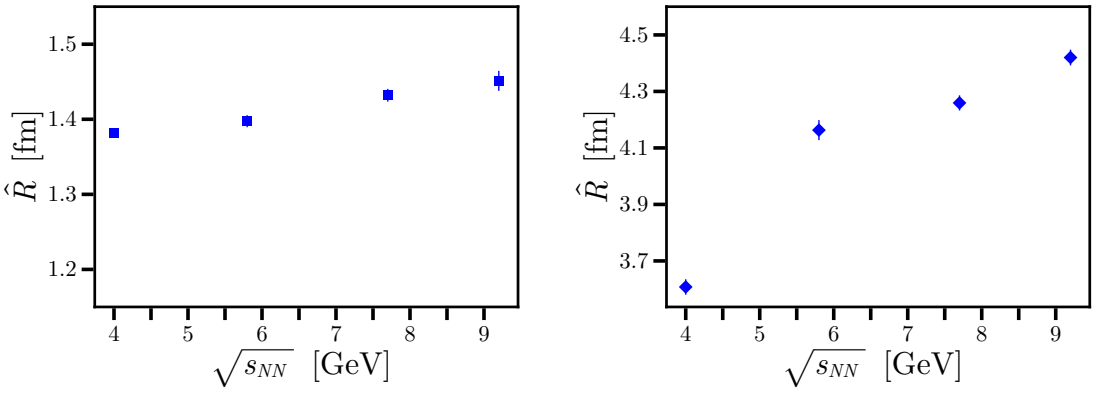

(a) Primary pions

(b) Secondary pions

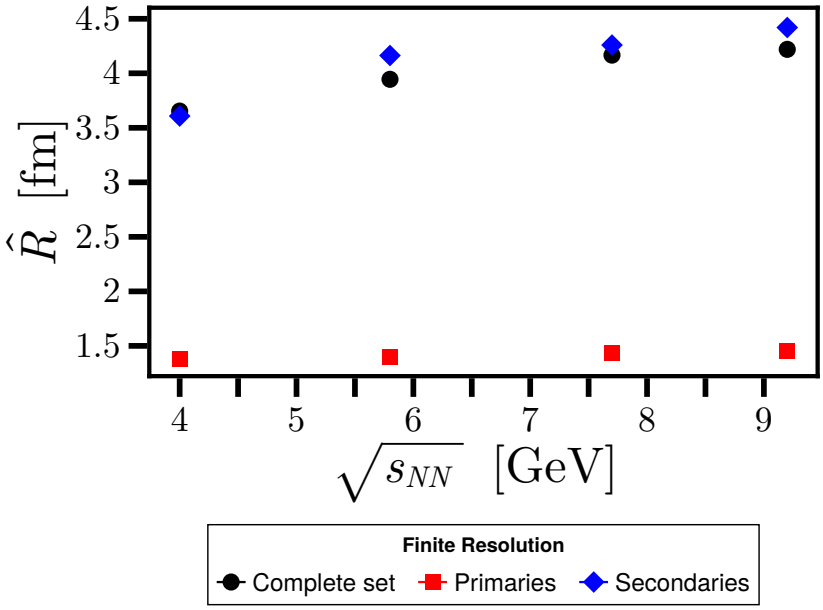

(c) Comparison of the three samples

Figure 4.16: Scale parameter, $\hat{R}$, as a function of the collision energy, $\sqrt{s_{NN}}$, for (a) the primary pions and (b) the secondary pions obtained from Bi+Bi collisions with impact parameter $b = 0 - 1$ fm and a smearing of 10 MeV. $\hat{R}$ is obtained from the fits to a Lévy form and Eq. (4.4). The comparison between the complete, primary and secondary pions is shown in (c).

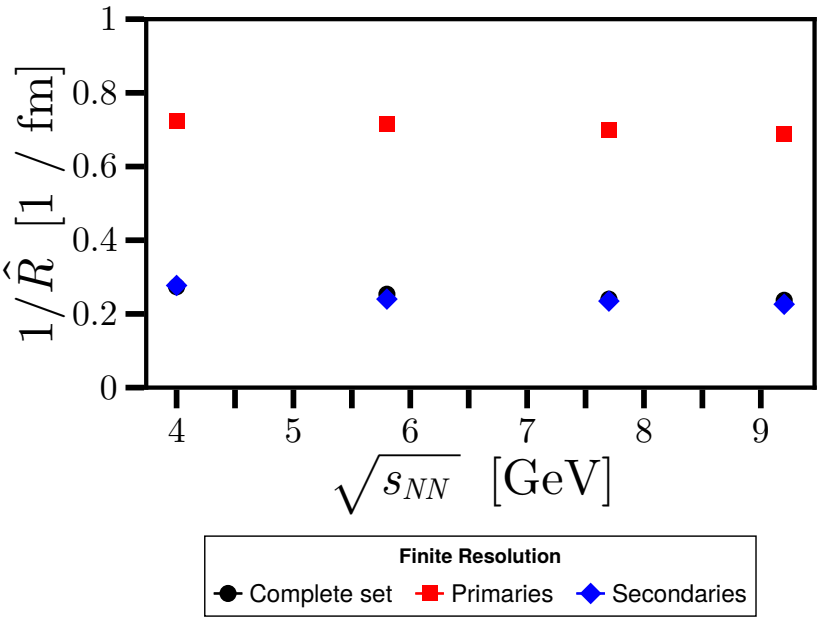

Figure 4.17: Inverse of the scale parameter, $\hat{R}^{-1}$, as a function of the collision energy, $\sqrt{s_{NN}}$, for the complete (black dots), primary (red squares) and secondary (blue diamonds) sets, accounting for the finite resolution effects.

As it was discussed in Chapter 2, within the context of the *core-halo* picture, the intercept parameter can be related to the square of the fraction of pions coming from the *core*. This implies, according to Eq. (2.43), that between 77 % and 82 % of the pions should come from the *core*, and only a smaller fraction should come from the *halo*. According to the previously discussed definition of secondary particles, pions of secondary origin are those coming from the decay of long-lived resonances. The results show that simulating a finite resolution detector with a smearing $\Delta q \sim 10$ MeV, the fraction of pions of secondary origin together with the pions of primary origin come from a space-time region within R_{inv}, such that $\Delta q \cdot R_{\text{inv}} \sim 1$ implying that $R_{\text{inv}} \lesssim 20$ fm. In other words, a minimum momentum resolution of 10 MeV translates into a maximum source size of 20 fm, from where pion pairs can be identified. Since the intercept parameter for secondary particles decreases more than for the primaries as the energy increases, this means that for larger energies, long-lived resonances decay further away from the center, as expected, and thus contribute less to the population of *core* pions. As discussed in Chapter 3, from the UrQMD simulation, it is possible to directly identify that the average fraction of pions produced by primary processes, which always populate the *core*, increases marginally with energy to be between 6 % and 13 %. Therefore, we can conclude that for lower energies, the *core* is mainly populated by pions produced from slow moving resonance decays and that this population gradually decreases as the collision energy increases.

CHAPTER 5

Conclusions

In this work, the two-pion correlation function has been presented as a prime femtoscopy tool that can be used in the context of the study of the interaction region formed in relativistic heavy-ion collisions. The main formalism of the two-particle has been presented and the rationale for using this correlation functions as a tool for extracting the pion source size and shape was also presented.

For collisions whose energy is within the NICA energy range, the evolution with collision energy of the parameters that describe the two-pion correlation function has been investigated. Monte Carlo simulations have been performed using the Ultra-relativistic Quantum Molecular Dynamics (UrQMD) event generator to produce five million events for each of the following center-of-mass collision energies: $\sqrt{s_{NN}} = 4.0$, 5.8, 7.7 and 9.2 GeV. In each case, the quantum correlations are included using the CRAB formalism, which is implemented as an analyzing code. No other source of correlations but the quantum ones have been considered. The correlation function is studied as a function of the invariant relative pair momentum for a fixed value of the average pair momentum. To find the parameters that describe the correlation function, fits were performed using Gaussian, Lorentzian and symmetric Lévy distributions. The distribution that provides the better description of the correlations is the Lévy distribution for the different settings and across the considered energy range. The simulated pion sample was separated into its primary and secondary components. The latter is defined as the set of pions coming from the decay of long-lived resonances, concretely ρ, Δ, ω, and K^*. As it was expected, the source size for the sample of secondary pions is larger than that for the whole sample and significantly larger than the source size of the primary pions. In some cases, the intercept parameter

exhibits the same hierarchy as the source size, whereas the Lévy index exhibits the opposite. For the case of the primary pion sample, the Lévy index shows an overall slight decrease with collision energy, however, the secondary and full set of pions do not show a clear tendency with collision energy. When comparing the source parameters of the complete pion sample with those of primary and secondary origin, it is possible to see that the secondary pions dominate the behaviour of the whole set.

In order to obtain a more accurate picture of the space-time characteristics of the pion producing sources, the case of a non-ideal detector was simulated by introducing a smearing parameter in the CRAB code to mimic a minimum resolution for the determination of the relative pair momentum, the value of which is consistent with the expected average momentum resolution reported by the MPD collaboration. From the uncertainty relation between momentum and position, this minimum resolution translates into a maximum source size from where pion pairs can be identified. This smearing produces that the intercept of the correlation function becomes smaller than unity. Within the *core-halo* picture, the impossibility of determining source sizes larger than the inverse of the smearing momentum can be turned into an advantage since the intercept size can be directly identified with the square of the fraction of pions coming from the *core*. The presented results indicate that the pion sample coming from the *core* has a significant component whose origin is the decay of long-lived but slow-moving resonances, as well as a small component of pions from primary processes. The former decreases, whereas the latter increases with collision energy.

In this sense, the analysis of the relative abundance of pions in the *core* coming from resonance decays and primary processes, as the collision energy changes, becomes more important as a tool to study signals of criticality within the NICA energy range. Indeed, when particle-producing processes introduce extra sources of correlations with lengths of the order of the size of the system, the *core* in this case, it is expected that they can be captured, in particular, by a non-monotonic evolution of the Lévy index with collision energy. Since the model of UrQMD that was used in this analysis, which considers the pion emitting source as a hadron gas, does not include a phase transition whose signature could be captured in this kind of analysis, this work can be extended by changing the model and generator to one that does have a phase transition, and then, it might be possible to see which are the effects of this transition on the two-pion correlation function and the space-time parameters that characterize the pion emitting source. This could, in turn, be used as a signal of the presence of the critical phenomena associated with the presence of a critical end-point in the QCD phase diagram, since in the vicinities of the critical end-point, the value of the correlation critical exponent is predicted by theory to be approximately 0.5 and this can be measured with the Lévy index of stability. Even more, with enough statistics, this kind of analysis could constrain the equation of state of nuclear matter. A similar analysis to the one recently proposed has already been performed for the RHIC and LHC energies ($\sqrt{s_{NN}} = 200$ GeV and 2.76 TeV, respectively) in Refs. [51, 52]

APPENDIX A

Two-pion correlation function fits: Ideal resolution case

As it has already been mentioned, the purpose of this Appendix is to show the complete analysis of the two-pion correlation functions obtained for all the explored energies, not considering finite resolution effects.

A.1 Two-pion correlation function for the complete set of pions

Figure A.1 shows the two-pion correlation function for the complete sample of positively charged pions at a collision energy $\sqrt{s_{NN}} = 4.0$ GeV, together with its fits to the Lorentzian, Gaussian and Lévy forms. The resulting fit parameters are shown in Table A.1. Notice that the fit that better describes the correlation function is obtained with the Lévy form.

	R_{inv} [fm]	λ	α	χ^2
Lorentzian	5.213 ± 0.146	1.021 ± 0.02	—	138.842
Gaussian	6.787 ± 0.126	0.922 ± 0.015	—	75.25
Lévy	7.346 ± 0.051	1.018 ± 0.006	1.428 ± 0.018	3.533

Table A.1: Parameters resulting from fits of the two-pion correlation function to Lorentzian, Gaussian and Lévy forms for the complete pion set obtained at $\sqrt{s_{NN}} = 4.0$ GeV.

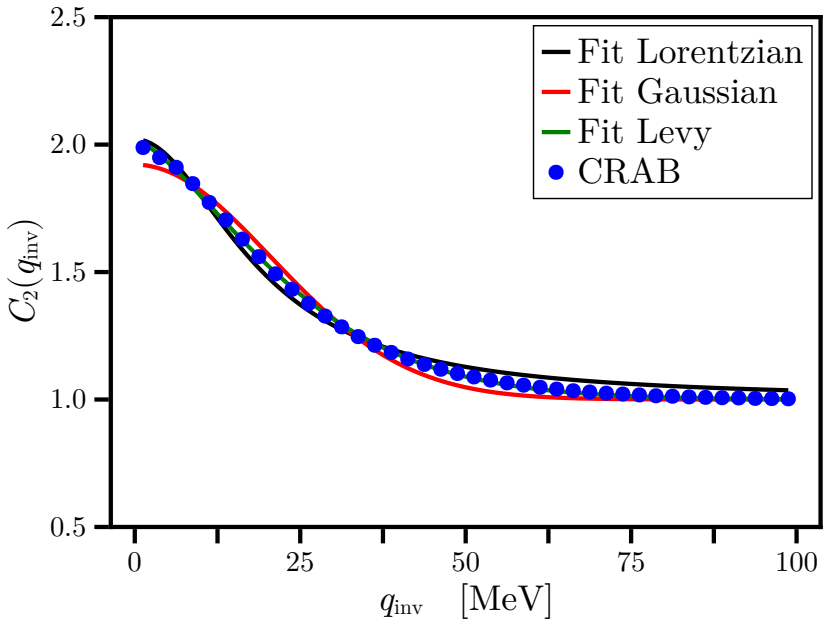

Figure A.1: Two-pion correlation function for Bi+Bi collisions at $\sqrt{s_{NN}} = 4.0$ GeV, with impact parameter $b = 0 - 1$ fm. The blue dots represent the output of CRAB, while the solid lines of different colors represent the Lorentzian (black), Gaussian (red) and Lévy (green) fits.

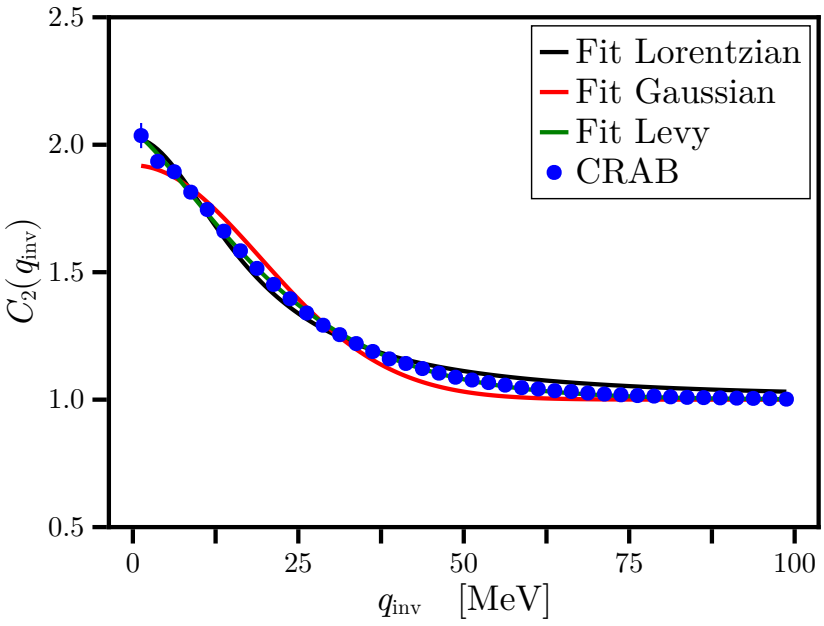

Figure A.2: Two-pion correlation function for Bi+Bi collisions at $\sqrt{s_{NN}} = 5.8$ GeV, with impact parameter $b = 0 - 1$ fm. The blue dots represent the output of CRAB, while the solid lines of different colors represent the Lorentzian (black), Gaussian (red) and Lévy (green) fits.

The two-pion correlation function for the complete sample pions at a collision energy $\sqrt{s_{NN}} = 5.8$ GeV, together with its fits to the Lorentzian, Gaussian and Lévy forms is shown in Fig. A.2. The resulting fit parameters are shown in Table A.2. Notice that the fit that better describes the correlation function is obtained with the Lévy form.

The two-pion correlation function for the complete sample pions at a collision energy $\sqrt{s_{NN}} = 7.7$ GeV, together with its fits to the Lorentzian, Gaussian and Lévy forms is shown in Fig. A.3. The resulting fit parameters are shown in Table A.3. Notice that the fit that better describes the correlation function is obtained with the Lévy form.

The two-pion correlation function for the complete sample pions at a collision energy $\sqrt{s_{NN}} = 9.2$ GeV, together with its fits to the Lorentzian, Gaussian and Lévy forms is shown in Fig. A.4. The resulting fit parameters are shown in Table A.4. Notice that the fit that better describes the correlation function is obtained with the Lévy form.

	R_{inv} [fm]	λ	α	χ^2
Lorentzian	5.632 ± 0.142	1.027 ± 0.018	—	45.27
Gaussian	7.254 ± 0.166	0.919 ± 0.018	—	38.301
Lévy	8.121 ± 0.059	1.05 ± 0.006	1.312 ± 0.015	0.835

Table A.2: Parameters resulting from fits of the two-pion correlation function to Lorentzian, Gaussian and Lévy forms for the complete pion set obtained at $\sqrt{s_{NN}} = 5.8$ GeV.

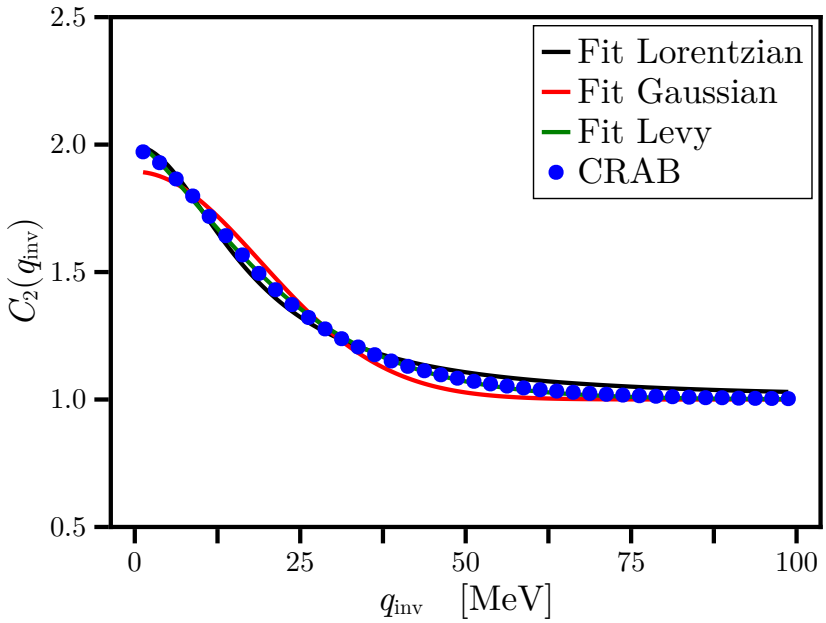

Figure A.3: Two-pion correlation function for Bi+Bi collisions at $\sqrt{s_{NN}} = 7.7$ GeV, with impact parameter $b = 0 - 1$ fm. The blue dots represent the output of CRAB, while the solid lines of different colors represent the Lorentzian (black), Gaussian (red) and Lévy (green) fits.

	R_{inv} [fm]	λ	α	χ^2
Lorentzian	5.688 ± 0.141	0.995 ± 0.017	—	94.24
Gaussian	7.362 ± 0.158	0.894 ± 0.017	—	78.49
Lévy	8.119 ± 0.061	1.007 ± 0.006	1.352 ± 0.017	3.432

Table A.3: Parameters resulting from fits of the two-pion correlation function to Lorentzian, Gaussian and Lévy forms for the complete pion set obtained at $\sqrt{s_{NN}} = 7.7$ GeV.

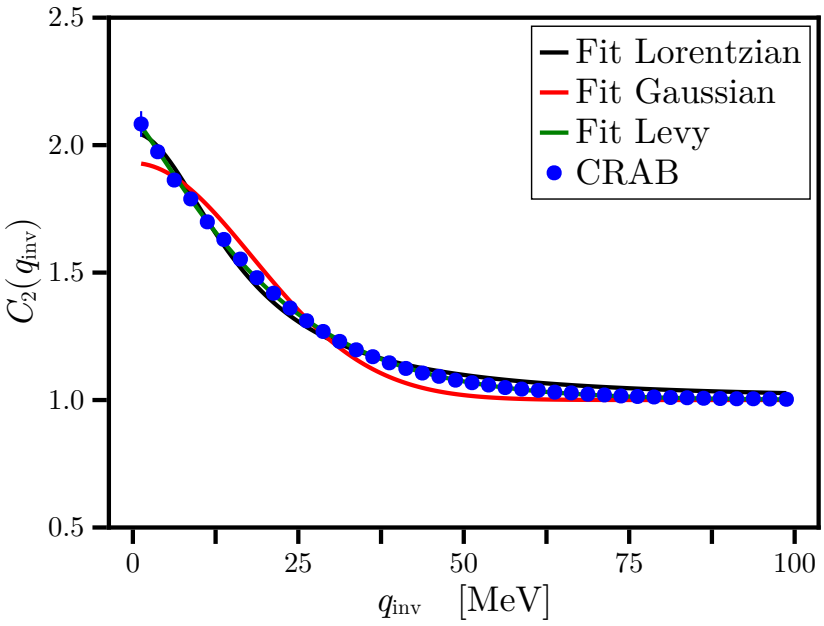

Figure A.4: Two-pion correlation function for Bi+Bi collisions at $\sqrt{s_{NN}} = 9.2$ GeV, with impact parameter $b = 0 - 1$ fm. The blue dots represent the output of CRAB, while the solid lines of different colors represent the Lorentzian (black), Gaussian (red) and Lévy (green) fits.

	R_{inv} [fm]	λ	α	χ^2
Lorentzian	6.124 ± 0.146	1.049 ± 0.018	—	34.342
Gaussian	7.77 ± 0.218	0.93 ± 0.023	—	44.516
Lévy	9.149 ± 0.054	1.109 ± 0.005	1.19 ± 0.01	0.289

Table A.4: Parameters resulting from fits of the two-pion correlation function to Lorentzian, Gaussian and Lévy forms for the complete pion set obtained at $\sqrt{s_{NN}} = 9.2$ GeV.

	R_{inv} [fm]	λ	α	χ^2
Lorentzian	2.494 ± 0.086	1.049 ± 0.024	—	436.399
Gaussian	3.529 ± 0.014	0.982 ± 0.003	—	3.923
Lévy	3.567 ± 0.01	0.998 ± 0.003	1.878 ± 0.015	3.481

Table A.5: Parameters resulting from fits of the two-pion correlation function to Lorentzian, Gaussian and Lévy forms for the primary pion set obtained at $\sqrt{s_{NN}} = 4.0$ GeV.

	R_{inv} [fm]	λ	α	χ^2
Lorentzian	5.346 ± 0.154	1.04 ± 0.021	—	144.286
Gaussian	6.918 ± 0.133	0.936 ± 0.016	—	67.044
Lévy	7.566 ± 0.035	1.043 ± 0.004	1.399 ± 0.011	1.298

Table A.6: Parameters resulting from fits of the two-pion correlation function to Lorentzian, Gaussian and Lévy forms for the secondary pion set obtained at $\sqrt{s_{NN}} = 4.0$ GeV.

A.2 Two-pion correlation function for the separated samples

Figure A.5 shows the two-pion correlation function for primary and secondary pions at a collision energy $\sqrt{s_{NN}} = 4.0$ GeV, together with its fits to the Lorentzian, Gaussian and Lévy forms. The comparison between the correlation function for primary and secondary pions is also shown. Tables A.5 and A.6 show the resulting fit parameters for primary and secondary pions, respectively. Notice that the fit that better describes the correlation function for both, primary and secondary pions, is obtained with the Lévy form.

Figure A.6 shows the two-pion correlation function for primary and secondary pions at a collision energy $\sqrt{s_{NN}} = 5.8$ GeV, together with its fits to the Lorentzian, Gaussian and Lévy forms. The comparison between the correlation function for primary and secondary pions is also shown. Tables A.7 and A.8 show the resulting fit parameters for primary and secondary pions, respectively. Notice that the fit that better describes the correlation function for both, primary and secondary pions, is obtained with the Lévy form.

Figure A.7 shows the two-pion correlation function for primary and secondary pions at a collision energy $\sqrt{s_{NN}} = 7.7$ GeV, together with its fits to the Lorentzian, Gaussian and

	R_{inv} [fm]	λ	α	χ^2
Lorentzian	2.445 ± 0.079	1.03 ± 0.022	—	158.468
Gaussian	3.476 ± 0.017	0.965 ± 0.004	—	3.132
Lévy	3.516 ± 0.014	0.982 ± 0.004	1.863 ± 0.021	0.353

Table A.7: Parameters resulting from fits of the two-pion correlation function to Lorentzian, Gaussian and Lévy forms for the primary pion set obtained at $\sqrt{s_{NN}} = 5.8$ GeV.

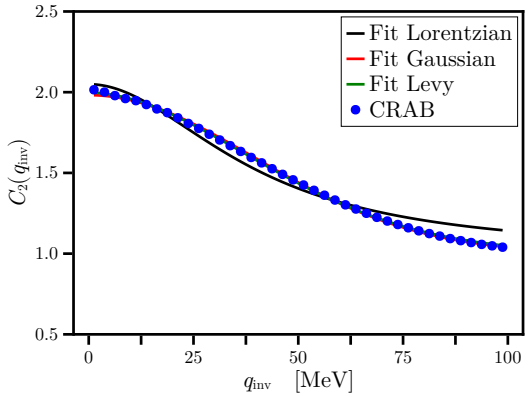

(a) Primary pions

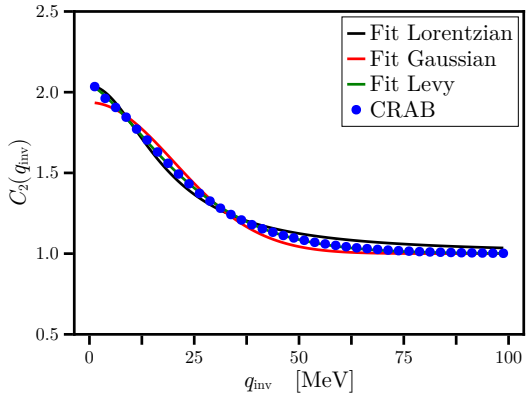

(b) Secondary pions

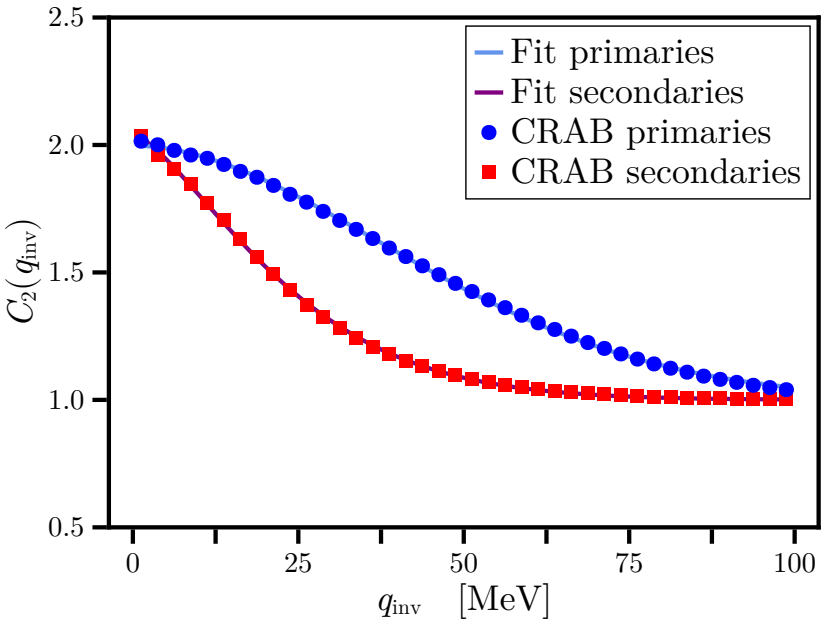

(c) Primary and secondary pions

Figure A.5: Two-pion correlation function for Bi+Bi collisions at $\sqrt{s_{NN}} = 4.0$ GeV, with impact parameter $b = 0 - 1$ fm for (a) primary and (b) secondary pions. The blue dots represent the output of CRAB, while the solid lines of different colors represent the Lorentzian (black), Gaussian (red) and Lévy (green) fits. The comparison between the correlation function of primary and secondary pions, together with its fits to the Lévy form is shown in (c), where the CRAB output is represented by blue dots for the case of primary pions set and by red squares for the case of secondary pions, while the solid lines represent the fit to Lévy forms shown in (a) and (b).

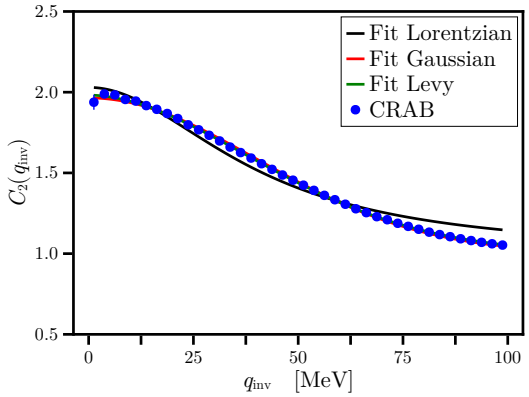

(a) Primary pions

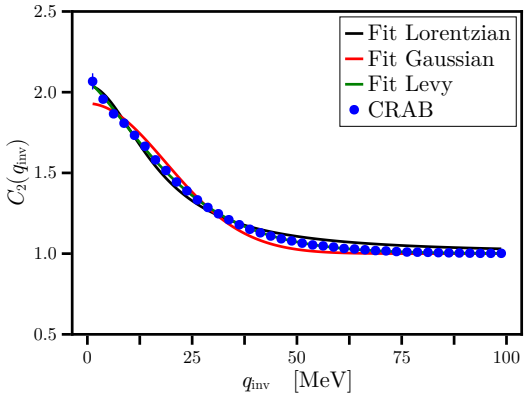

(b) Secondary pions

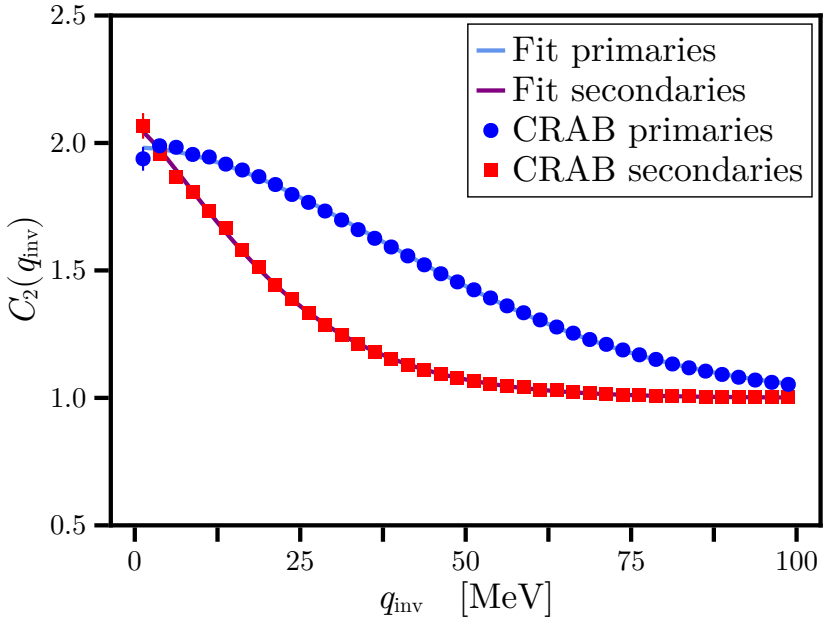

(c) Primary and secondary pions

Figure A.6: Two-pion correlation function for Bi+Bi collisions at $\sqrt{s_{NN}} = 5.8$ GeV, with impact parameter $b = 0 - 1$ fm for (a) primary and (b) secondary pions. The blue dots represent the output of CRAB, while the solid lines of different colors represent the Lorentzian (black), Gaussian (red) and Lévy (green) fits. The comparison between the correlation function of primary and secondary pions, together with its fits to the Lévy form is shown in (c), where the CRAB output is represented by blue dots for the case of primary pions set and by red squares for the case of secondary pions, while the solid lines represent the fit to Lévy forms shown in (a) and (b).

	R_{inv} [fm]	λ	α	χ^2
Lorentzian	5.828 ± 0.168	1.041 ± 0.021	—	54.205
Gaussian	7.455 ± 0.17	0.93 ± 0.018	—	30.012
Lévy	8.402 ± 0.065	1.066 ± 0.007	1.31 ± 0.016	0.321

Table A.8: Parameters resulting from fits of the two-pion correlation function to Lorentzian, Gaussian and Lévy forms for the secondary pion set obtained at $\sqrt{s_{NN}} = 5.8$ GeV.

	R_{inv} [fm]	λ	α	χ^2
Lorentzian	2.494 ± 0.071	1.039 ± 0.019	—	204.973
Gaussian	3.512 ± 0.024	0.968 ± 0.006	—	13.577
Lévy	3.596 ± 0.007	1.002 ± 0.002	1.752 ± 0.009	0.385

Table A.9: Parameters resulting from fits of the two-pion correlation function to Lorentzian, Gaussian and Lévy forms for the primary pion set obtained at $\sqrt{s_{NN}} = 7.7$ GeV.

Lévy forms. The comparison between the correlation function for primary and secondary pions is also shown. Tables A.9 and A.10 show the resulting fit parameters for primary and secondary pions, respectively. Notice that the fit that better describes the correlation function for both, primary and secondary pions, is obtained with the Lévy form.

Figure A.8 shows the two-pion correlation function for primary and secondary pions at a collision energy $\sqrt{s_{NN}} = 9.2$ GeV, together with its fits to the Lorentzian, Gaussian and Lévy forms. The comparison between the correlation function for primary and secondary pions is also shown. Tables A.11 and A.12 show the resulting fit parameters for primary and secondary pions, respectively. Notice that the fit that better describes the correlation function for both, primary and secondary pions, is obtained with the Lévy form.

	R_{inv} [fm]	λ	α	χ^2
Lorentzian	5.847 ± 0.17	0.996 ± 0.02	—	120.194
Gaussian	7.558 ± 0.143	0.896 ± 0.015	—	53.64
Lévy	8.235 ± 0.038	0.995 ± 0.004	1.409 ± 0.012	1.516

Table A.10: Parameters resulting from fits of the two-pion correlation function to Lorentzian, Gaussian and Lévy forms for the secondary pion set obtained at $\sqrt{s_{NN}} = 7.7$ GeV.

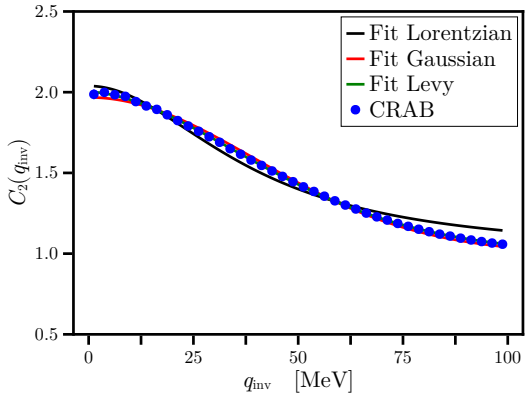

(a) Primary pions

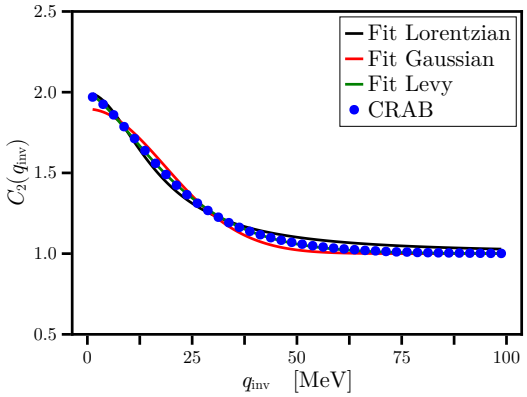

(b) Secondary pions

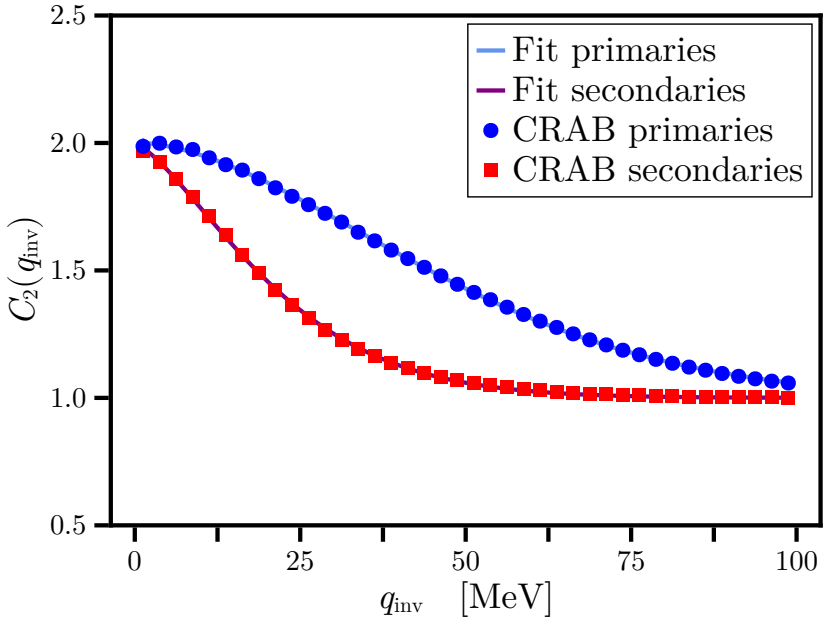

(c) Primary and secondary pions

Figure A.7: Two-pion correlation function for Bi+Bi collisions at $\sqrt{s_{NN}} = 7.7$ GeV, with impact parameter $b = 0 - 1$ fm for (a) primary and (b) secondary pions. The blue dots represent the output of CRAB, while the solid lines of different colors represent the Lorentzian (black), Gaussian (red) and Lévy (green) fits. The comparison between the correlation function of primary and secondary pions, together with its fits to the Lévy form is shown in (c), where the CRAB output is represented by blue dots for the case of primary pions set and by red squares for the case of secondary pions, while the solid lines represent the fit to Lévy forms shown in (a) and (b).

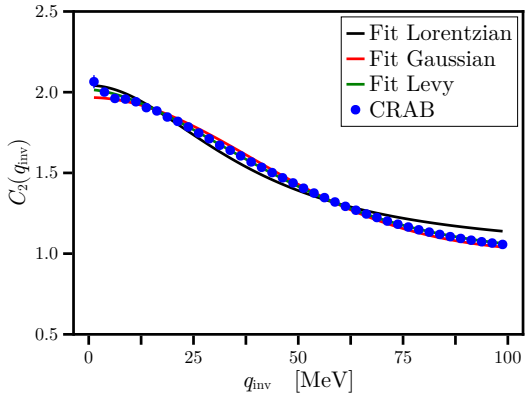

(a) Primary pions

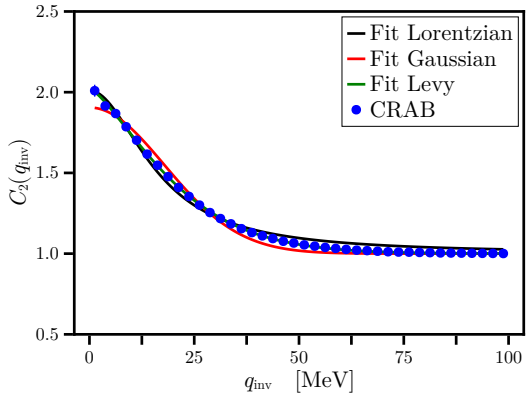

(b) Secondary pions

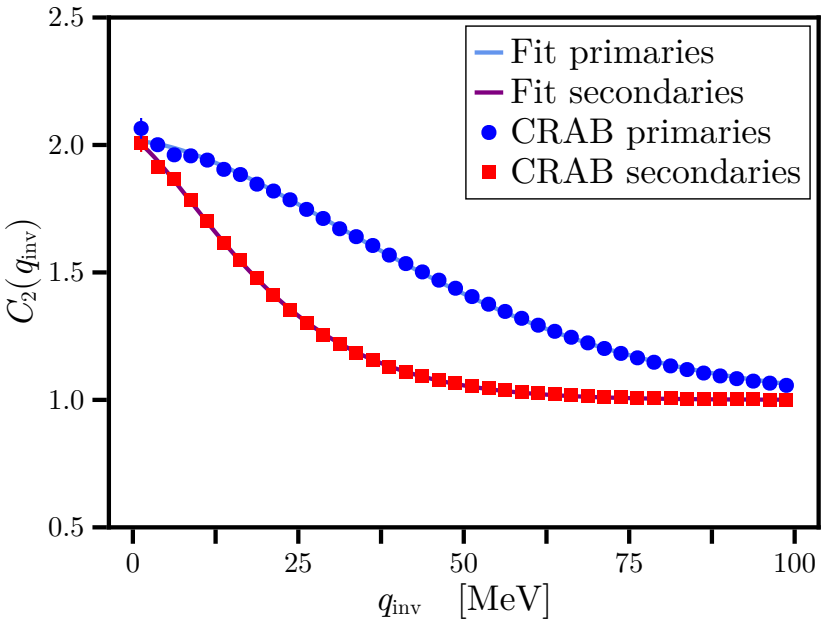

(c) Primary and secondary pions

Figure A.8: Two-pion correlation function for Bi+Bi collisions at $\sqrt{s_{NN}} = 9.2$ GeV, with impact parameter $b = 0 - 1$ fm for (a) primary and (b) secondary pions. The blue dots represent the output of CRAB, while the solid lines of different colors represent the Lorentzian (black), Gaussian (red) and Lévy (green) fits. The comparison between the correlation function of primary and secondary pions, together with its fits to the Lévy form is shown in (c), where the CRAB output is represented by blue dots for the case of primary pions set and by red squares for the case of secondary pions, while the solid lines represent the fit to Lévy forms shown in (a) and (b).

	R_{inv} [fm]	λ	α	χ^2
Lorentzian	2.548 ± 0.07	1.042 ± 0.019	—	144.415
Gaussian	3.559 ± 0.035	0.967 ± 0.008	—	15.472
Lévy	3.686 ± 0.02	1.016 ± 0.005	1.668 ± 0.023	1.074

Table A.11: Parameters resulting from fits of the two-pion correlation function to Lorentzian, Gaussian and Lévy forms for the primary pion set obtained at $\sqrt{s_{NN}} = 9.2$ GeV.

	R_{inv} [fm]	λ	α	χ^2
Lorentzian	6.074 ± 0.172	1.01 ± 0.02	—	66.828
Gaussian	7.801 ± 0.165	0.905 ± 0.017	—	34.548
Lévy	8.647 ± 0.047	1.022 ± 0.005	1.353 ± 0.012	0.469

Table A.12: Parameters resulting from fits of the two-pion correlation function to Lorentzian, Gaussian and Lévy forms for the secondary pion set obtained at $\sqrt{s_{NN}} = 9.2$ GeV.

APPENDIX B

Two-pion correlation function fits: Finite resolution case

In this Appendix, the complete analysis of the obtained correlations functions for all the explored energies and with finite resolution effects is shown. Recall, from Chapter 4, that the MPD relative momentum resolution is about 10 MeV. Thus, this effect can be included into the CRAB formalism by fixing the CRAB smearing parameter to 10 MeV.

B.1 Finite resolution effects on the two-pion correlation function for the complete set of pions

Figure B.1 shows the finite resolution effects on the two-pion correlation function for the complete set of positively charged pions at a collision energy $\sqrt{s_{NN}} = 4.0$ GeV, together with its fits to the Lorentzian, Gaussian and Lévy forms. The resulting fit parameters are shown in Table B.1. Notice that the fit that better describes the correlation function is obtained with the Lévy form.

The comparison of the obtained correlation function including the finite resolution effects and without those effects is also shown in Fig. B.1, while the comparison of the fit parameters of the Lévy forms between those two cases is shown in Table B.2

Figure B.2 shows the finite resolution effects on the two-pion correlation function for the complete set of pions at a collision energy $\sqrt{s_{NN}} = 5.8$ GeV, together with its fits to the Lorentzian, Gaussian and Lévy forms. The resulting fit parameters are shown in Table B.3.

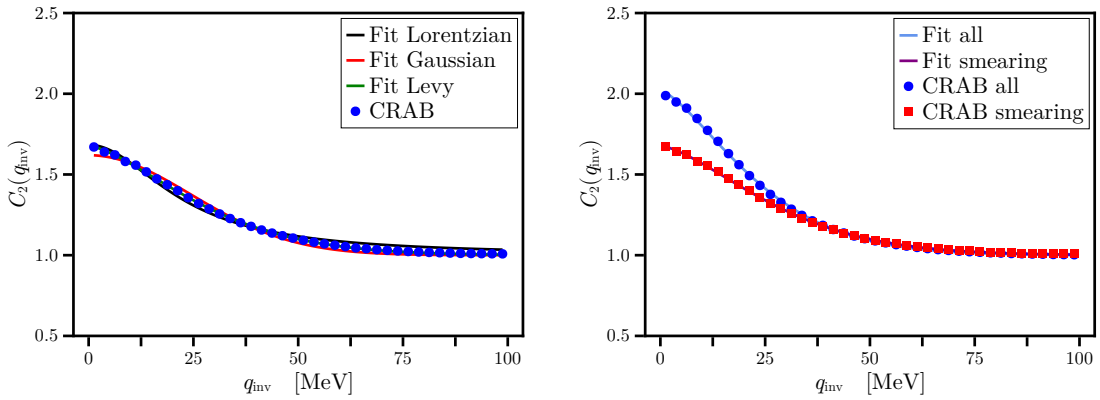

(a) Fits to finite resolution correlation function (b) Comparison between ideal and finite resolution

Figure B.1: Two-pion correlation function of Bi+Bi collisions at $\sqrt{s_{NN}} = 4.0$ GeV, with impact parameter $b = 0 - 1$ fm. In (a) the output of CRAB is shown but with the finite resolution effect of MPD, with a smearing of 10 MeV. The blue dots represent the output of CRAB, while the solid lines represent the fits to the Lorentz, Gaussian and Lévy forms. In (b), a comparison between the ideal and finite resolution is made, where the blue dots represent the same output of CRAB of Figure A.1, while the red dots include the finite resolution effect of MPD, with a smearing of 10 MeV. Solid lines represent the fit to a Lévy form.

	R_{inv} [fm]	λ	α	χ^2
Lorentzian	4.352 ± 0.125	0.684 ± 0.014	—	73.23
Gaussian	5.715 ± 0.094	0.619 ± 0.009	—	33.323
Lévy	6.129 ± 0.031	0.677 ± 0.003	1.478 ± 0.014	1.22

Table B.1: Parameters resulting from fits of the two-pion correlation function, obtained at $\sqrt{s_{NN}} = 4.0$ GeV, to Lorentzian, Gaussian and Lévy forms for the complete pion set that takes into account the finite resolution effects of MPD.

	R_{inv} [fm]	λ	α	χ^2
w. smearing	6.129 ± 0.031	0.677 ± 0.003	1.478 ± 0.014	1.22
wo. smearing	7.346 ± 0.051	1.018 ± 0.006	1.428 ± 0.018	3.533

Table B.2: Results of the fit to the two-pion correlation function with a Lévy form accounting for a finite resolution of the detector, setting a smearing of 10 MeV, for the complete pion set obtained at $\sqrt{s_{NN}} = 4.0$ GeV.

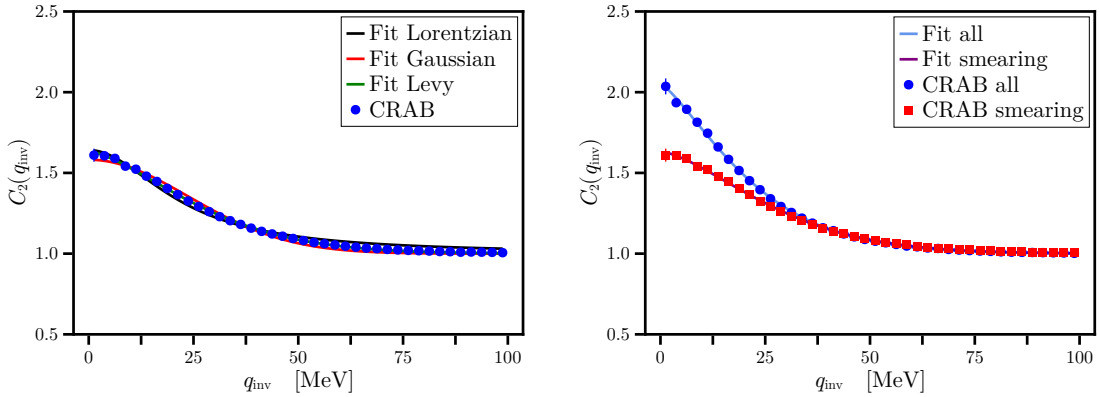

(a) Fits to finite resolution correlation function

(b) Comparison between ideal and finite resolution

Figure B.2: Two-pion correlation function of Bi+Bi collisions at $\sqrt{s_{NN}} = 5.8$ GeV, with impact parameter $b = 0 - 1$ fm. In (a) the output of CRAB is shown but with the finite resolution effect of MPD, with a smearing of 10 MeV. The blue dots represent the output of CRAB, while the solid lines represent the fits to the Lorentz, Gaussian and Lévy forms. In (b), a comparison between the ideal and finite resolution is made, where the blue dots represent the same output of CRAB of Figure A.2, while the red dots include the finite resolution effect of MPD, with a smearing of 10 MeV. Solid lines represent the fit to a Lévy form.

Notice that the fit that better describes the correlation function is obtained with the Lévy form.

The comparison of the obtained correlation function including the finite resolution effects and without those effects is also shown in Fig. B.2, while the comparison of the fit parameters of the Lévy forms between those two cases is shown in Table B.4

Figure B.3 shows the finite resolution effects on the two-pion correlation function for the complete set of pions at a collision energy $\sqrt{s_{NN}} = 7.7$ GeV, together with its fits to the Lorentzian, Gaussian and Lévy forms. The resulting fit parameters are shown in Table B.5. Notice that the fit that better describes the correlation function is obtained with the Lévy form.

The comparison of the obtained correlation function including the finite resolution effects and without those effects is also shown in Fig. B.3, while the comparison of the fit parameters of the Lévy forms between those two cases is shown in Table B.6

Figure B.4 shows the finite resolution effects on the two-pion correlation function for the complete set of pions at a collision energy $\sqrt{s_{NN}} = 9.2$ GeV, together with its fits to the Lorentzian, Gaussian and Lévy forms. The resulting fit parameters are shown in Table B.7. Again, the fit that better describes the correlation function is obtained with the Lévy form.

	R_{inv} [fm]	λ	α	χ^2
Lorentzian	4.449 ± 0.13	0.641 ± 0.013	—	28.227
Gaussian	5.856 ± 0.094	0.582 ± 0.008	—	13.295
Lévy	6.238 ± 0.046	0.632 ± 0.004	1.502 ± 0.022	0.912

Table B.3: Parameters resulting from fits of the two-pion correlation function, obtained at $\sqrt{s_{NN}} = 5.8$ GeV, to Lorentzian, Gaussian and Lévy forms for the complete pion set that takes into account the finite resolution effects of MPD.

	R_{inv} [fm]	λ	α	χ^2
w. smearing	6.238 ± 0.046	0.632 ± 0.004	1.502 ± 0.022	0.912
wo. smearing	8.121 ± 0.059	1.05 ± 0.006	1.312 ± 0.015	0.835

Table B.4: Results of the fit to the two-pion correlation function with a Lévy form accounting for a finite resolution of the detector, setting a smearing of 10 MeV, for the complete pion set obtained at $\sqrt{s_{NN}} = 5.8$ GeV.

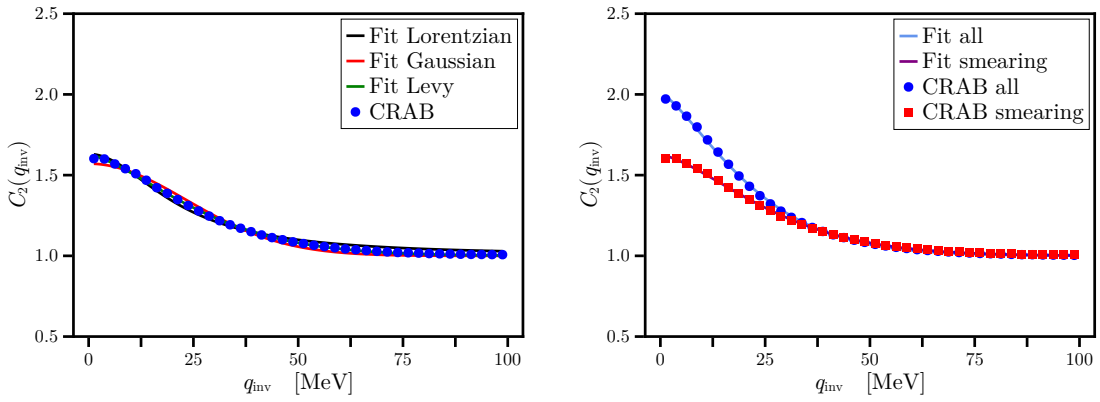

(a) Fits to finite resolution correlation function

(b) Comparison between ideal and finite resolution

Figure B.3: Two-pion correlation function of Bi+Bi collisions at $\sqrt{s_{NN}} = 7.7$ GeV, with impact parameter $b = 0 - 1$ fm. In (a) the output of CRAB is shown but with the finite resolution effect of MPD, with a smearing of 10 MeV. The blue dots represent the output of CRAB, while the solid lines represent the fits to the Lorentz, Gaussian and Lévy forms. In (b), a comparison between the ideal and finite resolution is made, where the blue dots represent the same output of CRAB of Figure A.3, while the red dots include the finite resolution effect of MPD, with a smearing of 10 MeV. Solid lines represent the fit to a Lévy form.

	R_{inv} [fm]	λ	α	χ^2
Lorentzian	4.569 ± 0.127	0.631 ± 0.012	—	55.101
Gaussian	5.995 ± 0.103	0.571 ± 0.008	—	31.039
Lévy	6.43 ± 0.046	0.625 ± 0.004	1.469 ± 0.02	1.838

Table B.5: Parameters resulting from fits of the two-pion correlation function, obtained at $\sqrt{s_{NN}} = 7.7$ GeV, to Lorentzian, Gaussian and Lévy forms for the complete pion set that takes into account the finite resolution effects of MPD.

	R_{inv} [fm]	λ	α	χ^2
w. smearing	6.43 ± 0.046	0.625 ± 0.004	1.469 ± 0.02	1.838
wo. smearing	8.119 ± 0.061	1.007 ± 0.006	1.352 ± 0.017	3.432

Table B.6: Results of the fit to the two-pion correlation function with a Lévy form accounting for a finite resolution of the detector, setting a smearing of 10 MeV, for the complete pion set obtained at $\sqrt{s_{NN}} = 7.7$ GeV.

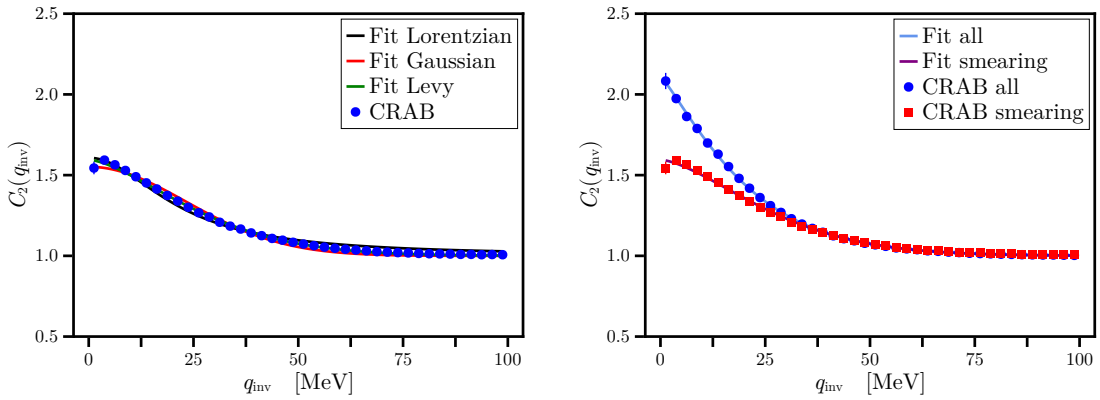

(a) Fits to finite resolution correlation function (b) Comparison between ideal and finite resolution

Figure B.4: Two-pion correlation function of Bi+Bi collisions at $\sqrt{s_{NN}} = 9.2$ GeV, with impact parameter $b = 0 - 1$ fm. In (a) the output of CRAB is shown but with the finite resolution effect of MPD, with a smearing of 10 MeV. The blue dots represent the output of CRAB, while the solid lines represent the fits to the Lorentz, Gaussian and Lévy forms. In (b), a comparison between the ideal and finite resolution is made, where the blue dots represent the same output of CRAB of Figure A.4, while the red dots include the finite resolution effect of MPD, with a smearing of 10 MeV. Solid lines represent the fit to a Lévy form.

	R_{inv} [fm]	λ	α	χ^2
Lorentzian	4.547 ± 0.14	0.607 ± 0.013	—	24.513
Gaussian	5.994 ± 0.104	0.552 ± 0.008	—	12.394
Lévy	6.342 ± 0.088	0.595 ± 0.007	1.526 ± 0.042	1.324

Table B.7: Parameters resulting from fits of the two-pion correlation function, obtained at $\sqrt{s_{NN}} = 9.2$ GeV, to Lorentzian, Gaussian and Lévy forms for the complete pion set that takes into account the finite resolution effects of MPD.

	R_{inv} [fm]	λ	α	χ^2
w. smearing	6.342 ± 0.088	0.595 ± 0.007	1.526 ± 0.042	1.324
wo. smearing	9.149 ± 0.054	1.109 ± 0.005	1.19 ± 0.01	0.289

Table B.8: Results of the fit to the two-pion correlation function with a Lévy form accounting for a finite resolution of the detector, setting a smearing of 10 MeV, for the complete pion set obtained at $\sqrt{s_{NN}} = 9.2$ GeV.

The comparison of the obtained correlation function including the finite resolution effects and without those effects is also shown in Fig. B.4, while the comparison of the fit parameters of the Lévy forms between those two cases is shown in Table B.8

B.2 Finite resolution effects on the two-pion correlation function for the separated samples

Figure B.5 shows the effects of finite resolution on the two-pion correlation function for primary and secondary pions at a collision energy $\sqrt{s_{NN}} = 4.0$ GeV, together with its fits to the Lorentzian, Gaussian and Lévy forms. Tables B.9 and B.10 show the resulting fit parameters for primary and secondary pions, respectively. Notice that the fit that better describes the correlation for both, primary and secondary pions, is obtained with the Lévy form.

	R_{inv} [fm]	λ	α	χ^2
Lorentzian	2.373 ± 9.506	0.938 ± 0.016	—	175.441
Gaussian	3.381 ± 0.022	0.878 ± 0.005	—	18.747
Lévy	3.454 ± 0.008	0.907 ± 0.002	1.757 ± 0.011	2.016

Table B.9: Parameters resulting from fits of the two-pion correlation function, obtained at $\sqrt{s_{NN}} = 4.0$ GeV, to Lorentzian, Gaussian and Lévy forms for the primary pions, accounting for a finite resolution of the detector, setting a smearing of 10 MeV.

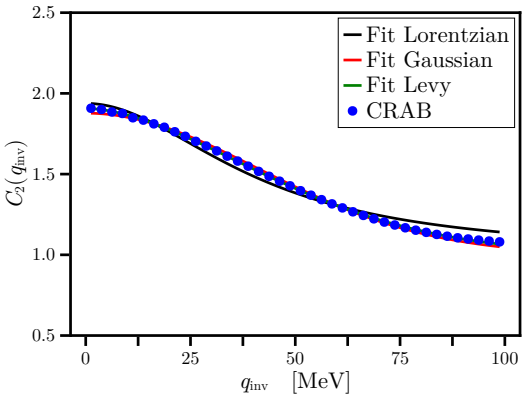

(a) Primary pions

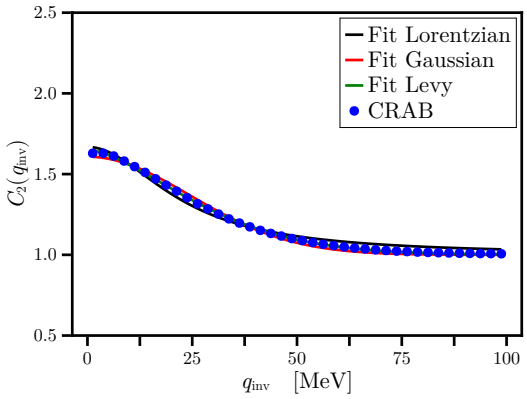

(b) Secondary pions

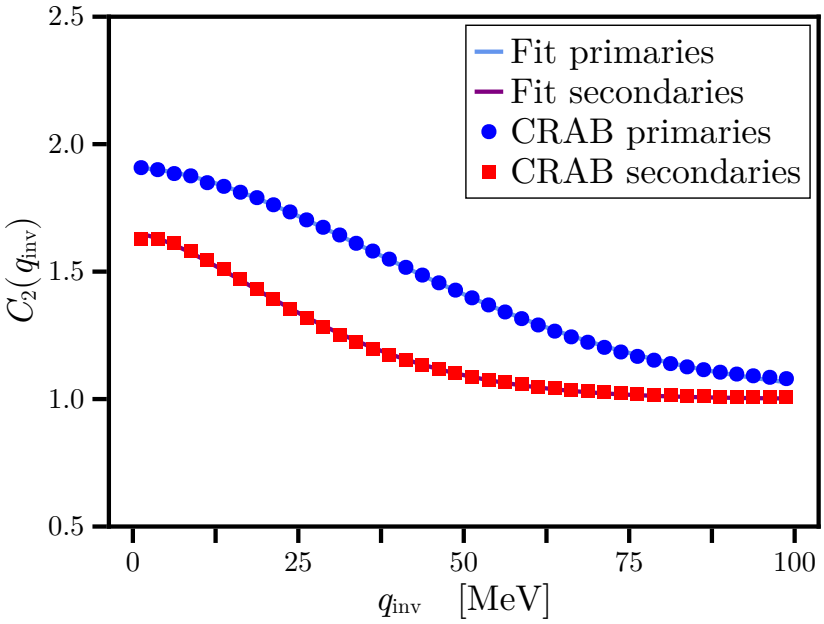

(c) Primary and secondary pions

Figure B.5: Two-pion correlation function of (a) primary and (b) secondary pions, produced in Bi+Bi collisions at $\sqrt{s_{NN}} = 4.0$ GeV, with impact parameter $b = 0 - 1$ fm. The blue dots and the red squares represent the output of CRAB with a smearing of 10 MeV, while the solid lines represent the fits Lorentzian (black), Gaussian (red) and Lévy (green) fits. The two-pion correlation function of primary and secondary pion, together with its fits to the Lévy forms are compared in (c).

	R_{inv} [fm]	λ	α	χ^2
Lorentzian	4.328 ± 0.138	0.668 ± 0.015	—	83.766
Gaussian	5.716 ± 0.079	0.608 ± 0.007	—	24.708
Lévy	6.022 ± 0.036	0.651 ± 0.004	1.564 ± 0.019	1.594

Table B.10: Parameters resulting from fits of the two-pion correlation function, obtained at $\sqrt{s_{NN}} = 4.0$ GeV, to Lorentzian, Gaussian and Lévy forms for the secondary pions, accounting for a finite resolution of the detector, setting a smearing of 10 MeV.

	R_{inv} [fm]	λ	α	χ^2
w. smearing	3.454 ± 0.008	0.907 ± 0.002	1.757 ± 0.011	2.016
wo. smearing	3.567 ± 0.01	0.998 ± 0.003	1.878 ± 0.015	3.481

Table B.11: Results of the fit to the two-pion correlation function with a Lévy form accounting for a finite resolution of the detector, setting a smearing of 10 MeV, for the primary pions obtained at $\sqrt{s_{NN}} = 4.0$ GeV.

The comparison between the correlation function for primary and secondary pions, including the finite resolution effects, is also shown in Fig. B.5, while the comparison of the fit parameters of the Lévy forms between those two cases is shown in Tables B.11 and B.12, respectively.

Figure B.6 shows the effects of finite resolution on the two-pion correlation function for primary and secondary pions at a collision energy $\sqrt{s_{NN}} = 5.8$ GeV, together with its fits to the Lorentzian, Gaussian and Lévy forms. Tables B.13 and B.14 show the resulting fit parameters for primary and secondary pions, respectively. Notice that the fit that better describes the correlation for both, primary and secondary pions, is obtained with the Lévy form.

The comparison between the correlation function for primary and secondary pions, including the finite resolution effects, is also shown in Fig. B.6, while the comparison of the fit parameters of the Lévy forms between those two cases is shown in Tables B.15 and B.16, respectively.

	R_{inv} [fm]	λ	α	χ^2
w. smearing	6.022 ± 0.036	0.651 ± 0.004	1.564 ± 0.019	1.594
wo. smearing	7.566 ± 0.035	1.043 ± 0.004	1.399 ± 0.011	1.298

Table B.12: Results of the fit to the two-pion correlation function with a Lévy form accounting for a finite resolution of the detector, setting a smearing of 10 MeV, for the secondary pions obtained at $\sqrt{s_{NN}} = 4.0$ GeV.

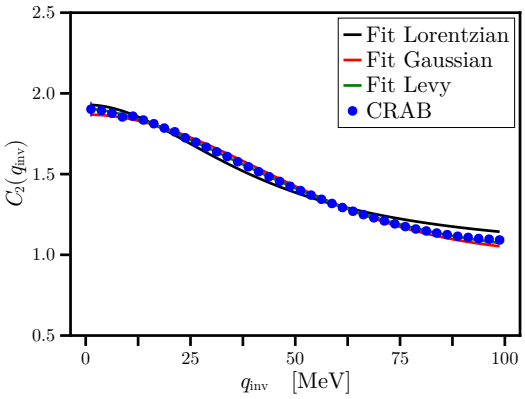

(a) Primary pions

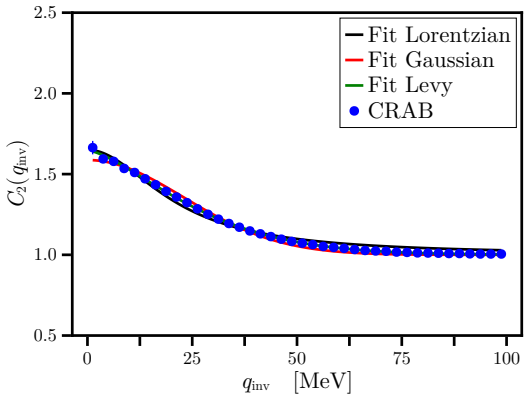

(b) Secondary pions

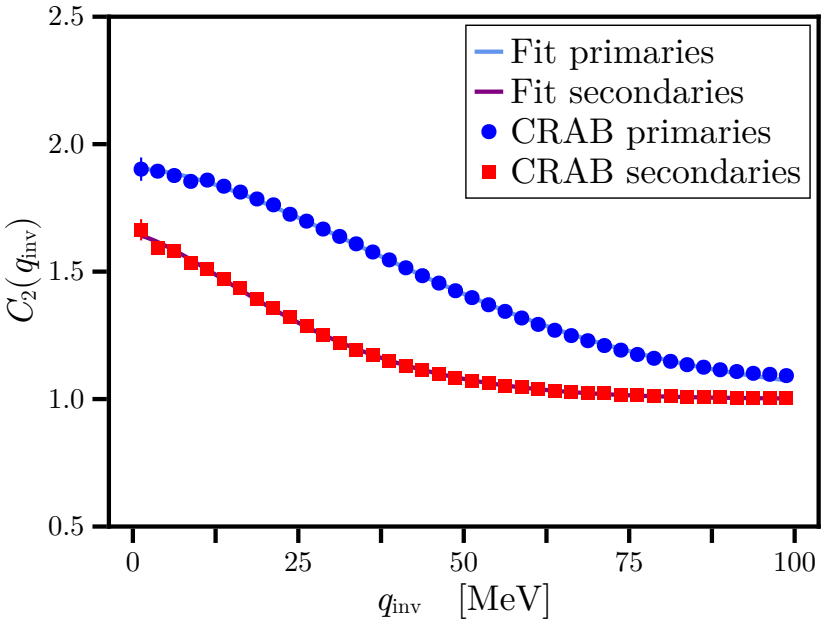

(c) Primary and secondary pions

Figure B.6: Two-pion correlation function of (a) primary and (b) secondary pions, produced in Bi+Bi collisions at $\sqrt{s_{NN}} = 5.8$ GeV, with impact parameter $b = 0 - 1$ fm. The blue dots and the red squares represent the output of CRAB with a smearing of 10 MeV, while the solid lines represent the fits Lorentzian (black), Gaussian (red) and Lévy (green) fits. The two-pion correlation function of primary and secondary pion, together with its fits to the Lévy forms are compared in (c).

	R_{inv} [fm]	λ	α	χ^2
Lorentzian	2.341 ± 8.843	0.93 ± 0.014	—	60.619
Gaussian	3.339 ± 0.027	0.869 ± 0.006	—	13.614
Lévy	3.426 ± 0.012	0.905 ± 0.003	1.709 ± 0.016	1.615

Table B.13: Parameters resulting from fits of the two-pion correlation function, obtained at $\sqrt{s_{NN}} = 5.8$ GeV, to Lorentzian, Gaussian and Lévy forms for the primary pions, accounting for a finite resolution of the detector, setting a smearing of 10 MeV.

	R_{inv} [fm]	λ	α	χ^2
Lorentzian	4.673 ± 0.147	0.65 ± 0.014	—	31.385
Gaussian	6.083 ± 0.108	0.587 ± 0.009	—	10.753
Lévy	6.591 ± 0.054	0.647 ± 0.005	1.447 ± 0.022	0.259

Table B.14: Parameters resulting from fits of the two-pion correlation function, obtained at $\sqrt{s_{NN}} = 5.8$ GeV, to Lorentzian, Gaussian and Lévy forms for the secondary pions, accounting for a finite resolution of the detector, setting a smearing of 10 MeV.

	R_{inv} [fm]	λ	α	χ^2
w. smearing	3.426 ± 0.012	0.905 ± 0.003	1.709 ± 0.016	1.615
wo. smearing	3.516 ± 0.014	0.982 ± 0.004	1.863 ± 0.021	0.353

Table B.15: Results of the fit to the two-pion correlation function with a Lévy form accounting for a finite resolution of the detector, setting a smearing of 10 MeV, for the primary pions obtained at $\sqrt{s_{NN}} = 5.8$ GeV.

	R_{inv} [fm]	λ	α	χ^2
w. smearing	6.591 ± 0.054	0.647 ± 0.005	1.447 ± 0.022	0.259
wo. smearing	8.402 ± 0.065	1.066 ± 0.007	1.31 ± 0.016	0.321

Table B.16: Results of the fit to the two-pion correlation function with a Lévy form accounting for a finite resolution of the detector, setting a smearing of 10 MeV, for the secondary pions obtained at $\sqrt{s_{NN}} = 5.8$ GeV.

	R_{inv} [fm]	λ	α	χ^2
Lorentzian	2.347 ± 8.157	0.92 ± 0.013	—	79.954
Gaussian	3.338 ± 0.031	0.859 ± 0.007	—	27.6
Lévy	3.441 ± 0.013	0.9 ± 0.003	1.67 ± 0.017	2.779

Table B.17: Parameters resulting from fits of the two-pion correlation function, obtained at $\sqrt{s_{NN}} = 7.7$ GeV, to Lorentzian, Gaussian and Lévy forms for the primary pions, accounting for a finite resolution of the detector, setting a smearing of 10 MeV.

	R_{inv} [fm]	λ	α	χ^2
Lorentzian	4.718 ± 0.151	0.621 ± 0.014	—	50.612
Gaussian	6.182 ± 0.091	0.563 ± 0.007	—	14.717
Lévy	6.557 ± 0.035	0.608 ± 0.003	1.532 ± 0.017	0.647

Table B.18: Parameters resulting from fits of the two-pion correlation function, obtained at $\sqrt{s_{NN}} = 7.7$ GeV, to Lorentzian, Gaussian and Lévy forms for the secondary pions, accounting for a finite resolution of the detector, setting a smearing of 10 MeV.

Figure B.7 shows the effects of finite resolution on the two-pion correlation function for primary and secondary pions at a collision energy $\sqrt{s_{NN}} = 7.7$ GeV, together with its fits to the Lorentzian, Gaussian and Lévy forms. Tables B.17 and B.18 show the resulting fit parameters for primary and secondary pions, respectively. Notice that the fit that better describes the correlation for both, primary and secondary pions, is obtained with the Lévy form.

The comparison between the correlation function for primary and secondary pions, including the finite resolution effects, is also shown in Fig. B.7, while the comparison of the fit parameters of the Lévy forms between those two cases is shown in Tables B.19 and B.20, respectively.

Figure B.8 shows the effects of finite resolution on the two-pion correlation function for primary and secondary pions at a collision energy $\sqrt{s_{NN}} = 9.2$ GeV, together with its fits to the Lorentzian, Gaussian and Lévy forms. Tables B.21 and B.22 show the resulting fit parameters for primary and secondary pions, respectively. Notice that the fit that better

	R_{inv} [fm]	λ	α	χ^2
w. smearing	3.441 ± 0.013	0.9 ± 0.003	1.67 ± 0.017	2.779
wo. smearing	3.596 ± 0.007	1.002 ± 0.002	1.752 ± 0.009	0.385

Table B.19: Results of the fit to the two-pion correlation function with a Lévy form accounting for a finite resolution of the detector, setting a smearing of 10 MeV, for the primary pions obtained at $\sqrt{s_{NN}} = 7.7$ GeV.

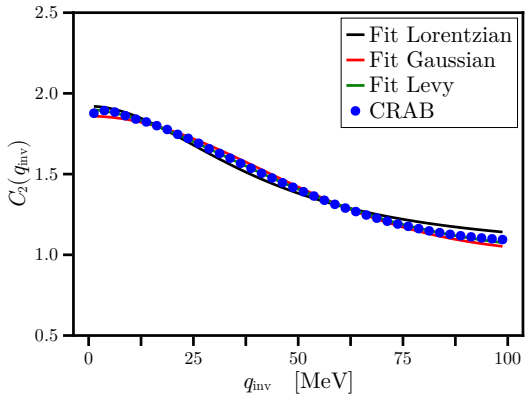

(a) Primary pions

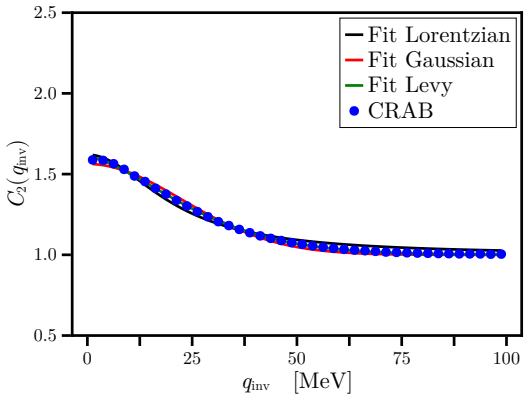

(b) Secondary pions

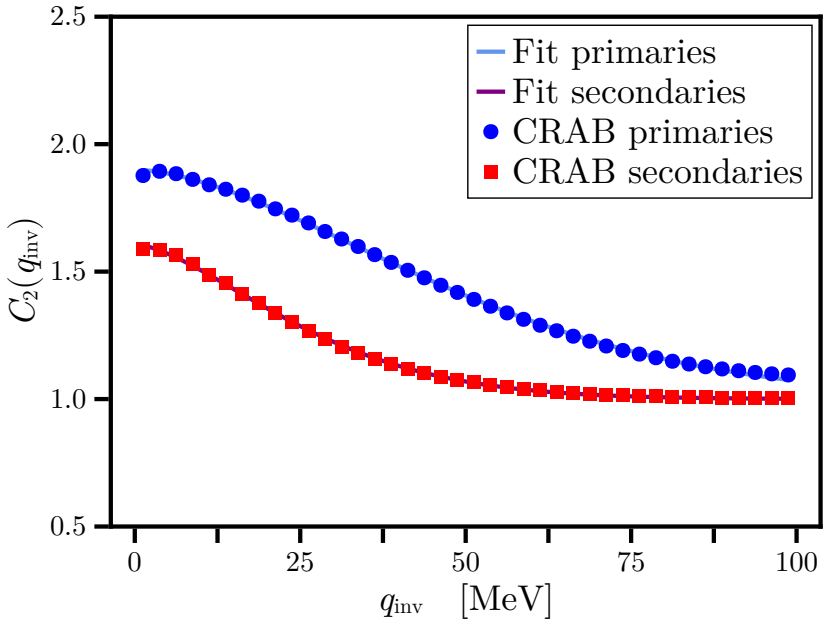

(c) Primary and secondary pions

Figure B.7: Two-pion correlation function of (a) primary and (b) secondary pions, produced in Bi+Bi collisions at $\sqrt{s_{NN}} = 7.7$ GeV, with impact parameter $b = 0 - 1$ fm. The blue dots and the red squares represent the output of CRAB with a smearing of 10 MeV, while the solid lines represent the fits Lorentzian (black), Gaussian (red) and Lévy (green) fits. The two-pion correlation function of primary and secondary pion, together with its fits to the Lévy forms are compared in (c).

	R_{inv} [fm]	λ	α	χ^2
w. smearing	6.557 ± 0.035	0.608 ± 0.003	1.532 ± 0.017	0.647
wo. smearing	8.235 ± 0.038	0.995 ± 0.004	1.409 ± 0.012	1.516

Table B.20: Results of the fit to the two-pion correlation function with a Lévy form accounting for a finite resolution of the detector, setting a smearing of 10 MeV, for the secondary pions obtained at $\sqrt{s_{NN}} = 7.7$ GeV.

	R_{inv} [fm]	λ	α	χ^2
Lorentzian	2.357 ± 8.253	0.909 ± 0.013	—	60.526
Gaussian	3.352 ± 0.032	0.848 ± 0.007	—	21.856
Lévy	3.451 ± 0.02	0.887 ± 0.005	1.681 ± 0.025	2.61

Table B.21: Parameters resulting from fits of the two-pion correlation function, obtained at $\sqrt{s_{NN}} = 9.2$ GeV, to Lorentzian, Gaussian and Lévy forms for the primary pions, accounting for a finite resolution of the detector, setting a smearing of 10 MeV.

describes the correlation for both, primary and secondary pions, is obtained with the Lévy form.

The comparison between the correlation function for primary and secondary pions, including the finite resolution effects, is also shown in Fig. B.8, while the comparison of the fit parameters of the Lévy forms between those two cases is shown in Tables B.23 and B.24, respectively.

	R_{inv} [fm]	λ	α	χ^2
Lorentzian	4.813 ± 0.155	0.613 ± 0.014	—	35.826
Gaussian	6.297 ± 0.095	0.556 ± 0.007	—	10.377
Lévy	6.7 ± 0.039	0.602 ± 0.003	1.518 ± 0.018	0.43

Table B.22: Parameters resulting from fits of the two-pion correlation function, obtained at $\sqrt{s_{NN}} = 9.2$ GeV, to Lorentzian, Gaussian and Lévy forms for the secondary pions, accounting for a finite resolution of the detector, setting a smearing of 10 MeV.

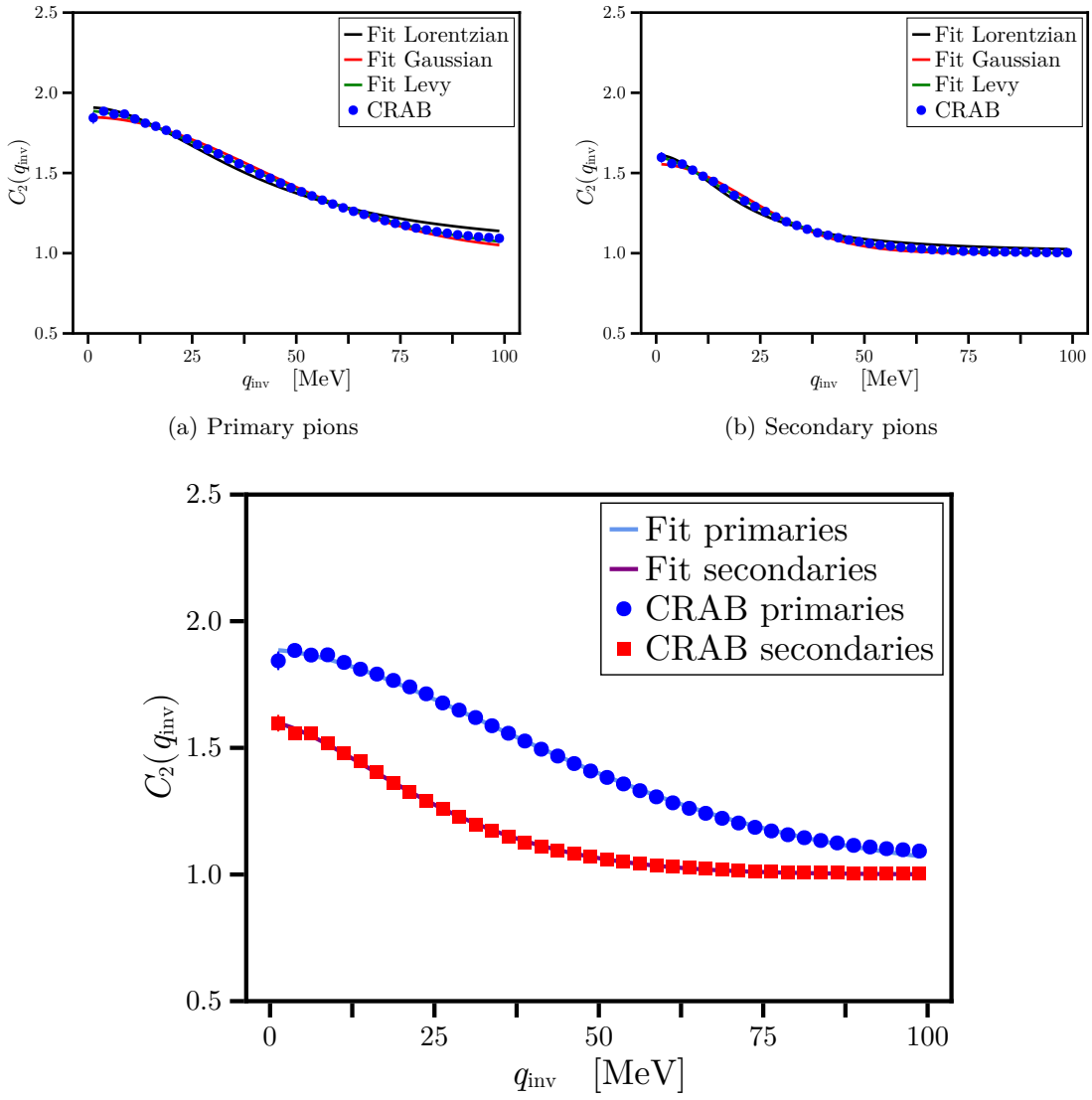

(a) Primary pions

(b) Secondary pions

(c) Primary and secondary pions

Figure B.8: Two-pion correlation function of (a) primary and (b) secondary pions, produced in Bi+Bi collisions at $\sqrt{s_{NN}} = 9.2$ GeV, with impact parameter $b = 0 - 1$ fm. The blue dots and the red squares represent the output of CRAB with a smearing of 10 MeV, while the solid lines represent the fits Lorentzian (black), Gaussian (red) and Lévy (green) fits. The two-pion correlation function of primary and secondary pion, together with its fits to the Lévy forms are compared in (c).

	R_{inv} [fm]	λ	α	χ^2
w. smearing	3.451 ± 0.02	0.887 ± 0.005	1.681 ± 0.025	2.61
wo. smearing	3.686 ± 0.02	1.016 ± 0.005	1.668 ± 0.023	1.074

Table B.23: Results of the fit to the two-pion correlation function with a Lévy form accounting for a finite resolution of the detector, setting a smearing of 10 MeV, for the primary pions obtained at $\sqrt{s_{NN}} = 9.2$ GeV.

	R_{inv} [fm]	λ	α	χ^2
w. smearing	6.7 ± 0.039	0.602 ± 0.003	1.518 ± 0.018	0.43
wo. smearing	8.647 ± 0.047	1.022 ± 0.005	1.353 ± 0.012	0.469

Table B.24: Results of the fit to the two-pion correlation function with a Lévy form accounting for a finite resolution of the detector, setting a smearing of 10 MeV, for the secondary pions obtained at $\sqrt{s_{NN}} = 9.2$ GeV.

Bibliography

[1] A. Ayala, S. Bernal-Langarica, I. Dominguez, I. Maldonado, and M. E. Tejeda-Yeomans, "Collision energy dependence of source sizes for primary and secondary pions at NICA energies," (2023), arXiv:2401.00619 [hep-ph] .

[2] C. Drischler, J. W. Holt, and C. Wellenhofer, "Chiral Effective Field Theory and the High-Density Nuclear Equation of State," Ann. Rev. Nucl. Part. Sci. **71**, 403–432 (2021), arXiv:2101.01709 [nucl-th] .

[3] A. Bzdak, S. Esumi, V. Koch, J. Liao, M. Stephanov, and N. Xu, "Mapping the Phases of Quantum Chromodynamics with Beam Energy Scan," Phys. Rept. **853**, 1–87 (2020), arXiv:1906.00936 [nucl-th] .

[4] S. Sharma (Bielefeld-BNL-CCNU), "The QCD Equation of state and critical end-point estimates at $\mathcal{O}(\mu_B^6)$," Nucl. Phys. A **967**, 728–731 (2017), arXiv:1704.05969 [hep-lat] .

[5] M. A. Stephanov, K. Rajagopal, and E. V. Shuryak, "Event-by-event fluctuations in heavy ion collisions and the QCD critical point," Phys. Rev. D **60**, 114028 (1999), arXiv:hep-ph/9903292 .

[6] R. Lednicky, "Progress in correlation femtoscopy," in *32nd International Symposium on Multiparticle Dynamics* (2002) pp. 21–26, arXiv:nucl-th/0212089 .

[7] R. Hanbury Brown and R. Q. Twiss, "A New type of interferometer for use in radio astronomy," Phil. Mag. Ser. 7 **45**, 663–682 (1954).

[8] R. Hanbury Brown and R. Q. Twiss, "A Test of a new type of stellar interferometer on Sirius," Nature **178**, 1046–1048 (1956).

[9] V. Abgaryan *et al.* (MPD), "Status and initial physics performance studies of the MPD experiment at NICA," Eur. Phys. J. A **58**, 140 (2022), arXiv:2202.08970 [physics.ins-det] .

[10] G. Goldhaber, S. Goldhaber, W.-Y. Lee, and A. Pais, "Influence of Bose-Einstein statistics on the anti-proton proton annihilation process," Phys. Rev. **120**, 300–312 (1960).

[11] M. A. Lisa, S. Pratt, R. Soltz, and U. Wiedemann, "Femtoscopy in relativistic heavy ion collisions," Ann. Rev. Nucl. Part. Sci. **55**, 357–402 (2005), arXiv:nucl-ex/0505014 .

[12] A. K. Chaudhuri, *A short course on Relativistic Heavy Ion Collisions* (IOPP, 2014) arXiv:1207.7028 [nucl-th] .

[13] A. Ayala, S. Bernal-Langarica, and C. Villavicencio, "Finite volume and magnetic field effects on the two-pion correlation function in relativistic heavy-ion collisions," Phys. Rev. D **105**, 056001 (2022), arXiv:2111.05951 [hep-ph] .

[14] A. Ayala and A. Sanchez, "Boundary and expansion effects on two pion correlation functions in relativistic heavy ion collisions," Phys. Rev. C **63**, 064901 (2001), arXiv:nucl-th/0101020 .

[15] H. Adhikary *et al.* (NA61/SHINE), "Two-pion femtoscopic correlations in Be+Be collisions at $\sqrt{s_{\rm NN}} = 16.84$ GeV measured by the NA61/SHINE at CERN," Eur. Phys. J. C **83**, 919 (2023), arXiv:2302.04593 [nucl-ex] .

[16] T. Csorgo, "Particle interferometry from 40-MeV to 40-TeV," Acta Phys. Hung. A **15**, 1–80 (2002), arXiv:hep-ph/0001233 .

[17] A. Adare *et al.* (PHENIX), "Lévy-stable two-pion Bose-Einstein correlations in $\sqrt{s_{NN}} =$ 200 GeV Au+Au collisions," Phys. Rev. C **97**, 064911 (2018), [Erratum: Phys.Rev.C 108, 049905 (2023)], arXiv:1709.05649 [nucl-ex] .

[18] U. A. Wiedemann and U. W. Heinz, "Particle interferometry for relativistic heavy ion collisions," Phys. Rept. **319**, 145–230 (1999), arXiv:nucl-th/9901094 .

[19] J. Adamczewski-Musch *et al.* (HADES), "Identical pion intensity interferometry at $\sqrt{s_{\rm NN}} = 2.4$ GeV: HADES collaboration," Eur. Phys. J. A **56**, 140 (2020), arXiv:1910.07885 [nucl-ex] .

[20] M. Naraschewski and R. J. Glauber, "Spatial coherence and density correlations of trapped bose gases," Phys. Rev. A **59**, 4595–4607 (1999), arXiv:cond-mat/9806362 .

[21] C.-Y. Wong and W.-N. Zhang, "Chaoticity parameter λ in hanbury-brown–twiss interferometry," Phys. Rev. C **76**, 034905 (2007), arXiv:0708.1948 [hep-ph] .

[22] G. Baym, "The Physics of Hanbury Brown-Twiss intensity interferometry: From stars to nuclear collisions," Acta Phys. Polon. B **29**, 1839–1884 (1998), arXiv:nucl-th/9804026 .

[23] J. Bolz, U. Ornik, M. Plumer, B. R. Schlei, and R. M. Weiner, "Resonance decays and partial coherence in Bose-Einstein correlations," Phys. Rev. D **47**, 3860–3870 (1993).

[24] T. Csorgo, B. Lorstad, and J. Zimanyi, "Bose-Einstein correlations for systems with large halo," Z. Phys. C **71**, 491–497 (1996), arXiv:hep-ph/9411307 .

[25] R. J. Fries, B. Muller, C. Nonaka, and S. A. Bass, "Hadron production in heavy ion collisions: Fragmentation and recombination from a dense parton phase," Phys. Rev. C **68**, 044902 (2003), arXiv:nucl-th/0306027 .

[26] P. Senger and H. Strobele, "Hadronic particle production in nucleus-nucleus collisions," J. Phys. G **25**, R59–R131 (1999), arXiv:nucl-ex/9810007 .

[27] T. Csorgo, S. Hegyi, and W. A. Zajc, "Bose-Einstein correlations for Levy stable source distributions," Eur. Phys. J. C **36**, 67–78 (2004), arXiv:nucl-th/0310042 .

[28] W. A. Zajc *et al.*, "Two-pion correlations in heavy ion collisions," Phys. Rev. C **29**, 2173–2187 (1984).

[29] S. Pratt *et al.*, "Testing transport theories with correlation measurements," Nucl. Phys. A **566**, 103C–114C (1994).

[30] S. Pratt, "Crab software," (1997), available at https://web.pa.msu.edu/people/pratts/freecodes/crab/home.html.

[31] D. L. Mihaylov, V. Mantovani Sarti, O. W. Arnold, L. Fabbietti, B. Hohlweger, and A. M. Mathis, "A femtoscopic Correlation Analysis Tool using the Schrödinger equation (CATS)," Eur. Phys. J. C **78**, 394 (2018), arXiv:1802.08481 [hep-ph] .

[32] D. A. Brown and P. Danielewicz, "Imaging of sources in heavy ion reactions," Phys. Lett. B **398**, 252–258 (1997), arXiv:nucl-th/9701010 .

[33] D. A. Brown and P. Danielewicz, "Optimized discretization of sources imaged in heavy ion reactions," Phys. Rev. C **57**, 2474–2483 (1998), arXiv:nucl-th/9712066 .

[34] D. A. Brown and P. Danielewicz, "Observing nongaussian sources in heavy ion reactions," Phys. Rev. C **64**, 014902 (2001), arXiv:nucl-th/0010108 .

[35] M. Nagy, A. Purzsa, M. Csanád, and D. Kincses, "A novel method for calculating Bose–Einstein correlation functions with Coulomb final-state interaction," Eur. Phys. J. C **83**, 1015 (2023), arXiv:2308.10745 [nucl-th] .

[36] M. Nagy, A. Purzsa, M. Csanád, and D. Kincses, "Correlation function calculation with Lévy source and Coulomb FSI," (2023), available at https://github.com/csanadm/CoulCorrLevyIntegral.

[37] T. Csorgo, "Correlation Probes of a QCD Critical Point," PoS **HIGH-PTLHC08**, 027 (2008), arXiv:0903.0669 [nucl-th] .

[38] K. Rajagopal and F. Wilczek, "Static and dynamic critical phenomena at a second order QCD phase transition," Nucl. Phys. B **399**, 395–425 (1993), arXiv:hep-ph/9210253 .

[39] H. Rieger, "Critical behavior of the three-dimensional random-field Ising model: Two-exponent scaling and discontinuous transition," Phys. Rev. B **52** (1995), 10.1103/PhysRevB.52.6659.

[40] T. Csorgo, S. Hegyi, T. Novak, and W. A. Zajc, "Bose-Einstein or HBT correlation signature of a second order QCD phase transition," AIP Conf. Proc. **828**, 525–532 (2006), arXiv:nucl-th/0512060 .

[41] M. Csanad (PHENIX), "Exploring the QCD phase diagram via the collision energy dependence of multi-particle femtoscopy with PHENIX," J. Phys. Conf. Ser. **1602**, 012009 (2020), arXiv:2007.04751 [nucl-ex] .

[42] S. A. Bass *et al.*, "Microscopic models for ultrarelativistic heavy ion collisions," Prog. Part. Nucl. Phys. **41**, 255–369 (1998), arXiv:nucl-th/9803035 .

[43] M. Bleicher *et al.*, "Relativistic hadron hadron collisions in the ultrarelativistic quantum molecular dynamics model," J. Phys. G **25**, 1859–1896 (1999), arXiv:hep-ph/9909407 .

[44] M. Bleicher *et al.* (The UrQMD group), *The UrQMD user guide* (2014), available at https://itp.uni-frankfurt.de/~bleicher/userguide.pdf.

[45] G. Gräf, *Hanbury-Brown-Twiss Interferometry Within the UrQMD Transport Approach*, Master's thesis, Johann Wolfgang Goethe-Universität in Frankfurt am Main (2013), unpublished, available at https://publikationen.ub.uni-frankfurt.de/opus4/frontdoor/deliver/index/docId/31556/file/Main.pdf.

[46] L. P. Csernai, *Introduction to relativistic heavy ion collisions* (John Wiley & Sons Ltd., 1994).

[47] T. Csorgo, S. Hegyi, T. Novak, and W. A. Zajc, "Bose-Einstein or HBT correlations and the anomalous dimension of QCD," Acta Phys. Polon. B **36**, 329–337 (2005), arXiv:hep-ph/0412243 .

[48] W. A. Zajc, "A pedestrian's guide to interferometry," NATO Sci. Ser. B **303**, 435–459 (1993).

[49] A. Maevskiy, F. Ratnikov, A. Zinchenko, and V. Riabov, "Simulating the time projection chamber responses at the MPD detector using generative adversarial networks," Eur. Phys. J. C **81**, 599 (2021), arXiv:2012.04595 [physics.ins-det] .

[50] D. Kincses, "Two-particle interferometry with Lévy-stable sources in Au+Au collisions at STAR," (2023), slides from the presentation given at the 23rd Zimányi School Winter Workshop on Heavy Ion Physics, available at https://indico.cern.ch/event/1352455/contributions/5696657/attachments/2764575/4823959/kincsesd_zimanyi2023_talk_v2.pdf.

[51] D. Kincses, M. Stefaniak, and M. Csanád, "Event-by-Event Investigation of the Two-Particle Source Function in Heavy-Ion Collisions with EPOS," Entropy **24**, 308 (2022), arXiv:2201.07962 [hep-ph] .

[52] B. Kórodi, D. Kincses, and M. Csanád, "Event-by-event investigation of the two-particle source function in sNN=2.76 TeV PbPb collisions with EPOS," Phys. Lett. B **847**, 138295 (2023), arXiv:2212.02980 [nucl-th] .